Dark Matter Search with NaI(Tl) crystal and lowering the analysis threshold for COSINE-100 experiment

Govinda Adhikari

February 2019

Department of Physics

The Graduate School

Sejong University

Dark Matter Search with NaI(Tl) crystal and lowering the analysis threshold for COSINE-100 experiment

Govinda Adhikari

A dissertation submitted to the Faculty of the Sejong University in partial fulfillment of the requirements for the degree of Doctor of Philosophy in Physics

February 2019

Approved by Professor Yeongduk Kim

Dark Matter Search with NaI(Tl) crystal and lowering the analysis threshold for COSINE-100 experiment

by

Govinda Adhikari

Approved ---------------------
Professor Seyong Kim

Approved ---------------------
Professor Hyungchae Jung

Approved ---------------------
Professor Hyunsoo Kim

Approved ---------------------
Professor Yongsun Kim

Approved ---------------------
Professor Yeongduk Kim

Abstract

Astronomical observations including the velocities of stars and galaxies and gravitational lensing measurements led to the conclusion that the majority of the matter in our universe is dark because it isn't visible. Several theoretical evidences strongly support that the WIMPs (Weakly Interacting Massive Particles) is one of the attractive candidate for dark matter. It is quite challenging to run the very low-background detector in deep underground laboratory to detect the rarely occurring interactions of WIMPs with nuclei of the normal matter. The DAMA/LIBRA experiment has reported a low-energy annual modulation signal with 12.9 σ from more than 15 years in an array of low background NaI(Tl) detector which may have been caused by the WIMP interaction. However, there is a continuous debate about the DAMA signal in the scientific community so that independent experiment for confirmation of the DAMA's results with the same target materials is necessary. The COSINE-100 is a dark matter direct detection experiment using low-background NaI(Tl) crystals to test the DAMA/LIBRA collaboration's claim about detection of the dark matter annual modulation. The COSINE-100 experiment has been running smoothly since September 2016 at the Yangyang Underground Laboratory in South Korea, using 8 NaI(Tl) crystals in a total of 106 kg and ~2 ton of liquid scintillator. This thesis describes about the COSINE-100 detectors assembly, its performance and background understanding for 1.7 years of the data. A dark matter-induced annual modulation search has been performed using 2 keV energy threshold and observed the best fit values for modulation amplitude and phase of 0.0092 ± 0.0067 counts/keV/kg/day and 127.2 ± 45.9 days, respectively. This thesis also covers the method used to lower the threshold from 2 keV to 1 keV and model dependent WIMP analysis with null hypothesis of the dark matter interaction which allows to set an exclusion limit that covers DAMA/LIBRA parameter space.

TABLE OF CONTENTS

LIST OF FIGURES

Chapter 1

Review of the Dark Matter

This chapter contains the overview of the history of dark matter from cosmological models to astronomical observations. It will continue with dark matter theory, its evidence and current technologies and techniques that are needed to understand the idea of our experimental observations.

1.1 Cosmological Model

The ΛCDM (Lambda cold dark matter) or Lambda-CDM is a model parametrization of the Big Bang cosmological model which consists of three major components of the Universe. First, a cosmological constant denoted by Lambda and associated dark energy; second, the postulated cold dark matter and third, the ordinary matter. ΛCDM explains the Universe from the Big Bang, it contains massive structure at variety scales and its expanding. The ΛCDM model can be extended by adding quintessence, cosmological inflation and other elements that are current areas of study and research. ΛCDM is constituted of 6 parameters: dark matter density, baryon density, dark energy density, curvature fluctuation, scalar spectral index and re-ionization optical depth [1]. These parameters are fit to match with astronomical observations like rotation of galaxy curves, gravitational lensing, Cosmic

Microwave Background (CMB), Big Bang Nucleosynthesis (BBN), supernova redshifts and Large-Scale Structure (LSS).

ΛCDM is an amalgamation of the preferred cosmological framework from a research of astronomical observations and theoretical models. The first theory is postulated by Vesto Slipher's in 1912 which is the observation of Doppler shift showing that all galaxies are receding away from the Earth [2]. This observation was explained in 1927 by Lemaitre through the postulation of the occurrence of the Big Bang by observing the expansion of the Universe. A point is obtained where all masses are focused into a "primeval atom", for space-time existence [3]. Edwin Hubble derived Hubble's law from measurements of the distance of the galaxies with known redshifts. Those galaxies which looked farther away were receding from the Earth at faster velocity, he defined the relation:

$$\upsilon = H_0 D \tag{1}$$

Where 'υ' is the velocity of the Galaxy, D is the distance of a galaxy from the observer, and H_0 is the Hubble's constant [4].

After the discovery of the CMB, the Big Bang model was favored for the cosmological model. The discovery supported the current model over the theory of universal expansion to describe the observations. This proposed a new matter that leads both the measurements and the observations and that could be interpreted as the Universe's expansion. This model given impact that the Universe should look the similar at any point of view and time, directly in contradiction to the Big Bang model which predicts a hotter much denser universe in the past. Presently, Planck collaboration reported observations of the cosmological parameters describing the nature of the Universe. The observation included 15.5 months of data and gives the evidence that supported by the ΛCDM model of the Universe. Their observation predicts that the Universe is made out of (4.82 ± 0.12) % normal matter, (25.82 ± 0.69) % dark matter (CDM) and (68.5 ± 1.7) % dark energy (Λ) [5].

Currently, the theory of "primeval atom" is the Big Bang when density and temperature approach infinity in that moment of space and time. It also breaks down the laws of physics. It happened 13.798 ± 0.037 billion years ago, came a hot, dense and expanding universe governed by a hypothetical unified force [6]. After the Big Bang, a phase transition of the inflationary short period (10^{-37} - 10^{-32} s old), the volume of the universe expanded by a factor of 10^{78} and gave a signature of gravitational wave on the CMB [6]. After the era of inflation, the Universe continued to cool and expand creating the proper conditions for the formation of subatomic particles. Producing baryogenesis directly after inflation, leaving a probability of excess of leptons and quarks over anti-quarks and anti-leptons as well as dominance of matter over anti-matter [7]. The expansion still continues and commonly particle energies kept dropping and there is symmetry-breaking phase transitions by factor 10^{-12} – 10^{-6} s old [8].

Astronomical observations are a major way to understand the Universe beyond the earth. A combination of evidence points towards two dark components: dark energy and dark matter. Dark matter behaves like matter but doesn't interact with light and invisible to photon astronomy. Dark Energy is thought of as a fluid with a negative pressure that doesn't dilute as the universe expands. It promotes repulsion and drives the acceleration. While dark matter is theoretically predicted to follow the dilution of all matter, dark energy dominates in the later universe as it is free of z-dependent dilution.

1.1.1 Cosmic Microwave Background (CMB)

Cosmic Microwave Background (CMB) radiation was discovered in 1964 by Penzias and Wilson when they were seeking to understand unexpected noise in a radio antenna when they could not identify the source of an irreducible isotropic (black body spectrum) with a low temperature of 2.725 K as shown in Figure 1.1 [9]. This discovery was the major breakthrough for the acceptance of the Big Band model. Since the CMB in Big Bang cosmological model originates from the surface of last scattering when electrons and protons combined into the neutral hydrogen atoms 380,000 years after the Big Bang, photons do not easily interact with baryons and travel freely. The temperature is about 3,000 K together with the expansion of the Universe.

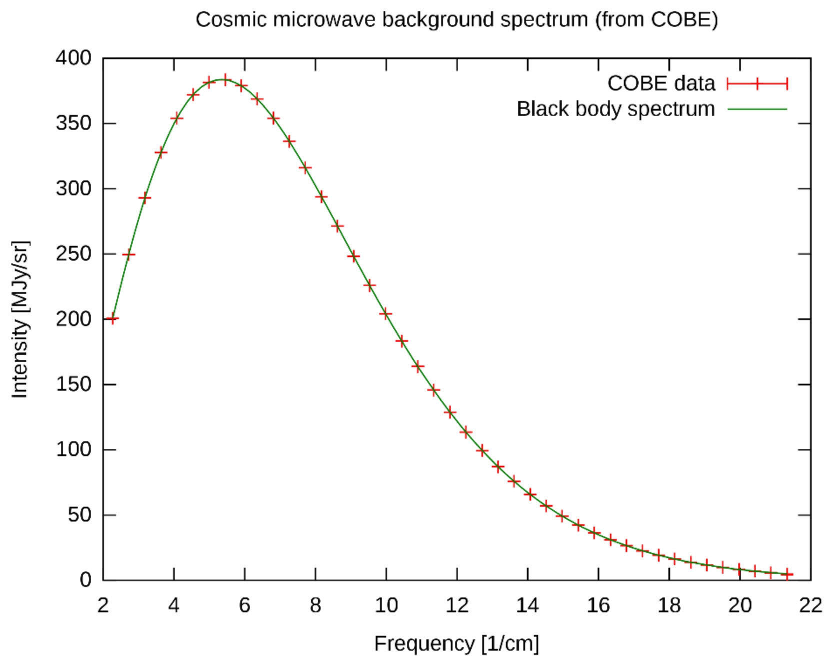

Figure 1.1: The cosmic background radiation. The data showed a perfect fit between the black body curve predicted by the big Bang theory and observed in the microwave background, data from COBE [10].

When looking into the sky at two different directions, the temperature of the CMB is likely the same but not perfect. The deviation of the temperature in direction from its mean value can be defined in terms of spherical harmonics [11]:

$$\frac{\Delta T(\mathbf{n})}{T} = \sum_{l=0}^{\infty} \sum_{m=-l}^{+l} \alpha_{lm} Y_{lm}(\mathbf{n}) \quad (2)$$

The correlation is measured between two directions of *n* and *m* separated by an angle θ (with **n**. **m** = cosθ) [9]. Averaging over all directions separated by this angle gives the correlation function $C(\theta)$ which is commonly expanded in Legendre polynomials $P_l(\cos\theta)$ [12]:

$$\begin{aligned} C(\theta) &= \left\langle \left(\frac{\Delta T(\mathbf{n})}{T}\right)\left(\frac{\Delta \mathrm{T}(\mathbf{m})}{T}\right) \right\rangle \\ &= \frac{1}{4\pi} \sum (2l+1) C_l P_l(cos\theta) \end{aligned} \quad (3)$$

The measured spectrum is then plotted as the multipole moment function (*l*) as shown in Figure 1.2. It can be used to define important properties of the Universe. The largest deviation from black body temperature on the order of 10^{-3} originates from the movement of the Earth relative to the rest frame of the Cosmic Microwave Background. More interesting are the small primordial fluctuations on the order of 10^{-5} as shown in Figure 1.3. They originate from the following effects.

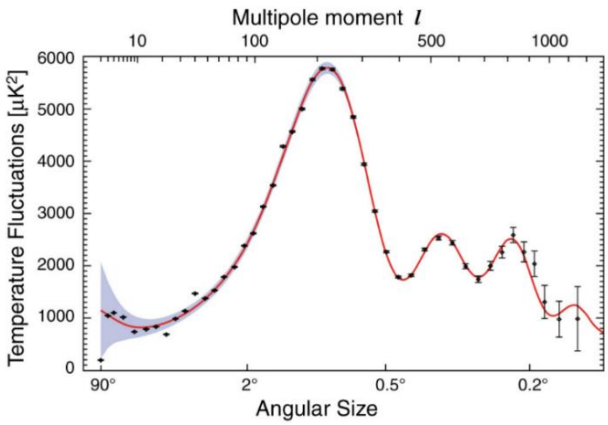

Figure 1.2: The “angular spectrum” of the fluctuations measured by WMAP [13]. Credit: NASA/WMAP Science Team

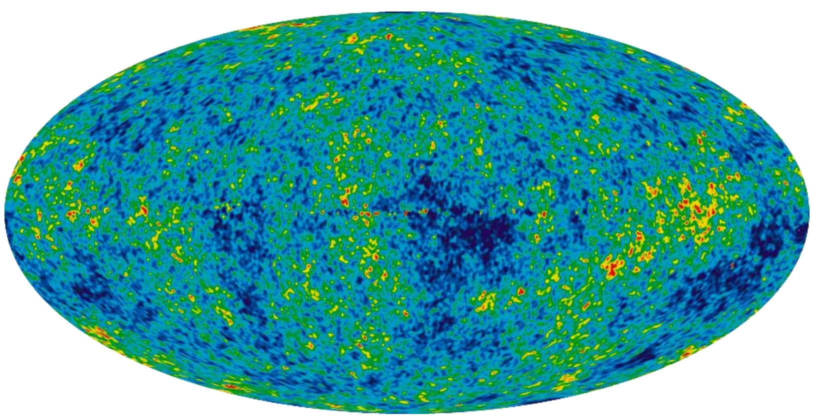

Figure 1.3: Sky map of cosmic microwave background (CMB) as seen by WMAP [14]. Yellow regions appear hotter, dark blue regions cooler at decoupling.

- Intrinsic fluctuations in the temperature at the time of last scattering. This effect is mostly important at small scales [14].
- Fluctuations in the velocity at the time of last scattering, leading to a Doppler shift effect of the photons scattering off the plasma [14].
- Fluctuations in the gravitational potentials at the time of last scattering, following to the Sachs-Wolfe effect. On other words, denser regions are hotter; photons are redshifted, and then appear cooler, less dense regions hotter. This effect dominates the spectrum at large scales [14].

Acoustic oscillations are given the dominant structures: a denser region of the baryon-photon fluid attracts additional baryons then increasing the compression. This is counteracted by the radiation pressure of the photons following acoustic waves. The wave extends as fast as sound can travel so their actual size is given by the sound horizon at the time of last scattering. The Doppler shift can bring the oscillations in the power spectrum out of phase with the temperature oscillations therefore reducing the heights of the acoustic peaks. The higher multipoles can be used to explain many other cosmological parameters [10].

Latest experiments determined that the CMB presents almost perfect black body radiation, as measured by the COBE satellite in 1990. Afterwards detailed investigations of variations in the CMB were undertaken from two experiments, the Wilkinson Microwave Anisotropy

Probe called as (WMAP) and the Planck satellite. The focus was to measure anisotropies in the CMB, which lead to the physics phenomena in the early cosmology [10], [14].

The newest results obtained by the WMAP satellite after 7 years of observation are [15]:

- Baryonic density $\Omega_b = 0.0456 \pm 0.0016$
- Dark Matter density $\Omega_{dm} = 0.227 \pm 0.014$
- Dark Energy density $\Omega_\Lambda = 0.728^{+0.015}_{-0.016}$
- Hubble constant $H_0 = 70.4_{-1.4}^{+1.3}$ km s^{-1} Mpc^{-1}

The baryon density Ω_b is much smaller than the Dark Matter density Ω_{dm}. This means that most of the Dark Matter has to be non-baryonic.

Another hint of non-baryonic Dark Matter is the temperature fluctuations [12]. Baryonic matter can start to clump only after it has decoupled from photons. If the existing structure have created during that amount of time, afterwards the fluctuations at that time would have to be 2 to 3 orders or larger than they actually were.

1.1.2 Big Bang Nucleosynthesis (BBN)

In the beginning era, the Universe was excessively hot for the elements to form. Protons and neutrons remained in thermal equilibrium condition by the weak interaction [12], [16], [17]:

$$\mathrm{n} + \upsilon_e \leftrightarrow \mathrm{p} + e^- \tag{4}$$

Then

$$\mathrm{n} + e^+ \leftrightarrow p + \overline{\upsilon_e} \tag{5}$$

Their relation is given by the Boltzmann factor

$$\frac{N_n}{N_p} = exp\left(\frac{-(m_n - m_p)c}{kT}\right) \tag{6}$$

At about 0.8 MeV above equilibrium reactions freeze out, the neutron fraction is

$$\frac{N_n}{N_p} \approx \frac{1}{5} \tag{7}$$

Deuterons are produced via

$$\mathrm{n} + \mathrm{p} \to \mathrm{d} + \gamma \tag{8}$$

At about 0.05 MeV photon-disintegration of deuterons freezes out and helium production begins, e. g.

$$\begin{gathered} d + d \ \to t + p \\ t + d \to^4 He + n \end{gathered} \tag{9}$$

At this time, the neutron fraction has reduced to ~ 1/7 by decay

$$n \to p + e^- + \overline{\upsilon_e} \tag{10}$$

The mass fraction of ${}^4He$ is given by

$$Y = \frac{4N_{He}}{4N_{He} + N_P} = 0.24 \qquad (11)$$

There are no stable nuclei with number of A = 5 or 8, further nucleosynthesis is limited and mostly takes place in stars and supernovae; another stable element produced primordially in a few quantities is ^7Li, e.g.

$$4_{He} + t \ \rightarrow 7_{Li} + \gamma \qquad (12)$$

The abundances of the light elements depend on the density of baryons in the Universe, as shown in Figure 1.4. By measuring these abundances, the baryons density Ω_b can be determined as, $0.018 < \Omega_b h^2 < 0.023$ [18], [19]. This value is reasonable agreement with the baryon density observed by WMAP but differs substantially from the total matter density $\Omega_m h^2 = 0.1334^{+0.0056}_{-0.0055}$ [15]. This is an independent evidence of the non-baryonic Dark Matter.

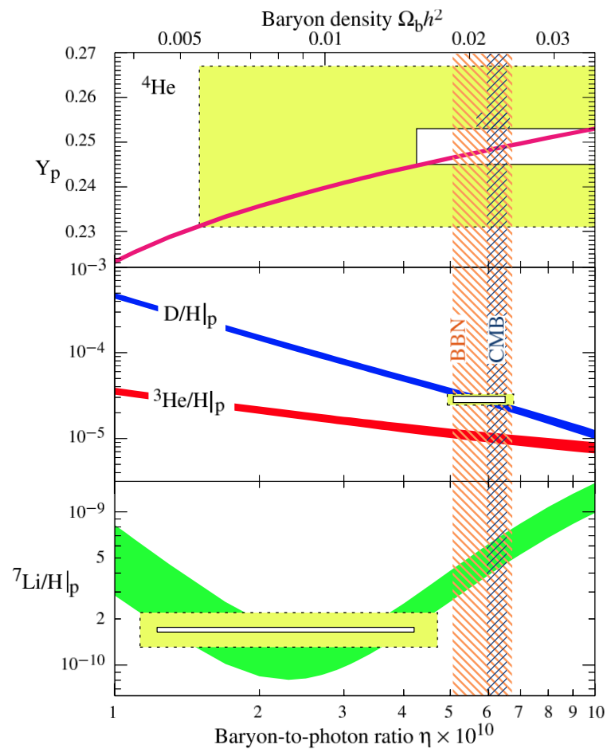

Figure 1.4: Dependence of light elements abundances on baryons density. The bands are the predictions of the BBN at 95% C.L. The vertical bands are the baryon density obtained from the CMB measurements and the BBN concordance range (both at 95% C.L.) [20].

1.1.3 Large Scale Structure (LSS)

Large Scale Structure (LSS) is one of evidences for Cold Dark Matter (CDM). LSS observation map of each galaxy is brighter than a selected threshold and the Redshift Survey is translated to the distance. The field began with the Center for Astrophysics (CfA) Redshift Survey in 1977 [21] and has progressed to the Sloan Digital Sky Survey (SDSS), which has mapped more than 1.5 million spectra to date, shown in Figure 1.5 [22]. LSS have revealed a surprisingly inhomogeneous matter distribution that matches with simulations containing CDM at multiple length scales that they are indistinguishable from the data as shown in Figure 1.5. It contains both data (top, left) and the simulation (bottom, right). The Hot Dark Matter (HDM) simulations do not have enough small-scale structure.

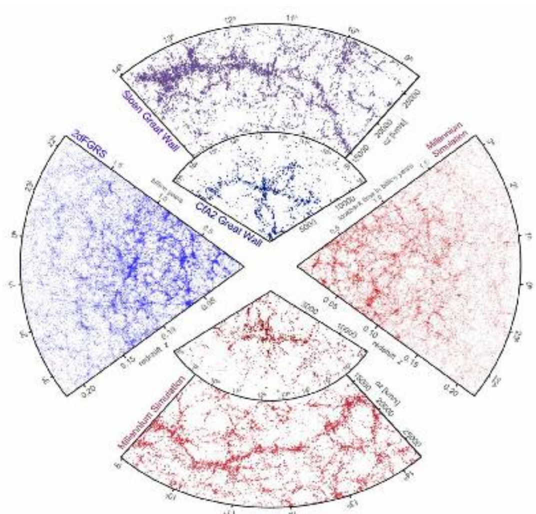

Figure 1.5: Large Scale Structure observed by the Sloan Digital Sky Survey by converting redshift to distance (top, left) [22], [23]. The Numerical process by the simulation (bottom, right) reproduce this inhomogeneity when CDM is included.

1.2 Evidence for the Dark Matter

1.2.1 Virial Theorem

The Virial Theorem relates to the total kinetic energy of a self-gravitating body due to the motions of its constituent parts, $\boldsymbol{T}$ is the kinetic energy, $\boldsymbol{U}$ is gravitational potential energy of the body [24].

$$2T + U = 0 \tag{13}$$

By re-arranging the above equation and making some simple assumptions about

$$\begin{gathered} T = \left(\frac{mv^2}{2}\right) \\ U = \left(\frac{GM^2}{R}\right) \end{gathered} \tag{14}$$

for galaxies, we can obtain:

$$M = \frac{v^2 R}{G} \tag{15}$$

Where $\boldsymbol{M}$ defines the accumulated mass of the galaxy, $\boldsymbol{v}$ defines the mean velocity (together combining the rotation and velocity dispersion) of stars in the galaxy, $\boldsymbol{G}$ defines Newton's gravitational constant and $\boldsymbol{R}$ defines the effective radius (size) of the galaxy. This equation is extremely important as it relates two observable properties of galaxies (velocity dispersion and effective half-light radius) to a fundamental but unobservable, property – the mass of the galaxy. Consequently, the virial theorem forms the root of many galaxy scaling relations [24]. The comparison of mass estimates based on the virial theorem to the estimate based on the luminosities of galaxies is one technique used by astronomers to detect the presence of dark matter in galaxies and cluster of galaxies.

1.2.2 Galaxy rotation curve

Observation of the rotation curves of stars in spiral galaxies gives one of the best pieces for the existence of Dark Matter [25]. The visible part of spiral galaxies consists of a central bulge and a thin disk. The tangential velocity $\upsilon(\mathrm{r})$ of a star with mass (*m*) revolving in a galaxy with mass *M(r)* at a distance (*r*) from the galactic center can be defined by the equation involving gravitational and centrifugal forces [12].

$$\frac{m\upsilon^2}{r} = \frac{GmM(r)}{r^2} \tag{16}$$

to be

$$\upsilon(\mathrm{r}) = \sqrt{\frac{\mathrm{GM(r)}}{\mathrm{r}}} \tag{17}$$

as

$$\mathrm{M(r)} \equiv 4\pi \int \rho(\mathrm{r}) r^2 \mathrm{d}r \tag{18}$$

with $\rho(r)$ the mass density profile of the galaxy,

$$M(r) \propto r^3 \quad (19)$$

inside the visible bulge of the galaxy and constant outside.

Therefore, the velocity $\upsilon(r)$ should directly proportional to r inside the visible bulge and inversely proportional to $\frac{1}{\sqrt{r}}$ outside. However, $\upsilon(r)$ is determined, by observation of the redshift from the 21 cm hydrogen line showing that the velocity remains constant up to large radii, implying that

$$M(r) \propto r \quad (20)$$

An astronomer Vera Rubin from the USA discovered the discrepancy between the predicted angular motion and the observed motion of galaxies by observing the galactic rotation curves in the late 1970s. Rubin confirmed that the optical region rotation curves are flat compare to the visible edge of spiral galaxies. Recent observation found that there was much more gas than stellar mass in these structures, at least of 80 % of the mass belonging to a dark component [12]. An example of a rotation curve is shown in Figure 1.6.

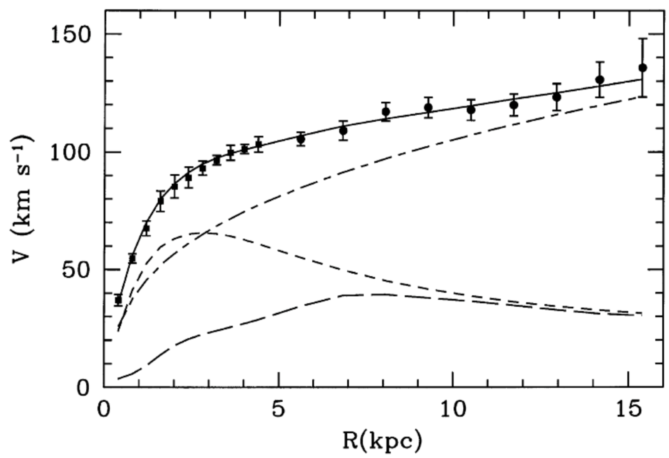

Figure 1.6: M33 rotation curve (black dot-points) compared with the best-fitting model (solid line). Others are the halo contribution (dot-dashed line), the gas contribution (long-dashed line), and the stellar disc (short-dashed line) [26].

1.2.3 Bullet clusters

The most convincing evidence for the existence of Dark Matter has been obtained by observation of 1E 0657-558 (z=0.296), called as the "bullet cluster", a merger of two galaxy clusters occurred 10^8 year ago, as shown in Figure 1.7. [27]. Another observation on the MACS J0025.4-1222 cluster (z=0.586) has now confirmed these findings [28].

When the chance of two galaxies colliding each other, stars act like collision-less particle because of its size which isn't comparable in galactic scale, while the hot X-ray emitting inter-galaxy gas acts as a fluid which experiences pressure and is therefore slowed down during the collision. In theoretical models Dark Matter is expected to be collision less. Since it would take some time until the galaxies and the gas are virialized again, the distribution are spatially separated in the Bullet Cluster. Without including Dark Matter, one would expect that the gravitational potential follows the inter-galaxy gas, which accounts for about 5 times the mass of the stars in the galaxies [29], [30]. However, the gravitational potential which follows the distribution of the galaxies has been found, which is a strong evidence of collision less Dark Matter and rejects the most alternative gravitational theories such as MOND.

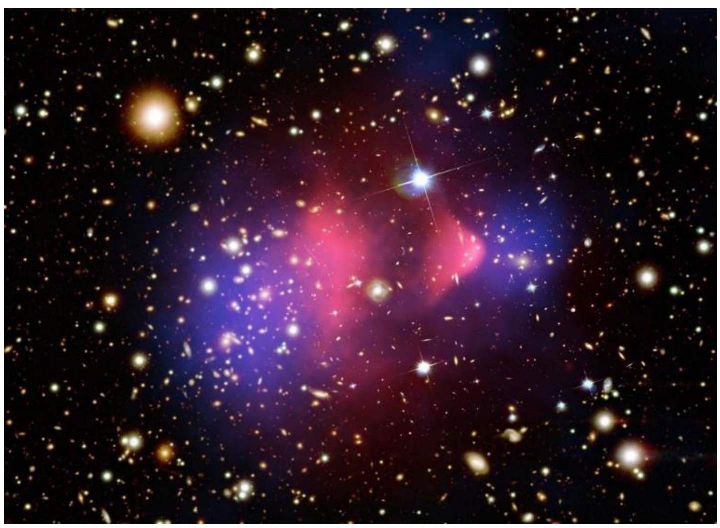

Figure 1.7: The bullet cluster, in which the galaxies (white and orange) and the intergalactic gas (pink) are still separated. The mass distribution (blue) as obtained by gravitational lensing. This is the best evidence for the existence of Dark Matter [31].

1.2.4 Gravitational lensing

If a photon passes by an object at minimum distance *b* its flight path will be deflected by an angle [12], [32], [33].

$$\alpha = \frac{4GM}{bc^2} \qquad (21)$$

(*G* is Gravitational constant; *c* is speed of light). The object behaves as a gravitational lens, the mass can be determined from the formula by measuring the angle of deflection. If the object is more massive, a galaxy cluster of a black hole, a multiple image of the photon source will appear or in another case (if the gravitational lens and the observer are collinear) predicted as an Einstein ring. This is strong of gravitational lensing. As shown in Figure 1.8., if the lens is a star the deflection is too small to be observed but if the star moves past in the line of sight, a partial change in the luminosity of the source can be measured. This is so-called “microlensing”. If the light from certain distant sources passes by many lenses on its way to Earth, the distortion of the pictures can be studied to obtain information on the Large-Scale Structure (LSS), by *weak* gravitational lensing [11].

Gravitational lensing has been observed with quasars as sources at the first time on cosmological scales [34]. At the time, microlensing has been used to detect baryonic Dark Matter in the non-luminous matter of astrophysical objects called Massive Astrophysical Compact Halo Objects (MACHOs). MACHOs can be formed from brown dwarfs, neutron stars and white dwarfs, faint red dwarfs or black holes. Those masses are massive between

0.001 - 1 $M_{\odot}$. Observations show that they could contribute anything from (almost) 0 up to 20 % of the Dark Matter in the galaxy [35], [36]. Hubble Space Telescope data give an upper limit of <1 % of the mass of the galactic halo [37], therefore MACHOs cannot be significant contribution to Dark Matter form.

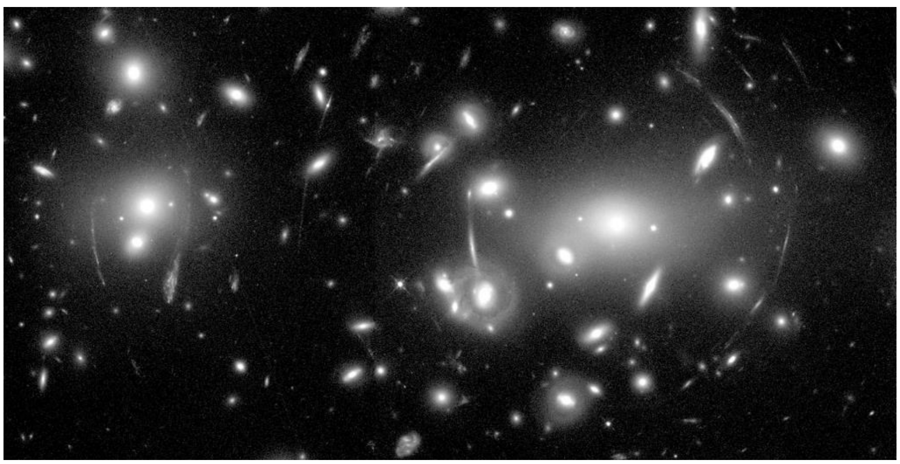

Figure 1.8 Gravitational lensing in Abell 2218 as observed by the Hubble Space Telescope [38]. The arcs are parts of an Einstein Ring.

1.3 Dark matter candidate

Currently, there is no theoretical model of the nature of dark matter, but only the required energy densities on the scale of galaxies. Particle for dark matter is the logical continuation cosmology, there are a lot of theories which predict particle that could be form for dark matter. In particular, supersymmetric theories would be an interesting addition of the standard model, by adding a super-partner to each particle at standard model to be ‘mirrored’ properties.

Dark Matter candidates must not be from SM particle and fulfill certain characteristics. They are expected massive to match with observations of gravitational anomalies and structure formation, gluons, eliminating photons and neutrinos as candidates. They exclude the charged leptons, quarks, and W bosons from the candidates. Dark Matter cannot be from baryonic matter, it is also stable. Additionally, a possible search with detection methods are required to probe the existence of dark matter halo.

1.3.1 Baryonic dark matter

The density of baryons can be calculated from the Cosmic Microwave Background (CMB) and Big Bang Nucleosynthesis (BBN) and is about 4.5 % of the density. This is bigger than the visible baryon density to be 0.3 % [39] so some of the dark matter must be baryonic. Other possible candidates are MACHOs as observed by gravitational lensing but the total density of dark matter is 22.7 % of density [15]. This is much larger than the total density of baryons, therefore most of the dark matter has to be non-baryonic. As a conclusions, non-baryonic density must be form of the Dark Matter.

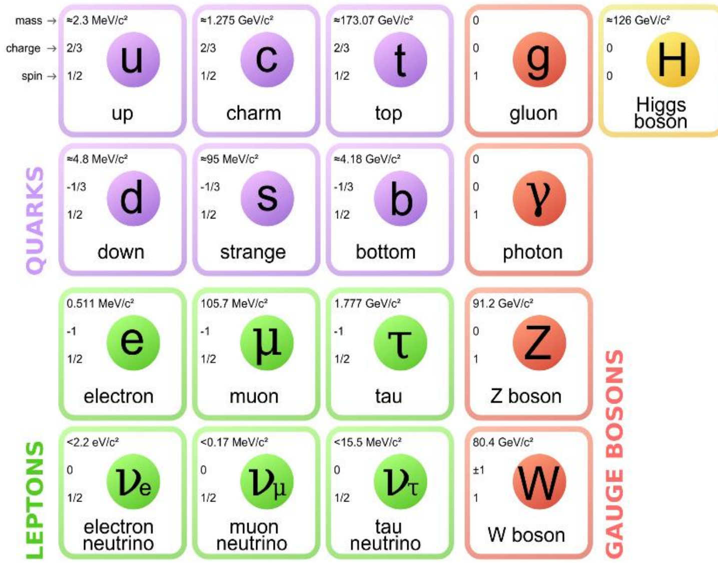

Figure1.9: Standard model of elementary particles.
Source:https://en.wikipedia.org/wiki/Standard_Model

1.3.2 Neutrinos

Neutrinos have one big advantage compared to other non-baryonic Dark Matter candidates; they are already known to exist as clearly observed by Standard Model of particles. Similar to the CMB, cosmic neutrino background is providing 339 neutrinos and antineutrinos per cm^3 [12]. Unfortunately, the mass of the neutrinos are extremely small in comparison to the missing mass and the neutrinos as the candidate for Hot Dark Matter, which is excluded by structure formation. Direct mass measurements limit their masses to 2 eV [20] and further experiments that is sensitive to neutrino masses on the order of 0.2 eV are on operation [40], [41]. Observations of cosmic microwave radiation, baryon acoustic oscillations and supernovae limit the neutrino density even to $\Omega_\upsilon h^2 < 0.0062$ [15], which means other Dark Matter candidates are necessary. There are no other particles with the required properties available in the Standard Model. It has to be neutral, non-baryonic, massive, and non-decaying which is beyond the Standard Model.

1.3.3 Weakly Interacting Massive Particles (WIMPs)

Weakly Interacting Massive Particle (WIMP) dark matter candidates can fill the criteria outlined by Cold Dark Matter (CDM) and return the correct relic density under the assumption. It is the model predicted by supersymmetry (SUSY). Supersymmetry is also hypothetical-extension of the Standard Model of particle physics to solve some of its problems such as the hierarchy problem, possibly the inclusion of gravity into the theory and the question of gauge coupling unification [18], [42], [43].

In the SM, all elementary matter particles (including quarks and leptons) are fermions and all interaction are mediated by exchange particles (bosons). There are fermions, bosons and the Higgs particle. This super-partner model should have the same quantum numbers including mass but not the spin, similar with the original particle, but particles with these properties are not observed yet in nature. Therefore, SUSY has to be broken allowing the superpartners to be more complex than the corresponding Standard Model particles.

WIMPs are produced thermally in the beginning of the Universe. As WIMPs cluster, that should be a massive in our galaxy of the galactic halo. The Earth moves around the Sun at

30 km/s and the Sun moves around the galactic center at 220 km/s. Due to the seasons these velocities either add up or down in opposite directions, the velocity of the Earth relative to the galactic halo varies at the year. This leads to the expected energy spectrum of annual modulation that comes from WIMP recoils by scattering in a target to be about 7 %. The observation of annual modulation can be used as a signature in WIMP direct searches.

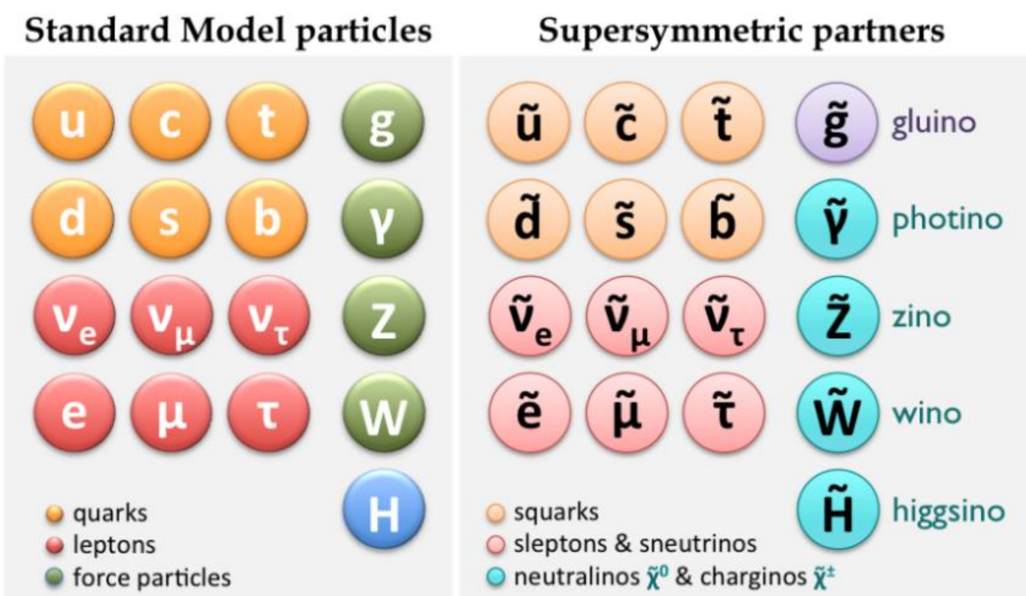

Figure 1.10. Standard model of elementary particles with super symmetry.

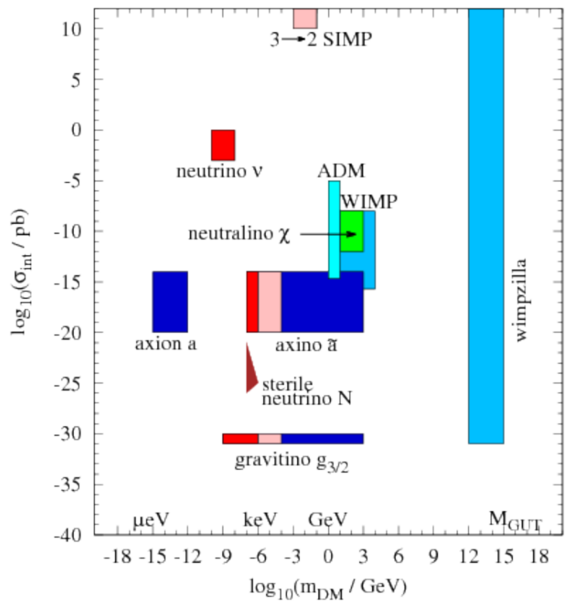

Figure 1.11: Dark matter candidates, with its interaction cross-section on y-axis and particle mass on the x-axis based on theoretical model. The WIMP (including neutralino) and the axion are preferred candidates [32] .

1.3.4 Axions

Axions represent a class of non-thermal dark matter particles. They result from the strong CP problem and are hypothetical light bosons produced with a low momentum. Therefore, they can be categorized as a cold dark matter component depending on the axion mass. In the mass range between about 10^{-6} and 10^{-3} eV, the axion could contribute a large part to Ω_M [44].

Solar axions are typically not considered as cold dark matter, nevertheless the proof of their existence via detection would be interesting. The sun is the strongest and closest source of axions, where they are produced by the Primakoff effect via scattering photons in the strong electromagnetic field of a nucleus Ze.

$$\gamma + Ze \leftrightarrow Ze + A \tag{22}$$

There are astrophysical limits on the creation of axions in stars, which result from the fuel burning cycles, as axions would constitute a way of energy loss from a star [45].

1.4 Direct Detection Techniques

1.4.1 Standard Halo Model

The Standard Halo Model (SHM) was introduced into cosmology and astroparticle physics over thirty years ago [23]. The velocity distribution of the dark matter $f_R(v)$ is a Gaussian in the Galactic frame

$$f_R(v) = \frac{1}{(2\pi\sigma_\upsilon^2)^{\frac{3}{2}} N_{R,esc}} \exp\left(-\frac{|v|^2}{2\sigma_\upsilon^2}\right) \times \Theta(\upsilon_{esc} - |v|) \tag{23}$$

where σ_υ is the isotropic velocity dispersion of the DM, $\sigma_0 = \sqrt{2\sigma_\upsilon}$ is the value of the asymptotically flat rotation curve. The isothermal spheres have infinite extent whereas Galaxy halos are finite. This is achieved in the SHM by truncating the velocity distribution at the velocity escape (speed υ_{esc}), using the Heaviside function Θ. The constant $N_{R,esc}$ is used to renormalize the velocity distribution after truncation,

$$N_{R,esc} = erf\left(\frac{\upsilon_{esc}}{\sqrt{2\sigma_{\upsilon}}}\right) - \sqrt{\frac{2}{\pi}}\frac{\upsilon_{esc}}{\sigma_{\upsilon}}exp\left(-\frac{\upsilon_{esc}^2}{2\sigma_{\upsilon}^2}\right) \quad (24)$$

To describe the velocity distribution of DM in the galactic frame under the SHM, we need to prescribe two parameters, υ_0 and υ_{esc}. These quantities in the SHM are following:

Local DM density	ρ_0	0.3 GeV cm^{-3}
Circular rotation speed	υ_0	220 km s^{-1}
Escape speed	υ_{esc}	544 km s^{-1}
Velocity distribution	$f_R(v)$	Equation 23

Current theories of galaxy formation in the cold dark matter paradigm envisage the build-up of DM halos through accretion and merger. WIMP direct detection searches have traditionally taken ρ_0 = 0.3 GeV cm^{-3} for the local DM density.

1.4.2 WIMP-nucleous interaction

The signal of a direct detection technique is the recoil energy E_r deposited as the WIMP scatters off a target nucleus in the detector material. Assumming of elastic scattering, the recoil energy may be determined kinematically:

$$E_r = \frac{m_\mu^2 \upsilon^2}{m_n}(1 - \cos\theta) \tag{25}$$

where υ is the velocity of the WIMP relative to the nucleus, θ is the scattering angle in the center-of-mass frame and m is a mass term for the WIMP (χ) or target (n). The WIMP-target reduced mass, $m_\mu = \frac{(m_\chi m_n)}{(m_\chi + m_n)}$, conveniently simplifies the above relation.

Normally, the WIMPs are not mono-energetic, but follow a Maxwell-Boltzmann distribution of velocities so it is necessary to integrate over this distribution. The differential rate $\left(\frac{dR}{dE_r}\right)$of WIMP elastic scatterings off nuclei in the detector target is determined by:

$$\frac{dR}{dE_r} = N_n \frac{\rho_0}{m_\chi} \int_0^{\upsilon_{esc}} d\upsilon f(\upsilon) \upsilon \frac{d\sigma}{dE_r} \tag{26}$$

where N_n is the number of target nuclei in the detector, ρ_0 is the local WIMP density, $\frac{d\sigma}{dE_r}$ is the WIMP-nucleus differential cross section, and υ_{esc} is the escape velocity of WIMPs in the galaxy. The velocity distribution, $f(\upsilon)$, must be changed from the rest-frame Maxwell-Boltzmann to include the sun's rotation about the galactic center.

The scattering rate provides without considering the instrumental effects. A lower integration limit can be introduced because any physical detector has its own trigger energy threshold (E_{th}) below which it does not collect the signals. This minimum velocity (υ_{min}) can be derived from maximizing Eq. 25 when $cos\,\theta = -1$:

$$\upsilon_{\mathrm{min}} = \sqrt{\frac{\mathrm{m}_n \mathrm{E}_{\mathrm{th}}}{2\mathrm{m}_{\mu}^2}} \tag{27}$$

Real detector should also consider the trigger efficiency, which is typically a rapidly varying function near the energy threshold.

The particle events of WIMP-nucleus scattering enter Eq. 26 in the final term, the scattering cross section $\left(\frac{d\sigma}{dE_r}\right)$. The most common WIMP models predict the cross section will be dominated by scalar (spin-independent) and axial-vector (spin-dependent) couplings. The differential cross section is most often written in terms of the momentum transfer, $q(q^2 = 2m_T E_r)$, with both spin-dependent and spin-independent terms as,

$$\frac{d\sigma}{dq^2}(q^2, \upsilon) = \frac{1}{4\mu^2\upsilon^2}\left(\sigma_{SI}^0 F_{SI}^2(q) + \sigma_{SD}^0 F_{SD}^2(q)\right)\Theta(q_{max} - q) \tag{28}$$

where $\sigma_{SI}^0\left(\sigma_{SD}^0\right)$ is the zero momentum considering transfer spin-independent (spin-dependent) cross section, $F^2(q)$ is the appropriate form factor, and Θ is the Heaviside step function. The presence of the form factor in Eq. 28 accounts for the finite size of the nucleus;

$F^2 \approx 1$ for small momentum transfer but decreases as the de Broglie wavelength (λ) of the momentum transfer which is comparable to the size of the nucleus [46].

Target nuclei of detector have different sensitivity for spin independent and spin dependent scattering based on the nuclear spin and number of nucleons. A direct search experiment considers different target nuclei to enhance one or both of these interactions [47].

1.4.2.1 Spin-independent of Elastic Scattering

The term spin-independent, or scalar, coupling appear from coherent scattering of a WIMP with the target nucleus. This provides a critical enhancement to the cross section with increasing target number of nucleons

$$\sigma_{SI}^0 = \frac{4m_\mu^2}{\pi}\left(Zf_p + (A - Z)f_n\right)^2 \tag{29}$$

where $Z(A - Z)$ is the number of protons (neutrons), $f_p(f_n)$ is the effective coupling to the proton (neutron). The most basic models will typically assume that $f_p = f_n$, which simplifies the spin-independent cross section to $\sigma_{SI}^0 \propto A^2$.To penalize the experimental results, suggestions of $f_n = -0.7f_p$ have been used to remove spin-independent sensitivity from heavier nuclei (Xe-based experiments currently providing leading sensitivity) [47].

The form factor that describes the dependence on momentum transfer may be reduced with reasonable accuracy to an exponential form:

$$F(q) \approx e^{\frac{-q^2}{q_0^2}} \tag{30}$$

where q_0 is related to the size of the nucleus.

The combined effect on Eq. 29 and Eq. 30 is that all target nuclei show a similar exponential spectrum, but with normalizations defined by the A^2 enhancement favors Xenon. The large momentum transfer affects strongly due to the exponential penalty so that Xenon spectrum fall off more quickly. The current generation of direct detection experiments places greater emphasis on spin-independent interactions because the A^2 enhancement allows them to probe more extreme cross section [18].

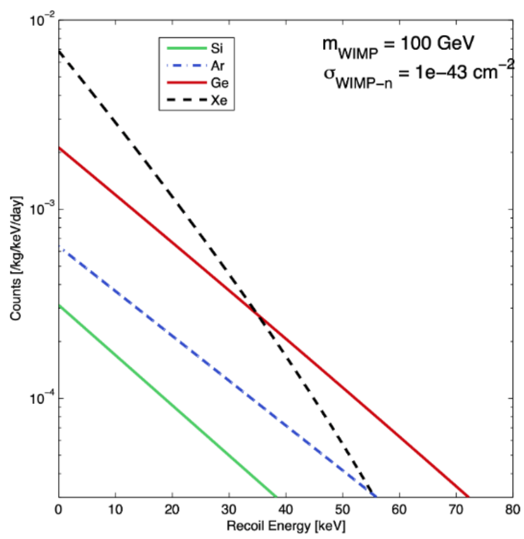

Figure 1.12: Differential WIMP recoil energy spectrum for the commonly studied nuclei with the WIMP mass of 100 GeV and a WIMP-nucleon cross section $\sigma = 10^{-43}$ cm^2. [47].

1.4.2.2 Spin-Dependent of Elastic Scattering

The spin-dependent, or axial-vector, coupling arises from interaction of a WIMP with the total spin of the nucleus:

$$\sigma_{SD}^{0} = \frac{32 m_{\mu}^{2} G_F^{2}}{\pi} J(J+1)\Lambda^{2} \tag{31}$$

Where, G_F is the Fermi constant, J is the total spin of the nucleus and

$$\Lambda = \frac{1}{J}\left(a_p\langle S_p\rangle + a_n\langle S_n\rangle\right) \tag{32}$$

Here $\langle S_p\rangle(\langle S_n\rangle)$ is the average spin contribution from the proton (neutron) group, and $a_p(a_n)$ is the effective coupling to the proton (neutron). Several models allow few factors differ between a_p and a_n to simplify the model so that spin-independent case becomes impossible.

At many models, the spin-independent coupling to a proton is greater than the spin-dependent ($\mathcal{O}(10^2 - 10^4$) for a MSSM neutralino), but the spin-independent scattering will still dominate. The spin-independent scattering is greatly enhanced by A^2 factor. The spin-dependent scattering must rely on $\mathcal{O}(1)\langle S_p\rangle$ and $\langle S_n\rangle$ terms, and often suffers from the isotopes with zero spin [46].

Since the form factor punishes large momentum transfer, it is benefit to select a light nucleus with nuclear spin. Fluorine is commonly used for target of spin-dependent work, because ^{19}F has ~100 % natural abundance, is low-mass (high spin/mass ratio), and forms a variety of molecules with carbon [48].

1.4.2.3 Inelastic Dark Matter scattering

It was first suggested to reconfirm the tension between a positive claim (DAMA) and the claimed exclusion of that result by another (CDMS) [49].

This model postulated a doublet of WIMP states, χ_- and χ_+ in which χ_+ is slightly heavier by a mass splitting δ. If scattering is allowed for χ_- upscattering into the χ_+ state, an additional kinematic constraint is imposed on the WIMP interactions:

$$\delta < \frac{\beta^2 m_\chi m_n}{2\left(m_\chi + m_n\right)} \tag{33}$$

Where m_n and m_χ are the masses of the target and WIMP respectively. This constraint increases the minimum considered WIMP velocity (υ_{min}) to:

$$\upsilon_{min} = \frac{1}{\sqrt{2m_n E_{th}}}\left(\frac{m_n E_{th}}{m_\mu} + \delta\right) \tag{34}$$

where E_{th} is the energy threshold and m_μ is the WIMP-target reduced mass. The effect of inelastic dark matter was to penalize lighter targets by increasing the minimum velocity to provide detectable signals and reducing the total event rate. With improved sensitivity of experiments with high-mass xenon material targets, the simple models of inelastic dark matter have been excluded.

1.4.3 Annual Modulation of Dark Matter

The WIMP flux on Earth is expected to modulate annually due to changes in the velocity of the Earth around the Sun. It is from the combination of the Earth's two orbits: First, around the Sun and the other around the center of the galaxy together with the sun. The Earth should see a WIMP at maximum rate in June, when the Earth motion around the Sun is in the direction of the galactic rotation velocity (increasing its effective velocity with correspond to a galactic halo WIMP). Furthermore, there should be a minimum WIMP rate in December when the Earth's velocity is directed, decreasing its effective velocity. The Earth's velocity in the galactic frame is

$$\begin{aligned} \upsilon_e(t) &= \upsilon_{\odot} + \upsilon_{\oplus} \mathrm{x} \cos \gamma \cos \omega(t - t_0) \\ &= 232 + 15\cos\left(2\pi \frac{\text{t-152.5}}{365.25}\right) \end{aligned} \quad (22)$$

Where $\upsilon_{\odot}$ is the Sun's velocity with correrspond to the galactic halo; $\upsilon_{\oplus}$ is the Earth's velocity around the Sun with an inclination of 60.2° with correspond to the galactic plane;

$\omega = \frac{2\pi}{1\ \text{yr}}$ is the frequency of the orbit, and t_0 is that time when the Earth's galactic speed is maximal in early June [47]. These calculations predict the modulation of the WIMP signal with a 1-year period and has a maximum in early June. Additionally, WIMP signal should be a single-scatter events, should be found in the expected WIMP-induced recoil signal region and modulate with an amplitude $\leq 7\ \%$ [47].

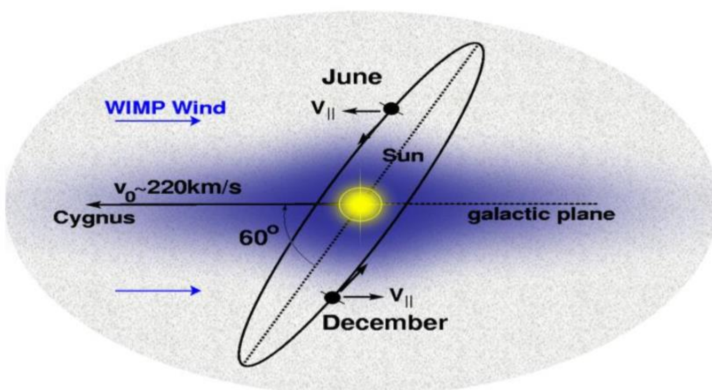

Figure 1.13: Illustration of Earth's relative velocity to WIMP direction that is signature to annual modulation in dark matter signal [47].

1.5 DAMA/LIBRA Experiment and Annual Modulation

Among dark matter experiments, DArk Matter (DAMA) is the only direct searches experiment which has claimed a discovery of dark matter signature. Several other experiments with better sensitivity and large exposure, projecting the WIMP parameters which are capable of producing the observed DAMA signal and didn't claim discovery. DAMA/LIBRA has run at the Laboratori Nazionali del Gran Sasso (LNGS) underground laboratory with an water equivalent of 3400 m in three phase and has released the newest result in 2018. Low energy (2-6 keV_{ee}) is the region which DAMA is interpreting as their signal region with phase 1. They lowered their analysis threshold from 2 keV to 1 keV in phase 2 result. The observed modulation signature at DAMA phase 1 is persistent with phase 2 over 20 annual cycles [50], [51].

DAMA/NaI (1996-2002) ran with 9.70 kg crystals in a 3 x 3 array for a total mass of 87.3 kg. It collected data over 7 annual cycles with a WIMP signal in the 2-4 keV range to 5.0 σ significance [50].

DAMA/LIBRA-phase1 (2003-2010) was upgraded from DAMA/NaI setup with new PMTs and 242.5 kg of lower NaI(Tl) crystals. DAMA/LIBRA reported data over 7 annual cycles for a total exposure of 1.04 ton. Years and observed 8.1 σ modulation in the 2-4 keV range which is consistent with the WIMP signal observed by DAMA/NaI [49]. The combined results of DAMA/NaI and DAMA/LIBRA reaches 9.5 σ from 2-4 keV [49].

DAMA/LIBRA-phase2 (2010-2018) was upgraded with higher quantum efficiency PMTs, lowering the software threshold from 2 keV to 1 keV. Phase2 reported over 6 annual cycles corresponding to a total exposure of 1.13 ton. Years and observed with the significance of 9.5 σ in the region of 1-6 keV.

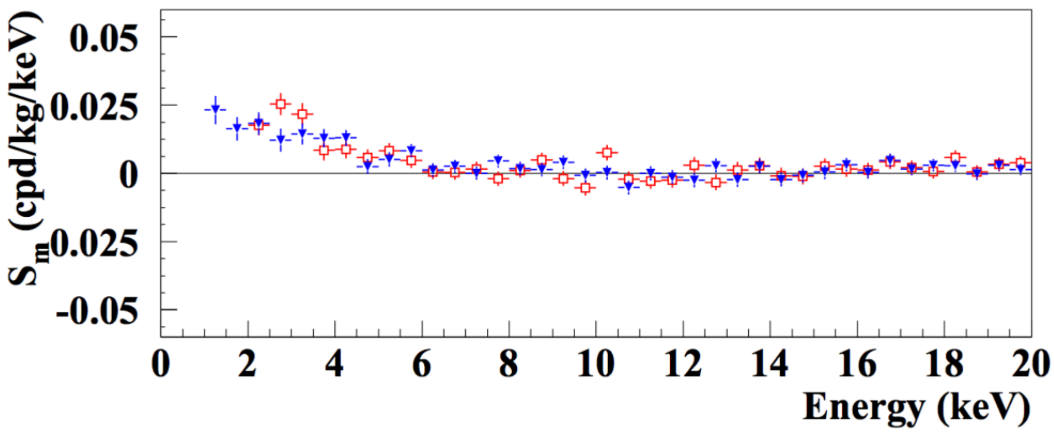

Figure 1.14: Modulation amplitude as a function of the energy for the single-hit scintillation events. (red-point) result from DAMA/LIBRA phase1 with 2keV threshold, (blue-point) result from DAMA/LIBRA phase2 with 1 keV threshold [50], [51].

Total accumulated data from DAMA/NaI and DAMA/LIBRAphase1+phase2 showed the single-hit residual rates is (0.0103 ± 0.0008) cpd/kg/keV, the measured phase is (145 ± 5) day and the measured period is (0.9987 ± 0.0008) year with the significance of 12.9 σ, all these values are in good agreement with those expected for dark matter particle interactions. DAMA/LIBRA claimed no systematics or side reaction that can mimic the extracted dark matter induced annual modulation signal [50].

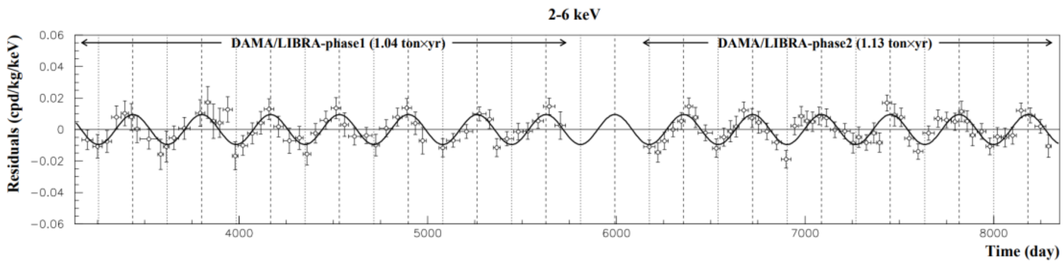

Figure 1.15: Experimental residual rate of the single-hit scintillation event measured by DAMA/LIBRA-phase1 and phase2 in the (2-6) keV energy intervals as a function of the time. The superimposed curve is the sinusoidal function with a period is 1 yr, a phase 152.5d (June 2^{nd}) and modulation amplitude [51].

The DAMA signal stirred up controversy in the astronomical society because no other search experiments have been able to observe the signal by using different target detector (liquid, gas, solid detector). It increased the tension in the field as new experiments continue to report conflicting phase space limits. Possible modulating backgrounds proposed to confirm and explain the DAMA signal have included, among others, seasonal variation in: muon flux & modulation, scintillator phosphorescence effects, ambient temperature, spallation neutrons from muons in the surrounding rock etc. But, DAMA refused many of these proposals, and has been in constant debate.

Verification of the DAMA results with a new NaI(Tl) WIMP search detector would require an independent development of low-background crystals. The crystal-growing company that supplied the DAMA NaI(Tl) crystals no longer produce similar-grade crystals.

Currently, several experiments are under R&D and are going to operate direct search with Thallium-doped NaI detector as the target media. ANAIS [52], DM-Ice [53], KamLAND-PICO [54], SABRE [55], and KIMS [56] have been worked to develop low-background detector NaI(Tl) suitable for reproducing the DAMA signal. Among these groups, the COSINE-100 experiment is a joint effort between KIMS and DM-Ice to confirm or refute the annual modulation signal observed by the DAMA/LIBRA experiment [57]–[60].

All of the measurements summarized with upper limits on the cross section based on null experimental results except for positive signals from the DAMA/NaI and DAMA/LIBRA experiments for which contour indicating allowed cross section vs WIMP mass regions are shown [61].

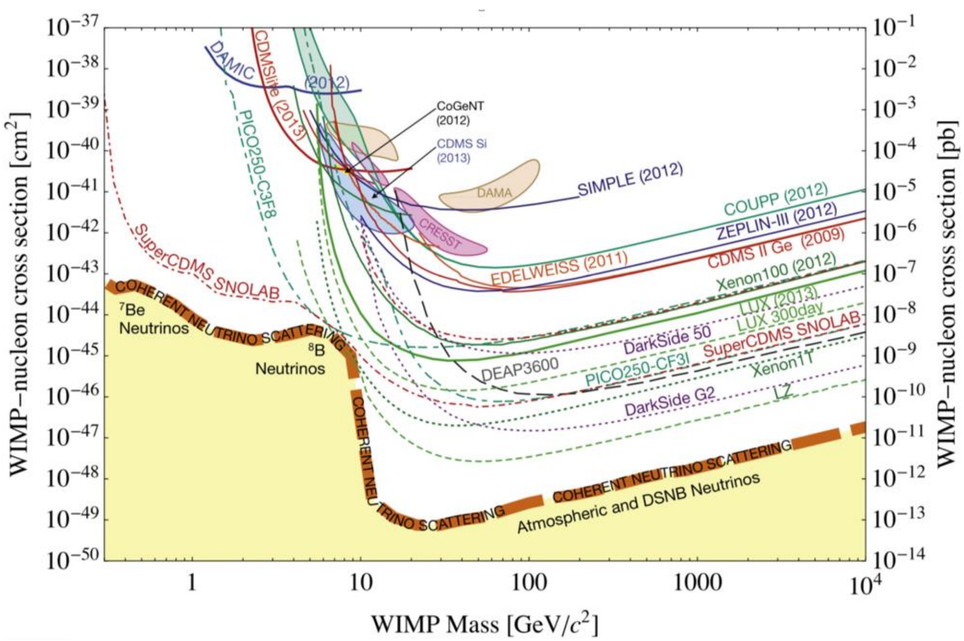

Figure 1.16: A collection of the WIMP-nucleon spin-independent cross section limits (solid lines) and hints of WIMP signals (closed counters) from current dark matter search experiments and projections (dashed) for planned direct detection dark matter experiments. The yellow band shows the approximate neutrino coherent scattering floor from atmospheric neutrinos, solar neutrinos and diffuse supernova [61].

Chapter 2

The COSINE-100 Experiment

DAMA/LIBRA collaboration installed ~250kg of NaI (Tl) detector in an array of 5 by 5 crystals at the Gran Sasso underground laboratory and running continuously since September 2003. The experiment searches for an annual modulation to detect the rate of nuclear recoils in the NaI (Tl) crystals caused by Earth's orbital motion through our Galaxy's dark-matter halo. The DAMA collaboration has claimed a positive evidence for WIMP signal via annual modulation detection for more than 14th cycles with a phase that is consistent with expectations for halo model. The modulation is persistent below 6 keV and much stronger at low energy while it shows null modulation above 6 keV. The statistical significance of the DAMA annual modulation signal with phase reached to 9.3σ [62]–[64].

The DAMA signal is interpreted as a result of WIMP nucleus scattering. This interpretation is not widely accepted because the WIMP-nucleon cross sections inferred from the DAMA/LIBRA modulation are in conflict with limits from other experiments that directly measure the total rate of nuclear recoils, such as XENON100 [65], LUX [66], and SuperCDMS [67]. The different target may response differently for specific WIMP model. So, an independent NaI(Tl) low background crystal experiment is necessary to resolve this conflicts.

The Korea Invisible Mass Search (KIMS) Collaboration is putting its effort on R&D of NaI (Tl) detectors at Yangyang Underground Laboratory (Y2L), Korea from 2012. The goal of the KIMS experiment is to confirm or reject the DAMA interpretation of the dark matter induced annual modulation signal. Extensive work is necessary to reproduce DAMA experiment to achieve ultrapure NaI(Tl) crystals independently. A coordinated R&D between ANAIS [68], [69], DM-Ice [53], [70] and KIMS collaborations [56], [71] to get very low background level crystals with a private crystal growing company "Alpha spectra" demonstrated the possibilities to reproduce DAMA experiment.

Several R&D crystals grown by the Alpha Spectra company from Colorado USA, Bejing Hamamatsu, and SICASS company from China were tested by KIMS collaboration between 2013 to 2015. The R&D crystals were installed to the existing shielding facilities of KIMS CsI experiment [72] within CsI array. The detector assembly, DAQ response and internal background is well understood after testing 15 R&D crystals. Background data is reproduced by using Geant4 based Monte Carlo simulation.

The first generation of the experiment with 17 kg of NaI(Tl) crystal from DM-Ice collaboration is successfully deployed at the South pole and collected data from 2011. The DM-Ice17 data with an exposure of 60.8 kg year demonstrates the detector stability and possibilities of the NaI(Tl) experiment at the southern hemisphere which is a strong foundation for future experiments. The DM-Ice17 data is inconsistent with the DAMA annual modulation signal in the range of 4 to 20 keV region.

The R&D experience by KIMS-NaI and DM-Ice give a solid baseline for the possibilities of replicating the DAMA experiment. The joint venture between KIMS-NaI and DM_Ice collaboration so-called COSINE-100 collaboration is established in 2015 to confirm or refute the claim made by DAMA about the annual modulation.

2.1 Experimental site for COSINE-100

The COSINE-100 experiment use the Yangyang pumped storage power plant site under Mount Jumbong with a granite overburden of 700 m which is located at Yangyang Underground Laboratory (Y2L), Yangyang Korea. There are two tunnels called A5 and A6 tunnel, the COSINE-100 experiment is installed at the A5 tunnel and the R&D setup is running at the A6 tunnel. The muon flux of the experiment hall is estimated as $4 \times 10^{-3} m^{-2} s^{-1}$ [58]. To isolate the system from atmosphere that contains a large amount of dust and backgrounds, the room is designed to be self-contained and the dust bigger than 0.5 μm per cubic meters is passed below 1500 cubic feet. Several sensors are located at a different location inside the experiment hall to monitor the temperature and humidity. The detector shielding is maintaining with the temperature fluctuation within ±1.0 °C, a humidity within ±3.0 % level, and radon level below 40 Bqm^{-3}. Since the crystal detector array is submerged in a large volume of a scintillating liquid which has a relatively high heat capacity, the temperature variations near the crystals are reduced compared to the room temperature variation and are measured to be ±0.1 °C.

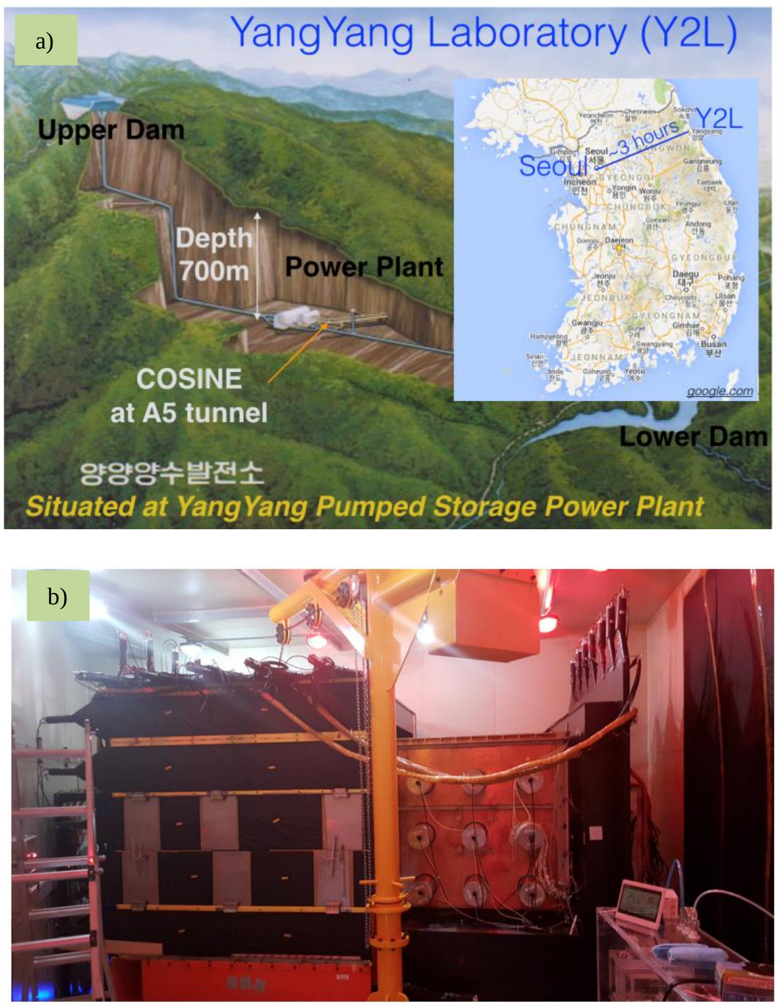

Figure 2.1 a)The experimental site for COSINE-100 experiment b) Picture of the COSINE detector room

2.2 An overview for the COSINE-100 experiment

COSINE-100 use Thallium doped NaI crystal crystals to study the nuclear recoil events to search the WIMP signal. Several tests from the R&D setup give a good experience for detector setup, its assembly in low background environment, installation, and preliminary quality test [71]. Eight NaI (Tl) crystals having non-uniform dimensions and mass-produced by Alpha Spectrea company are coupled with 3” R12669 Hamamastsu PMTs to read its scintillation signal. The WIMP search crystals are submerged into a Linear Alkyl Benzene (LAB)-based liquid scintillator which is used as a passive shielding as well as an active detector to reject the coincidence backgrounds. The dominant background contributions originated by cosmogenic muons and external sources such as decays of radioisotopes in surrounding materials can be excluded by shielding the detector in a deep underground laboratory using heavy shielding design made of lead and copper. The COSINE-100 used a 5 cm copper box and 20 cm lead shielding. Additionally, 37 muon counters are installed outside the lead shielding. The experiment extends its search to study the time dependent behavior of muon induced neutron events and that's why Polyethylene shielding is excluded from the shielding layers. The picture of the COSINE detector when the front door is open is as shown in Figure 2.1 (b). The details of the WIMP search COSINE crystals and its shielding structure are describing into the following subsections.

2.2.1 Shielding structure

Plastic scintillators provide a simple and reliable method for tagging cosmic-ray muons that pass through or near the detector. The main purpose of the Muon detector is to study a correlation between muons and WIMP search crystal signals. Thirty-seven Plastic scintillators are installed at the outermost layer of all six sides in the shielding skeleton. The dimension of each panel is listed as in table 2.1. The plastic scintillator panels are coupled with 2” H-7195 model Hamamastsu PMTs via light guide as shown in the Figure 2.2.

The lead blocks having a dimension of 20 cm × 10 cm × 5 cm with a total mass of 56 tons are stacked outside the copper box as a gamma attenuator. Low background lead blocks having 6.9 ppt of ^{238}U and 3.8 ppt of ^{232}Th are used in the inner half of shield while normal lead having a purity of 99.99 % is used in the outer half of this shielding. A 3 cm thick oxygen-free copper box having a dimension of 152 cm × 142 cm × 142 cm with total mass of 6.4 tons are installed inside the lead castle. An acrylic box 1 cm thick is fit to the inner walls of the copper box which is filled by the liquid scintillator. The copper box in this shielding is used to hold the acrylic box as well as a gamma attenuator.

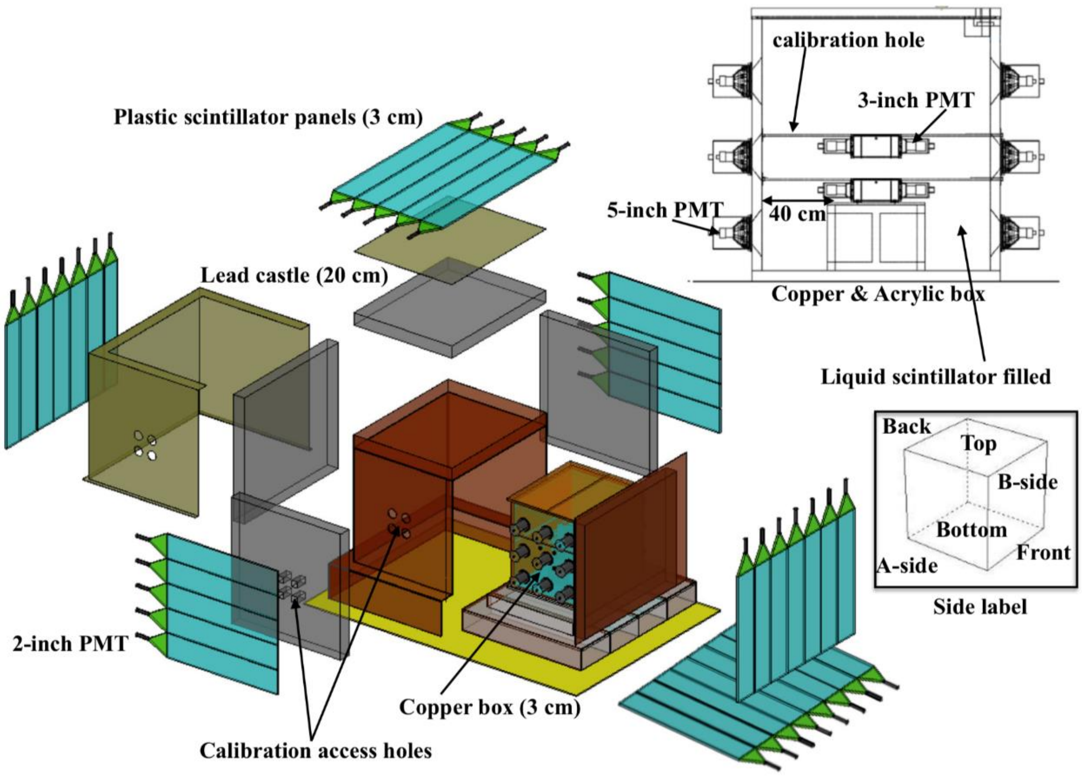

Figure 2.2 Shielding framework of the COSINE experiment

Table 2.1: Dimension of the plastic scintillator muon panels used in the COSINE-100 experiment.

Position	Length (cm)	Width (cm)	Thickness (cm)	Number of Panel	PMTs
Top	282	40	3	5	2
Front	205/207	40/33	3	5/2	1
Back	202	40/33	3	5/2	1
Right	204	40	3	5	1
Left	204	40	3	5	1
Bottom	205/207	40/33	3	2/6	1

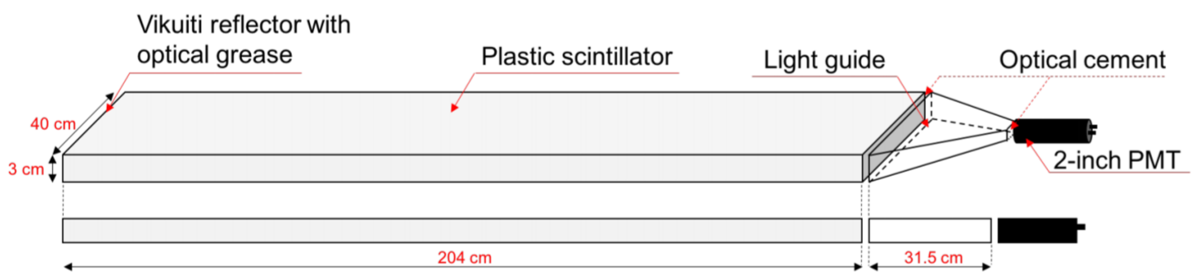

Figure 2.3 Muon detector assembly in COSINE-100 experiment

2.2.2 LS veto system

To reject the background contribution from external materials as well as the materials which are very close to the detector, it is beneficial to have an active veto system that can reduce background level by tagging neutron and gamma events. The level of the internal background can be reduced with an active veto system by tagging escaping gamma-rays from the NaI(Tl) crystal. LAB based liquid scintillator is used as an active veto system first time with NaI(Tl) crystals for dark matter search experiments.

The prototype detector was designed and installed at the R&D set up to determine the feasibility of reducing the background of a NaI(Tl) crystal detector for a dark matter search experiment. The background rate was reduced to 0.76 +/- 0.04 counts/kg/day/keV events at 6 - 20 keV, most of which originated in the external background. The internal ^{40}K rejection is about 48 %, consistent with observed data [73]. A new shield with an appropriate LS thickness will increase this rate to approximately 80%.

The COSINE-100 produced around 3 tons of the LAB based scintillator in its production factory. The emission spectrum of LAB has maximum at 340 nm, so the wavelength shifter was mixed to a solvent to adjust the wavelength of optical photons suitable for Photomultiplier tubes (PMTs) used in COSINE-100 experiment. Widely used PPO (2,5-Diphenyloxazole, $C_{15}H_{11}(NO)_3$g/L as a flour and bis-MSB (1,4-Bis(2-methylstyryl) benzene, $(CH_3C_6H_4CH=CH_2)_2C_6H_4$ 30 mg/L as a wavelength shifter [74] are mixed with the raw LAB which was supplied from Korean domestic company. To prevent any possible insoluble impurities, LAB is filtered by Meissner filters that have 0.1 μm pore size. It is relatively easier to dissolve PPO and bis-MSB, so 20 times enriched master solution is prepared at first and later mixed with raw LAB to make the optimized proportion.

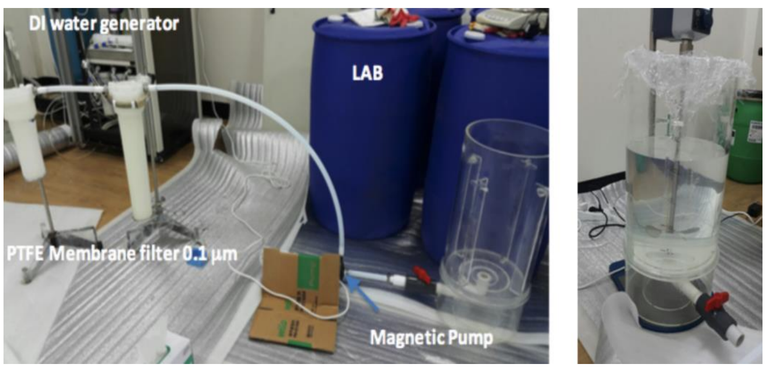

Figure 2.4 COSINE liquid scintillator production factory

It might be possible that the master solution may contain some amount of ^{40}K, which can be purified via water extraction. The master solution is mixed with De-Ionized (DI) water that has more than 17 MOhm resistance with the ratio 1:5 (by volume). The mixture is stirred for one hour and transfer to the clean container after the sedimentation of DI water. Karl-Fischer titration machine is used to check the humidity level of purified LS master solution and filtered LAB for reference. The result of titration shows 170 ppm inside the LS master solution while 60 ppm inside the LAB. So, N_2 gas is purging to reduce the humidity of the LS master solution and the final value was measured as 20 ppm. After enough purging, the LS master solution was mixed with filtered LAB.

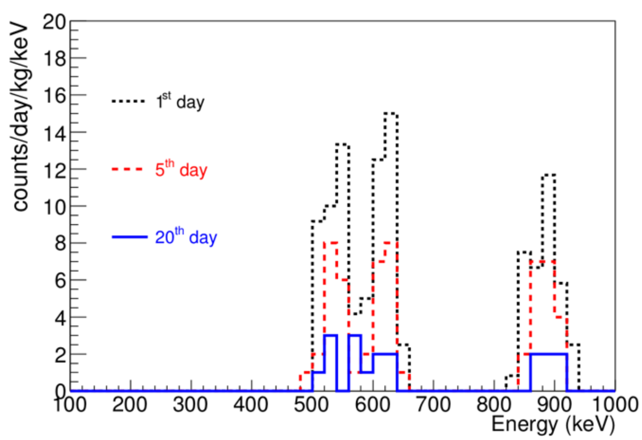

Figure 2.5 Alpha energy distribution from COSINE-LS with prototype detector

A small size LS prototype detector (~70 ml in volume) readout by 3- inch PMTs is constructed and installed at Y2L to understand the radiopurity of the LS. Internal alpha and beta/gamma events are well separated by using the technique described in Section 2.5.1. An available polyethylene shielding is good enough to prevent external neutron background events. The measurement shows 7 ppt and 4 ppt of ^{238}U and ^{232}Th respectively into the liquid scintillator which gives a negligible background to the NaI(Tl) crystal.

2.2.3 Photomultiplier tube

The R12669SEL PMTs which is the modified version of the PMTs used by DAMA (R6233) [75] are used in COSINE-100 experiment to readout the scintillation signals. This is the Super Bialkali (PMT) PMT having quantum efficiency ~35% at emission spectrum of the NaI(Tl) signal around 420 nm as specified in figure 2.6. The radioactivity of the PMT is measured by using HPGe detector at Y2L as listed into table 3.1.

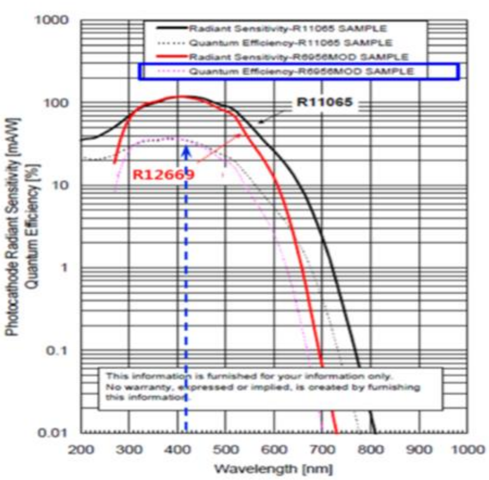

PMT	R12669SEL	R11065SEL
Photocathode	SBA	Bialkali
Window	Borosilicate	Quartz
Body	Borosilicate	Kovar
Stem	Glass	Glass
Gain(HV)	1×106	5×106
U(214Bi)	25±5	60±5
Th(228Ac)	12±5	0.5±0.2
K(40K)	58±5	19±2
226Ra	60±10	5±2
208Tl	4±1	

Figure 2.6: Quantum efficiency of the PMTs B) Specifications for R12669 and R11065. Radioactivity levels measured with a HPGe detector at Y2L. SEL means “selected for high quantum efficiency” [105]

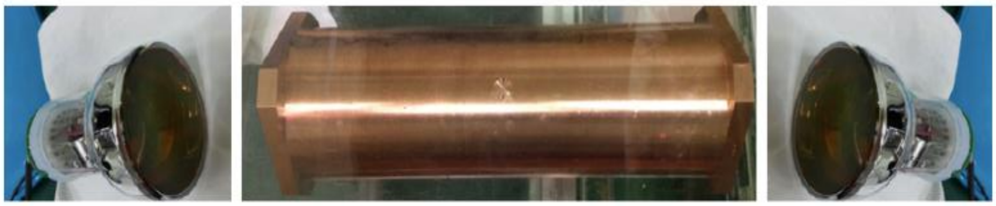

Figure 2.7 The picture of the NaI(Tl) crystal's with PMTs before assembling.

COSINE-100 is collecting data simultaneously using two channels anode (high gain) and dynode (low gain). Dynode readout is used to analyze the high energy events including alpha events which are used to understand the internal background. However, pulses from R12669SEL PMTs are saturated and electron loss at the later stages of dynodes causes non-linear behavior above few MeV as shown in figure 2.8 (a). A test bench is developed with a modified base circuitry with different stages of dynode channel readout. The distorted shape of anode readout is recovered with the 5th stage of dynode readout as shown in figure 2.8(c). The correlation between charge sum and pulse height is deformed via anode readout while recovered up to 10 MeV via the 5th dynode stage as shown in figure 2.8 (d)

The modified dynode channel reproduces the anode channel with a well-maintained energy resolution in one of the NaI(Tl) test detector as shown in figure 2.8 (d). This illustrates that the 5th stage dynode channel resolves the non-linearity problem of R12339SEl PMT and maintains the dynamic range up-to around 10 MeV. This modified PMT base is used to readout the scintillation signal form the WIMP search detector. We used 5” PMTs for liquid scintillator veto detector and 2” PMTs for muon detector.

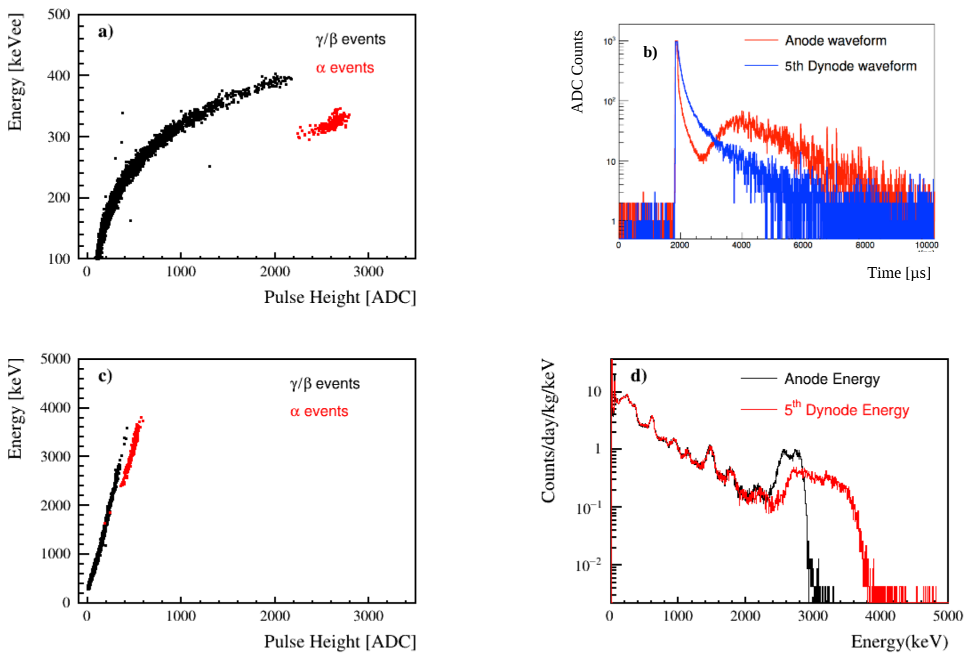

Figure 2.8 a) Correlation between charge sum and pulse height in Anode readout b) Pulse shape of an event readout via anode and 5th stage of dynode simultaneously c) Correlation between charge sum and pulse height in dynode 5th stage readout d) Energy spectrum from anode and dynode readout

2.2.4 NaI(Tl) detector assembly in R&D setup for background understanding

NaI(Tl) crystal in cylindrical shape is grown by different crystal growing company were cut from the large ingots and wrapped with Teflon reflector which is encapsulated with quartz window and copper case. Two 3” Hamamastsu PMTs are assembled to the crystal windows to readout the scintillation signal. The detector assembly is as shown in figure 2.9.

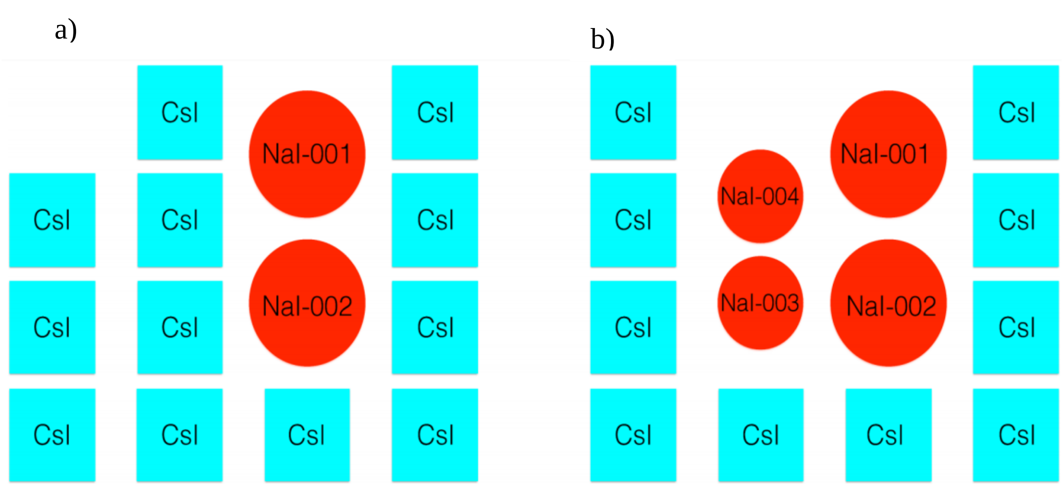

Figure 2.9 Schematic diagram of R&D setups for NaI(Tl) crystals with CsI(Tl) crystal array. NaI-001 and NaI-002 (KIMS-NaI first two crystals) were first tested with configuration A. In the B configuration, other crystals together with NaI-001 and NaI-002 were tested.

More than 15 NaI(Tl) is studied in R&D setup to understand the crystal's optical properties as well as its internal background. Since crystals are installed in an array of the CsI crystals so we can tag 3.2 keV X-rays from the target crystals and 1460 keV gamma from neighbor crystals to calculate the ^{40}K event rate. The background is estimated after considering the tagging efficiency based on the Geant4 MC as describe into the reference [71]. The total alpha rate is calculated by using the pulse shape discrimination technique between alpha and beta/gamma events.

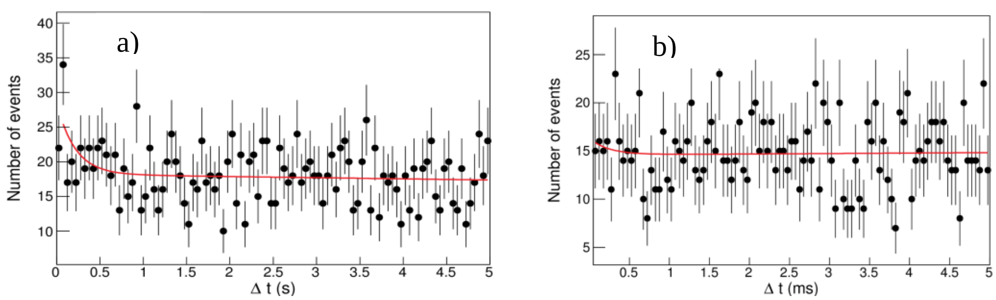

Figure 2.10 a) The time difference distribution between two alpha events from NaI-003 crystal. An exponential component below 1 second is due to the sequential decay of ^{220}Rn and ^{216}Po. b) β-α coincidence time spectrum from NaI-003 crystal. ^{214}Bi decay component was not identified so only upper limit is given from the fit.

The well-known time coincidence method commonly known as the Bi-Po method is used to estimate the ^{238}U level and a similar time coincidence method between two sequential alpha events is used to estimate the ^{232}Th level [56]. The specification of the crystals with its light yield and radiopurity are summarized in tables 2.2 and 2.3.

Table 2.2. Summary table for NaI crystals with their history

ID	Mass (Kg)	Comp.	Material	Prod. Powder	Growth	Day at Y2L
NaI-1	8.26	AS	B	-	2011.9	2013.9
NaI-2	9.15	AS	C	-	2013.4	2014.1
NaI-3	3.3	AS	Astro-grade (K:25.07 ppb)	2014.2	1014.4	2014.8
NaI-4	3.3	AS	Crystal-grade	2013.4	2014.3	2014.8
NaI-5	9.16	AS	As Wimp Scint II	2014.5.29	2014.7.24	2014.12
NaI-6	11.44	BH	Crystal Grade	-	2014.10.8	2015.01
NaI-7	9.16	AS	As Wimp Scint II	2014.5.29	2014.7.24	2015.07 (repacking 2015.05)
NaI-8 (Alu. Encap.)	1.84	BH	Astro-grade	-	2015.9 (Assembly 2015.11)	2015.12
NaI-9	3.29	BH	Crystal grade	-	-	2015.12
NaI-10	1.28	AS	As Wimp Scint II	2015.8.6	2015.10.2 (start 2015.8.17)	2015.12.21
NaI-11	12.5	AS	As Wimp Scint II	2015.8.6	2015.11	2016.02
NaI-15	1.8	SICCAS	Astro-grade	-		2016.12

Table 2.3 Measured radiopurity of the R&D crystals.

ID	U (ppt)	Th (ppt)	K (ppb)	Total alpha (mBq/kg)	Measured by	Light output (NPE/keV(^{241}Am source)
NaI-1	<0.02	<3.17	41.4±2.99	3.29±0.01	KIMS	15.60±1.41
NaI-2	<1.04	<0.48±0.2	49.3±2.43	1.77±0.01	KIMS	15.51±1.41
NaI-3	<0.14	0.46±0.07	25.34±3.57	2.43±0.011	KIMS	13.26±1.28
NaI-4	-	-	116.70±6.78	-	KIMS	3.85±0.38
NaI-5	<0.04	0.19±0.002	40.1±4.2	0.48±0.004		12.14±1.14
NaI-6	<0.05	8.9±0.004	127.12±6.45	1.53±0.01	KIMS	4.36±0.39
NaI-7	<0.04	0.20±0.01	38.11±5.38	0.85±0.04	KIMS	15.23±1.40
NaI-8 (Alu. Encap.)	<0.13	1.15±0.2	<17	21.4±0.7	KIMS	10.77±1.30
NaI-9	<0.14	94±12	639.14±51.24	7.4±0.2	KIMS	6.05±1.11
NaI-10	<0.016	<0.077	17.97±11.72	0.94±0.10	KIMS	20.88±1.33
NaI-11	<0.016	<0.079	18.5±3.2	1.025±0.13		16.8±1.2
NaI-15	<0.04	1.5±1.8	19.06±8.28	0.98±0.07	KIMS	6.06±0.56

It was found a very low level of ^{238}U and ^{232}Th in the studied crystals in comparison with the total alpha rate. It might be possible to have an additional ^{222}Rn contamination that may happen either at powder level or crystal growing and encapsulating period which can be confirmed by measuring the ^{210}Po as a function of the time. If we assume the zero level of

^{210}Po when the power/crystal suffers from ^{222}Rn contamination, then ^{210}Po will be increased and becomes equilibrium. So, modeling the alpha rate as a function of time with the half-life of ^{210}Po would give the possible ^{222}Rn contaminated date as shown in Figure 2.11. The predicted ^{222}Rn contaminated date coincides with the crystal grown period. Because of the high light yield and relatively better radiopurity, COSINE-100 decided to use the crystal grown by Alpha spectra company, Colorado, USA. The similar detector assembly technique of the R&D setup is used to assemble the COSINE crystals.

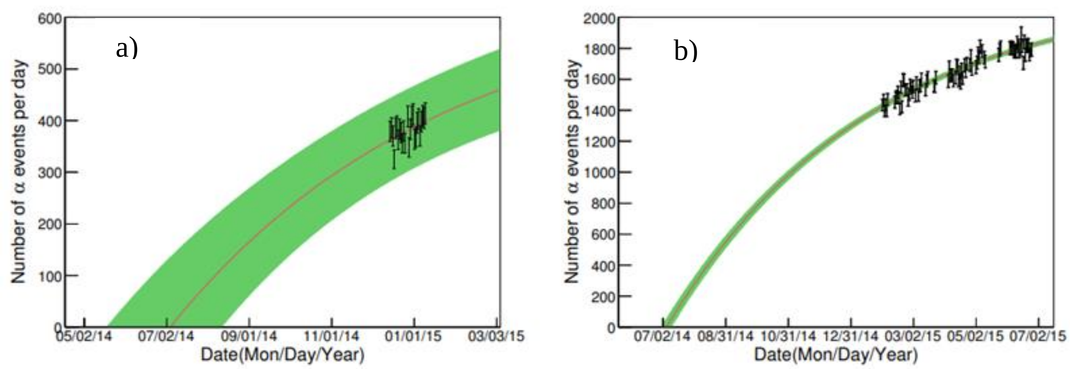

Figure 2.11 The increase in alpha activities is fitted to a model that assumes a single, instantaneous ^{210}Po contamination event occurred for each crystal: a) NaI-005 and b) NaI-006. The red line indicates the best fit model with its 68% uncertainty as a green band. Additional α events from the substantial ^{232}Th contamination in NaI-006 precedes the crystal growth period.

Eight crystals in an array of 4 × 2 which is grown by Alpha spectra company with different grades of power as WIMPScint-II and WIMPScint-III are submerged to ~2 Ton of the liquid scintillator in the COSINE-100 experiment.

2.3 COSINE-100 DAQ system

COSINE-100 used FADC & M64ADC module with the Trigger Clock Board (TCB) developed in collaboration with the domestic Korean company "Notice". 42 and 16 PMTs are used to read the muon LS veto detector signal respectively. This detector is triggered only if the NaI (Tl) detector satisfies the trigger condition so Muon and LS detector is a passive detector while NaI(Tl) is an active detector. Passive detector signals are digitized with 64 MS/s ADC (M64ADC) with 12-bit resolution and 2V of dynamic range. Eighteen PMTs signal of the active detector is digitized with 500 MS/s (FADC) with 12-bit resolution. These active detector signals are collected via 3" PMTs having two simultaneous readouts as discussed in section 2.2.3. The data flow scheme is described more details in ref [76]. The FADC modules trigger such events that make a hit to both PMTs of a crystal over the hardware threshold (6 mV) within the coincidence window of 200 ns. If one of the crystal modules satisfies the above condition, then those events are transferred to the TCB and FADCs digitize the waveform of all the crystals. An example of the triggered signal above with low and high gain is shown in figure 2.12.

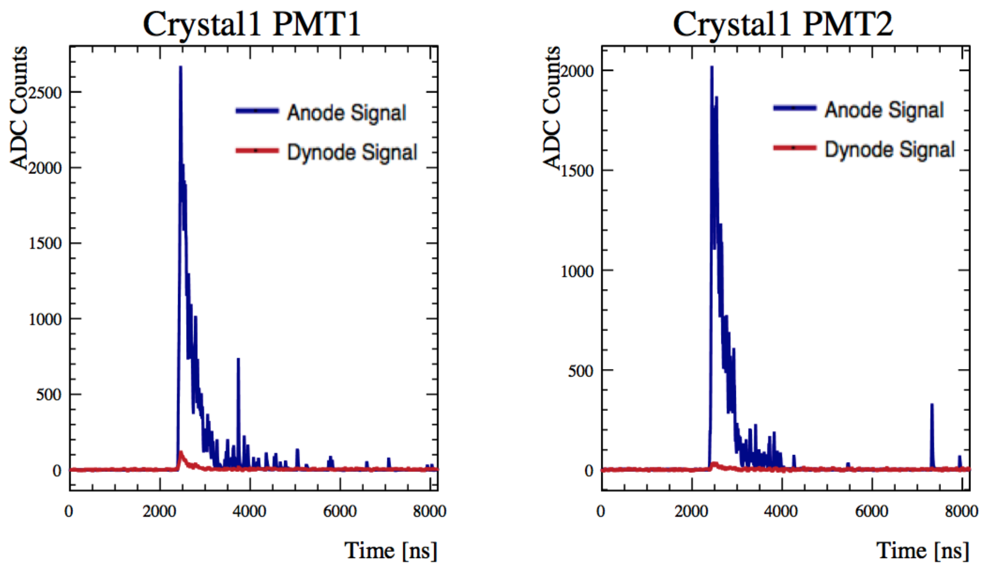

Figure 2.12 Raw signal shape of the triggered events in anode (high gain) channel and dynode (low gain) channel

CAEN A1535N HV module is used to supply the high voltage for PMTs. The HV is adjusted between two PMTs after matching the gain of the PMTs. The high and low gain signal from crystal PMTs are amplified by × 30 and × 100 respectively while LS PMTs signal is amplified by a factor of 30. PMT signals bandwidth is about 100 MHz which requires more than 200 MHz sampling rate, that's why 200 MHz bandwidth OP-Amp was used to amplify the signal.

2.4 Muon detector

The outer detector shielding is consisting of 42 PMTs of 2-inch PMT from Hamamatsu Photonics and 37 plastic scintillators with 3-cm thickness of type EJ-200 having maximum light output wavelength 425 nm. The array forms a near cubic structure with side labeled as front, back, top, bottom, left, and right. The length of the top-side panels are 282 cm and read out by a PMT at both ends. The panels on the other side are approximately 200 cm long and their signals are readout by one PMT.

2.4.1 Muon detector assembly

An acrylic light guide is coupled in each panel using BC-600 optical cement. Two-inch H7195 PMTs from Hamamatsu Photonics are coupled at the end of the light guide to read the scintillation signal. A vikuiti reflector film and TYVEK reflector sheet is attached to the scintillator to increase the light collection efficiency, covered with a 50-μm-thick aluminum foil and a black vynil sheet to prevent external light leaking and physical damage.

2.4.2 Event selection for muon events

The goal is to develop a procedure that will identify muons which passed all of detector components in COSINE-100. The ADC sum refers to energy equivalent of events that digitized from DAQ. A coincidence analysis is pervasive technique and to use for estimating the closest events between at least two panels in coincidence window. This method can determine the region for perspective part of spectrum, which either region for low energy background or high energy of muon. The maximum of Landau distribution defines the most probable value (mpv), where the maximum of the muon distribution is expected. Therefore, muon cut threshold is optimized by selecting the muon candidate events whose charge sum should be greater than 14,000 ADC units. To improve the selection, The time differences (ΔT) between the bottom-side and top-side signals, where muon candidate events exhibit a clear coincidence, while γ/β background events have a random distribution. On the basis of the time correlation observed for the muon candidate events, an additional selection criterion of ΔT is applied containing 5σ range of signal events, in this example -100 ns to 115 ns and the background contamination in the signal region is calculated to be 0.2 %. From the fit, the background contribution in the signal region can be estimated as approximately 0.1 %, which is consistent with the background contamination rate estimated with ΔT distribution. The muon selection efficiency of the charge threshold cuts as mentioned above was estimated to be (99.9 $\pm$ 0.1) %. A similar muon selection technique is applied for all pairs of different sides to tag muon candidate events.

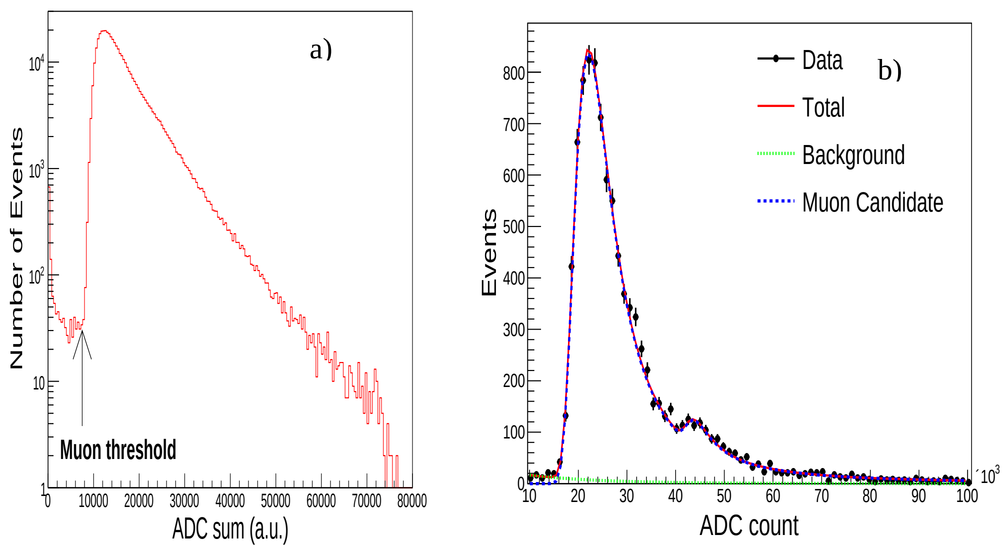

Figure 2.13 (a) All events are selected after applying the threshold and time cut. (b) The fit results shows a negligible number of muon like signal events (<0.1%) can be removed because of the muon threshold selection for top-side charge.

2.4.3 Muon monitoring system

The muon flux at the COSINE-100 experimental side is determined from all of two-side hit events including signals in the top-side panel array. Any muon events that hits in more than 2 sides are accounted as a single muon event. The calculated effective area of the top side is $A_d = 5.48 \pm 0.16$ m^2.

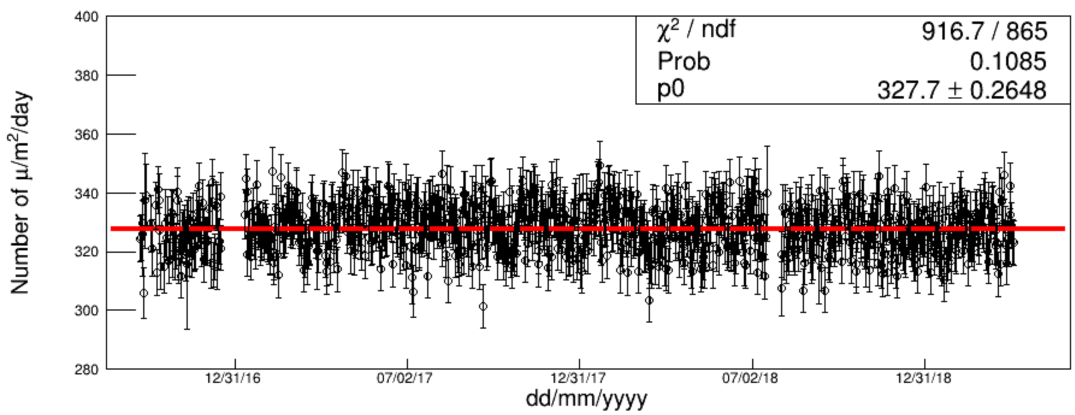

Figure 2.14 The measured muon flux at the COSINE-100 detector over a set2 data.

2.5 Neutron Monitoring detector (NMD)

There have been continuing debates about whether or not the DAMA annual modulation signal is due to muon-induced neutron signals that are known to be seasonally modulated [77]. So, it is important to understand muon-induced neutrons because neutron- induced nuclear recoils can mimic WIMP-nucleon interaction events. The main source of neutron is the spontaneous fission of ^{238}U in the rocks, (alpha, n) reactions caused by alpha particles from the decay of ^{238}U, and ^{232}Th and cosmic ray muons which break the target nuclei. The high energetic muons interacting with the shielding materials may generate neutrons inside the shield. Due to possible modulation of environmental neutrons, that neutron can interact with nuclei, monitoring neutron is necessary for annual modulation study. The COSINE-100 construct a fast neutron monitoring detector and install it at COSINE experimental hall. Details of NMD is discussed below.

2.5.1 R&D for fast NMD

In the case of fast-moving neutrons, the energy conversion process is the elastic scattering with light nuclei, that give rise to recoil nuclei. Two different liquid scintillators are the candidates for the fast neutron detector. One is the LAB-based LS produced by COSINE collaboration as described in section 2.2.2 and the other is Di-isopropylnaphthalene (C16H20, DIN) based LS which is a commercial product called ``Ultima Gold-F (UGF)" produced by PerkinElmer company. In comparison to cocktails based on DIN, the classical cocktails show very short pulse length [78]. This discrimination is much clear if the pulses are stretched. Since UG-F is the commercial LS, so it isn't clear about the type and quantity of wavelength shifter mixed into the DIN solvent.

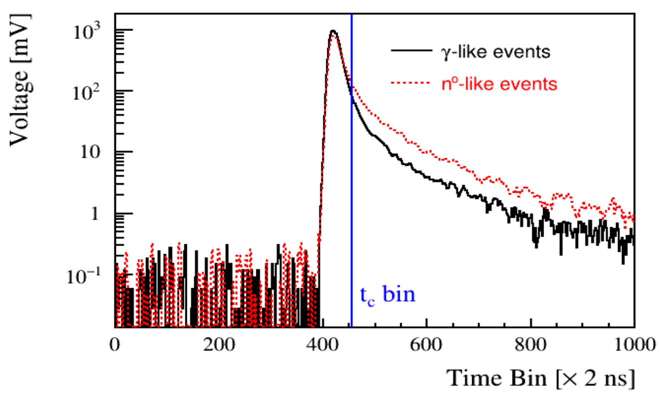

Figure 2.15 Signal shape of neutron and gamma events in UG-F using 252Cf source and optimization of starting time of tail section, t_c.

A prototype detector (70 ml in volume) is read out by 3” PMTs (R12669SEL) mounted on each end of the cylinder. PMTs are calibrated with Compton edge mean value (1122 keV) of the ^{60}Co external gamma source. When particle hit on liquid scintillator, it excites the solvent molecules that cause chemical quenching. The energy of solvent molecules is transferred to the flour molecule, which emits photons and those photons are received by a photomultiplier tube. The light emitted from the vast majority of organic LS consists of two main components; the slow and the fast component. An exponential tail that extends to several hundred nanosecond (ns) and an exponentially decaying components that is commonly in the range of few ns are found in slow and fast component respectively[79]. These components having different relative intensities depend on the specific energy loss $\frac{dE}{dX}$ of the particle passing through the LS. So, the signal shape of a fast neutron from LS is different from gamma events as shown in Figure 2.15. A fast neutron has a longer tail than that of a gamma due to greater de-excitation of different states in the LS [80].

Gamma and neutron event can be distinguished by taking the ratio between the integrated tail charge (Q_{tail}) and the total charge(Q_{total}) of the signal. Starting time bin of Q_{tail} value is optimized to get highest discrimination power between gamma and neutron band using ^{252}Cf, neutron calibration data. The optimized ratio parameter (Q_{tail})/(Q_{total}) is called as PSD parameter which is used for neutron/gamma discrimination. This PSD power is quantitatively expressed in terms of figure of merit (FoM) as

$$FoM = \frac{\Delta m}{\sqrt{s_1^2 + s_2^2}} \qquad 3.2$$

where *Δm* represents the difference between the fit mean value of the gammas & neutrons distributions. The s_1 & s_2 are their respective standard deviations. Therefore, higher FoM indicate better discrimination between events induced by gamma & neutron. The PSD power between two samples are studied by using ^{252}Cf neutron source which emits both gammas and fast neutrons with a mean energy of 2.14 MeV. The FoM of UGF-based LS is measured to be 7.1 at the energy range between 200 to 1000 keVee while the LAB-based LS shows an FoM of 4.01 measured in the same energy range. The PSD parameter as a function of electron equivalent energy is as shown in figure 2.16 (b). PSD threshold between gamma and neutron is ~80keV(with 3.2 FoM) for this small 70 ml R&D detector. So, we expect acceptable FoM and PSD threshold for large size COSINE NMD detector. Based on these PSD measurements, UGF-based LS is the good candidate material for COSINE fast neutron monitoring detector.

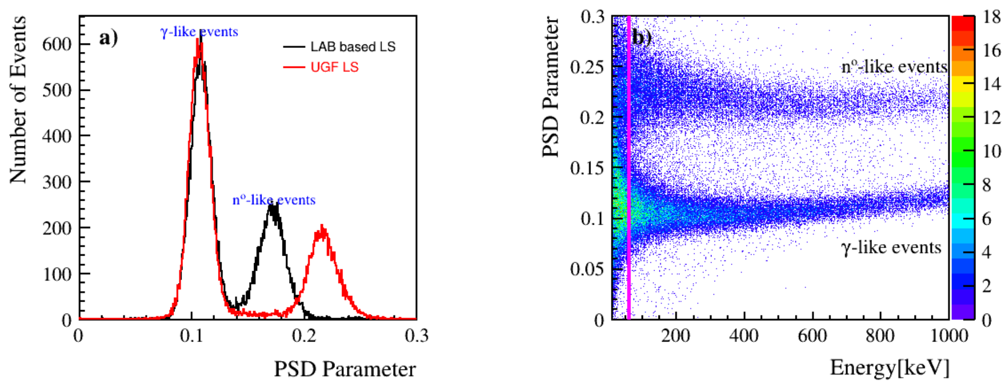

Figure 2.16 PSD study for NMD a)Comparison of PSD parameter distributions of LAB and DIN-based (UG-F) LS at the energy range (200~1000) keVee b) scatter plot between PSD parameter and energy in case of the UG-F. The vertical straight line near to 70 keV shows the PSD threshold

The ^{238}U and ^{232}Th isotopes will decay according their own decay chain and emits alpha (or beta) particles. Relative amount of light from heavily ionizing particles like alpha is larger than that of relativistic beta/ gamma particles. Therefore, PSD parameter is effective to separate β and α events. The signal from alpha is similar to nuclear recoil signal of neutrons from the neuron detector. That is why it is crucial to understand the alpha background in neutron measurement. To understand the internal alpha background, detector filled with UGF having mass 0.6 kg is installed inside the KIMS-CsI shielding test facility at the Y2L that has 10 cm of polyethylene shielding for cosmic neutrons [81].

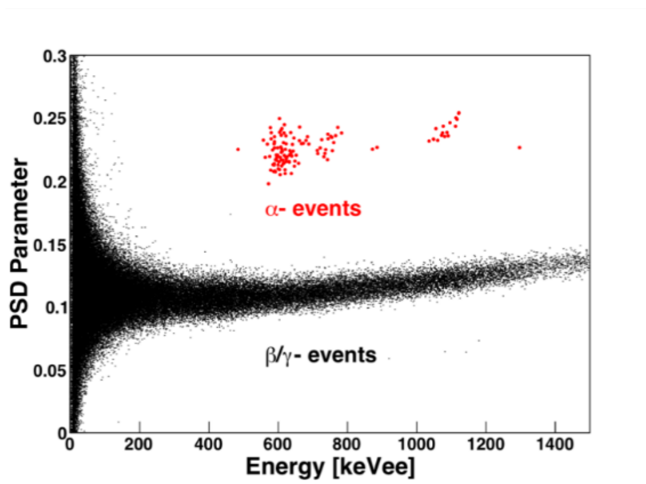

Figure 2.17 PSD parameter vs electron equivalent energy for background data. The upper red islands corresponds to the alpha background.

As shown in figure 2.18, there are three or more components in alpha band. Time coincidence analysis between the isotopes of ^{238}U and ^{232}Th are performed as discussed in section 2.2.

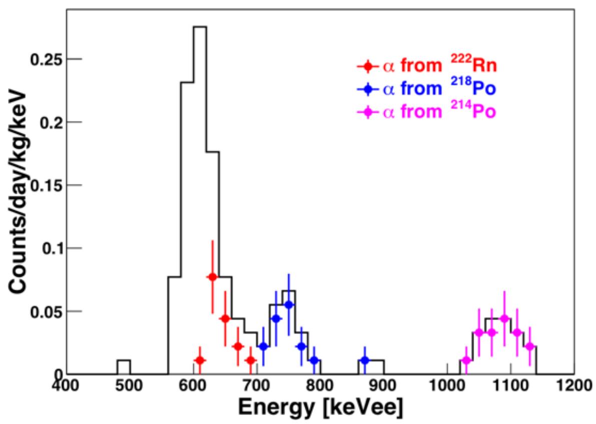

Figure 2.18 Energy distribution of alpha events. The red and blue dots are ^{222}Rn and ^{218}Po, and the magenta shows the distribution of ^{214}Po

The alpha energy distribution cannot be fully explained by the alpha sources identified by timing analysis. Since the alpha source which has alpha energy slightly less than 5.59 MeV of ^{222}Rn should be added, a decay chain and an α-decay are simulated. The first one is the decay chain beginning with ^{226}Ra that emits 4.87 MeV alpha and ^{226}Ra, and the other is ^{210}Po decay which emits 5.41 MeV alpha. As shown in figure 2.19, the remaining component can be assumed to be ^{210}Po, and there are not alpha events from ^{226}Ra. It means the possibility of contamination of UG-F by ^{222}Rn, so we take data for 13 days considering the half-life of ^{222}Rn. However, there is no significant decreasing the activity of total alpha, so the LS contamination is estimated that it is due to almost ^{210}Po. The activities of all components are presented in the next section including comparison with those of purified samples. Meanwhile, there is ^{220}Rn alpha to ^{216}Po alpha coincidence with a half-life of ~145 ms in ^{232}Th decay chain. However, the number of events after applying selection criteria is too small to fit, so we calculated conservatively and got the upper limit of 0.01 mBq/kg.

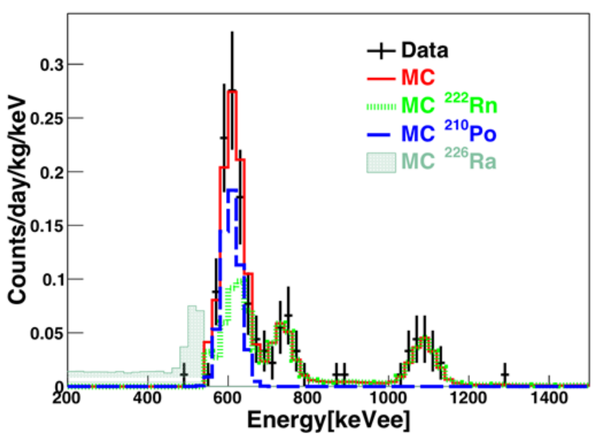

Figure 2.19 Energy distributions of measured (black) and simulated (red) alpha events. The red line includes the decay chain of ^{226}Ra and alpha events from ^{210}Po (blue line). The magenta area indicates only alpha events from ^{226}Ra

A combination of alumina adsorption and water extraction are studied for UG-F liquid scintillator. The adhesion of impurities from liquid to a solid surface is the basic principle of adsorption. Aluminum oxide which is one of the adsorbents is effective method to remove impurities for metal and ion, and successfully used for scintillator purification [82]. Alumina powder having 45 μm size and the UG-F are mixed and UG-F is separated by vacuum filtration using PTFE membrane filter with 0.25 μm pore size. The purified sample is treated by water extraction and nitrogen purging before the measurement. When two immiscible solvents like water and LS are brought into close phase contact, impurities present into the LS which is more soluble into the water can be transferred to water from the LS. So that we can get purified LS after re-separating. For the process of water extraction, the LS and the ultra-pure DI water having 16.4 MWOhm resistance are mixed into the container at a ratio of 4:1, respectively.

The LS and water layers are separated by using separation funnel. After water extraction, LS is purged by the nitrogen to remove radon contamination during the purification process.

Table 2.4. The α-background components with the UG-F before (ND-1) and after (ND-2) purification. All units are mBq/kg.

Sample	^{222}Rn	^{218}Po	^{214}Po	^{210}Po	Total α
ND-1	0.030±0.007	0.030±0.007	0.041±0.008	0.25±0.02	0.036±0.04
ND-2	0.025±0.003	0.032±0.004	0.032±0.004	0.12±0.007	0.21±0.03

Since the LS contamination is considered to be mostly due to ^{210}Po and reduction is expected after purification. We analyze the alpha events of sample after purification and the activities are summarized in table 2.4. In the table, ND-1 and ND-2 are UG-F samples before and after purification, respectively. As expected, the activity of ^{210}Po is reduced by more than two-fold, and other components did not show any significant difference compared to their error. Figure 2.20 shows the energy distributions of alpha events before and after purification.

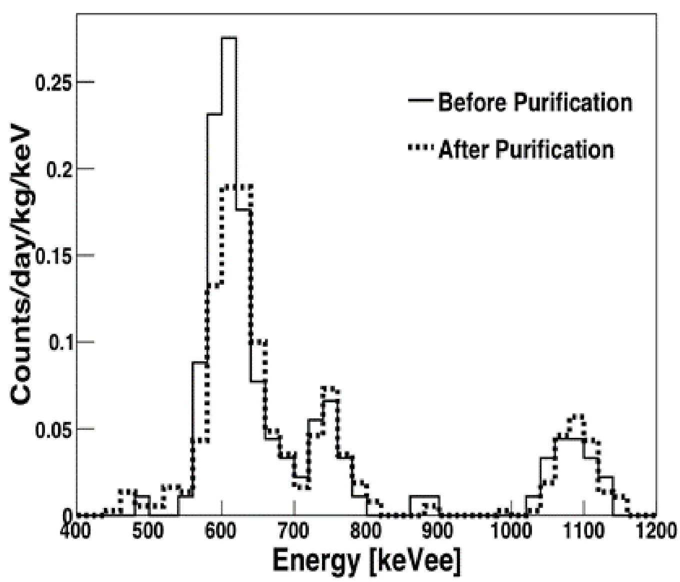

Figure 2.20 Comparison of the internal alpha energy distribution before and after purification

2.5.2 Fast Neutron Monitoring Detector

A cylindrical homogeneous detector made of Teflon having a fiducial volume of 5.2 liters is constructed to measure the fast neutrons inside the COSINE experiment hall. Homogeneous geometry is chosen to optimize the detection efficiencies which led to obtaining better resolution. The Teflon cell itself is a good reflector so it works as a reflector as well as LS container. Two acrylic windows having 1cm thickness are used at each end in which 5" Hamamastsu PMTs are coupled to read the scintillation signal. The best understanding from R&D experience as discussed in the section 2.5.1 is used to handle the detector component and maintain the purity of the target UG-F. The picture of the assembled detector is as shown in figure 2.21. Initial performance and background of the detector are studied at the R&D setup before installing it to the COSINE detector room.

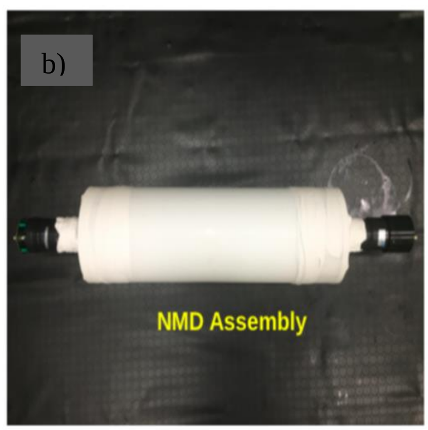

Figure 2.21 Fast neutron detector assembly inside a nitrogen supplied glove box

Since it has larger mass with less optical coverage than R&D detector so higher PSD threshold between neutron and gamma separation is expected. The detector is calibrated with ^{60}Co gamma source and optimization of the PSD power and background is measured with an analysis technique developed in the R&D setup. The PSD threshold is set to be 300 keV with the dynamic range up to 8 MeV and the total alpha background is measured to be 0.17 ± 0.005 mBq/kg. The total alpha rate is stable over two weeks' measurement which illustrates the stability of the detector in terms of the ^{222}Rn leakage. The dominant alpha background is found to be ^{210}Po isotopes as shown in figure 2.22(b). The position dependence is observed so that each event is reconstructed based on the asymmetry distribution of the alpha events.

The neutron detector is installed inside the COSINE-100 detector room within a 5 cm of lead shielding and running smoothly from August 2018. The picture of the detector along with its PSD parameter from the COSINE experiment hall is as shown in figure 2.22(a). The Compton edge from 1460 keV is used to monitor the gain stability of the detector and found to be stable within less than 1% level of the fluctuation for the first six months after installation. The alpha plus neutron band is well separated above 300 keV and alpha background is subtracted to estimate the neutron rate. The neutron plus alpha band below 0.9 MeV is dominated by alpha events and those alpha events are removed with the time coincidence analysis. The neutron rate above 0.9 MeV is found to be 0.016 ± 0.0004 mBq/kg. The alpha events originated from ^{210}Po can't be separated from neutron events and the total rate that includes both ^{210}Po alpha and neutron is found to be 0.088 ± 0.0010 mBq/kg.

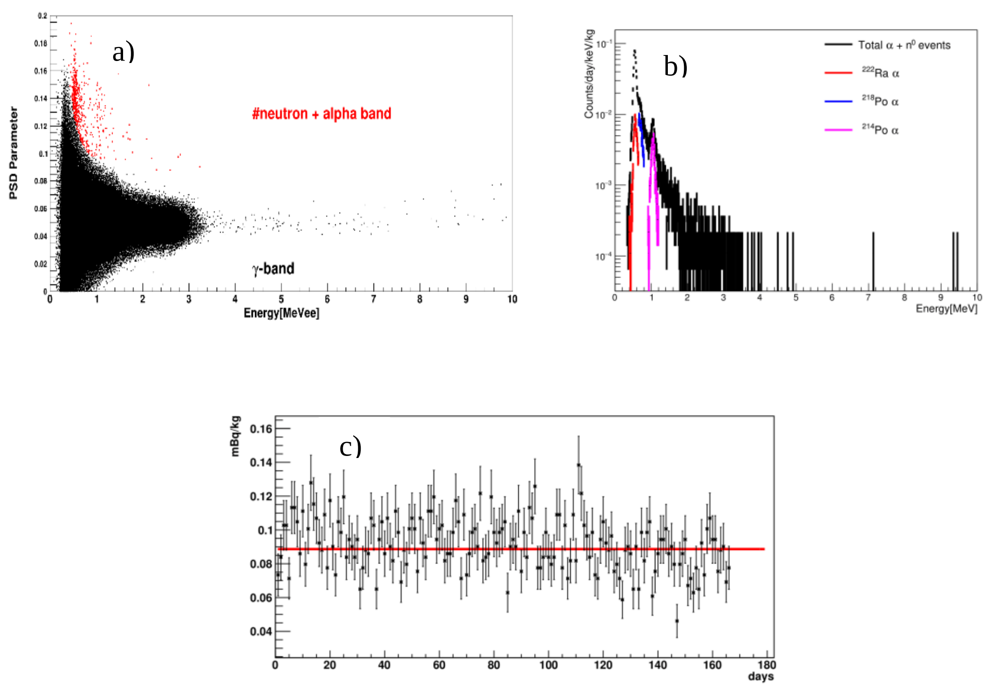

Figure 2.22 a) PSD performance of the NMD that are installed inside the COSINE detector room b) Energy spectrum of the neutron band events with alpha c) Fast neutron rate over the time for first six measurements

2.6 Monitoring system

Publish-subscribe messaging based program is used to monitor and control the COSINE laboratory data. A publisher program collects metrics from sensors and then publishes the metrics to one or more subscribers. A subscriber program subscribes messages from one or more publishers and then store into database or analyze metrics. RabbitMQ server which is a message broker connects with every monitored program at underground station send their message from underground server to the ground station server using federation plugin. Metrics data are stored into InfluxDB [83] servers which provides the visualization service using Grafana [84]. In the Grafana page, we can set an alert which is relayed to Slack application. The smartphone with the Slack app sends an alert to the subscribers. The details about the monitored variables are discuss in the following section.

2.6.1 Environmental variables monitoring system

The environmental variables are important for systematics analysis in seasonal variation. Several environmental variables like temperature, humidity, high voltage, current and so on are monitoring at different locations. Eight temperature sensors from Pico technology are installed at different locations that are very closer to the WIMP search detector, room, and tunnel for temperature monitoring. The temperature data with a timestamp are sent to the monitoring computer via USB. We use three MM2001 analog sensors, manufactured by Maxdetect, to measure the relative humidity. The humidity sensors are connected to the slow monitoring server via a Labjack U3 DAQ module. RAD7 from Durridge Company is installed to the detector room for regular monitoring of the Radon level in the detector. Other environmental variables like oxygen level, dust level, the performance of the air conditioner are also monitored by the system. The stability of electronics such as electricity, a variation of high voltage, current for PMTs is regularly monitored. The temperature in the detector room is well controlled to within a 1 °C variation, while the detector (LS) temperature only varies by 0.1 °C. HVs do not vary by more than ~ 1V from their set value. The Radon level is stable at around ~30Bq/m3. The overall environmental conditions in the detector room are well controlled and very stable.

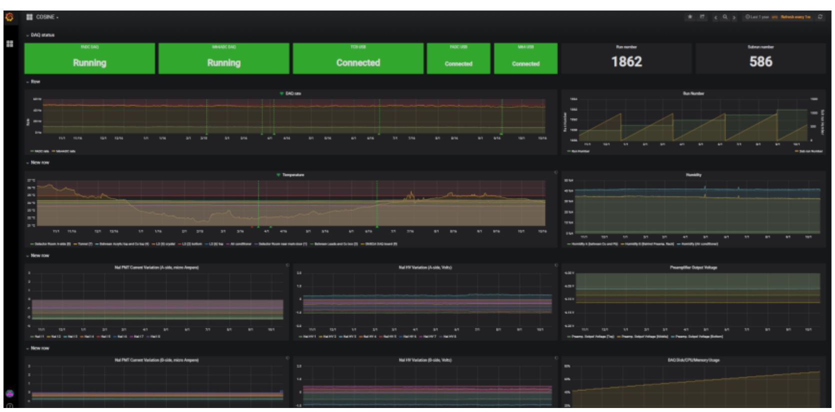

Figure 2.23 Screenshot of the environmental monitoring system

2.6.2 Data monitoring system

The triggered events are saved into the ROOT [cite] data format in every two hours' timestamp and processed immediately by offline analysis framework after preliminary noise selection. Online based data monitoring system is developed to screen the quality of each two hours run. Altogether 41 physics variables are overlaid with reference data that is prepared after using the event selection as shown in figure 2.23. This is the comparison between one example variable (energy) in our monitoring system where blue data points are from two hours run after noise selection and red reference spectrum are ~50 days data after the noise selection. Different time bin like daily, weekly and monthly plots are generated to monitor the time dependency of the variables. Database good/bad run list is updated after monitoring each variables with its chi-square value.

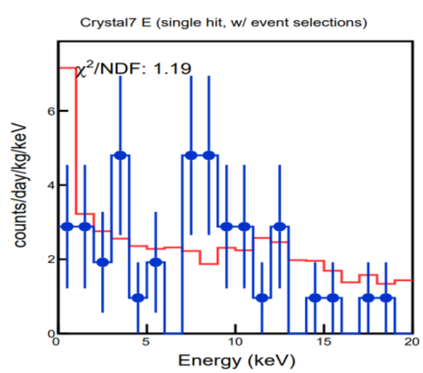

Figure 2.24 An example of the monitored variable (energy) to scan the primary data quality for WIMP search

Chapter 3

Annual modulation search with first 1.7 years of data

The physics run of the COSINE-100 is started from September 30, 2016 and currently running. First, 1.7 years of data called as 'set2 data' in later of this dissertation is used for model-independent annual modulation study. This section discusses about the detector stability, event selection and annual modulation analysis for set2 data.

3.1. Detector stability

The good run data-taking began on Oct 21st, 2016 and continues till the date. This dissertation covers the set2 results which are collected between Oct 21st 2016 to July 18th, 2018. Data is marked with the conservative numbering unit staring from 1544 and each run is marked with individual sub run (having ~2 hours of the live time). The total runs used in this analysis, with a real timestamp and live time are summarized in Table 3.1. Figure 3.1 shows the stability of the detector performance with 93.1 % of the good run data which can be used for physics analysis. The 6.9% loss of data is because of the DAQ failure and calibration campaign.

Table 3.1: The real timestamp information of each runs with their total live time

Run	Sub runs	Start (mm/dd/yy)	End (mm/dd/yy)	Livetime (days)
1544	580	10/20/16	12/09/16	46.42
1546	136	12/09/16	12/19/16	11.22
1616	673	01/12/17	03/09/17	55.22
1617	235	03/09/17	03/28/17	19.40
1625	10	03/30/17	03/31/17	0.72
1626	28	03/31/17	04/02/17	2.17
1627	27	04/03/17	04/05/17	2.13
1634	104	04/05/17	04/14/17	8.61
1652	804	04/14/17	06/20/17	66.87
1654	221	06/20/17	07/09/17	18.28
1666	299	07/09/17	08/03/17	24.84
1671	303	08/03/17	08/28/17	25.20
1672	956	08/29/17	11/16/17	79.67
1678	715	11/17/17	01/15/18	59.43
1683	79	01/16/18	01/23/18	6.50
1690	73	01/23/18	01/29/18	6.00
1718	935	01/29/18	04/17/18	77.85
1719	994	04/18/18	07/10/18	82.80
1720	98	07/10/18	07/18/18	8.08

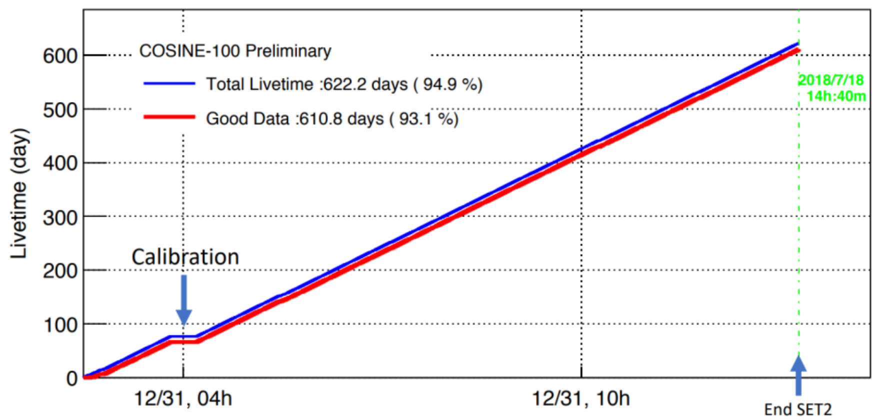

Figure 3.1 Accumulated data from early run to July 07, 2018. This dataset is used for physics analysis in this dissertation.

The amplitude of the DAMA annual modulation between 2 - 6 keV is 0.0095±0.0008 [51]. The long-term stability of the detector is crucial, as instability could manifest itself as a modulation, causing a false positive in our dark matter search.

3.1.1 Environmental stability

The instability in environmental conditions can create a fake time dependenct dark matter signal. So, environmental variables that are seasonally modulated like temperature, radon, and humidity are closely monitored by the COSINE monitoring system discussed in section 2.6.1. The temperature, humidity and radon levels in the experimental hall is maintained to be 23.5±0.3°C, 40.0±3% RH (relative humidity), and 36±10 Bq/m^3 respectively. The temperature and humidity at the proximity of the WIMP search detector are stable within 24.2±0.1°C and < 5% Relative Humidity (RH) respectively as shown in figure 3.2. The muon events are accumulated via muon detector studied over the period as discussed in section 2.4. The RH sensor near the crystal is operated during an interval of 450 days.

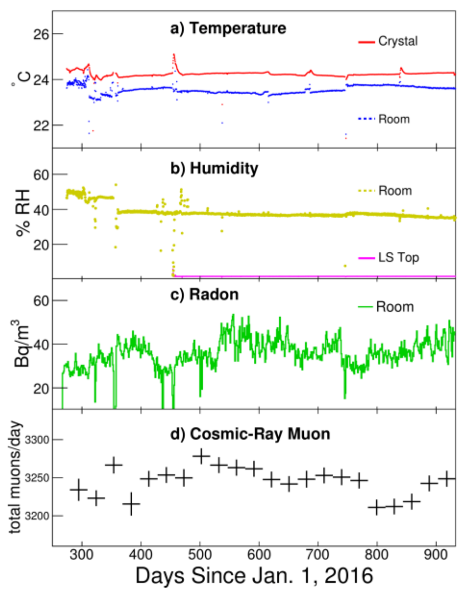

Figure 3.2 Stability of the COSINE-100's environmental variables over set-2 data a) Temperature b) Relative Humidity c) Radon d) Muon rate.

The first zero bin of the x-axis equivalent to the 1st January 2016 and using same axis for all time series plot in later analysis. Air conditioner malfunctioning or power outage causes the spikes in the temperature monitoring plot in figure 3.2. The data during this period is excluded from the physics analysis good run list. In general, environmental stability is well maintained and monitored regularly near the COSINE detector.

3.1.2 Gain Monitoring

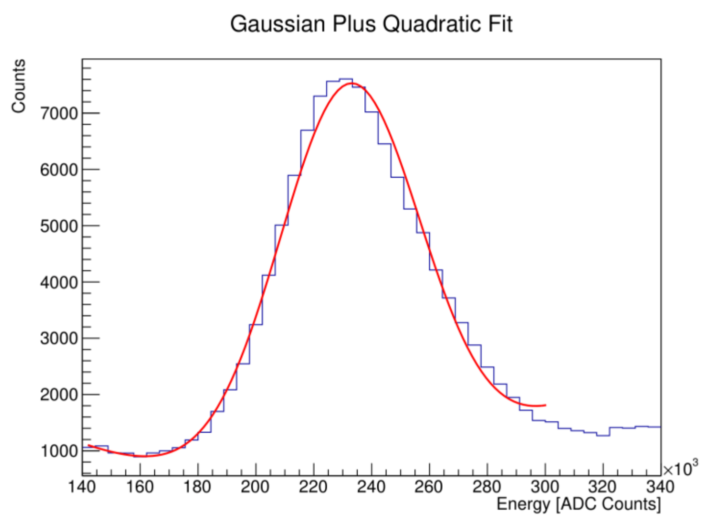

Figure 3.3 Gaussian + quadratic fit for ^{210}Pb peak to track the PMT gain.

The gain of the COSINE data is tracked by measuring the position of the 49 keV peak from ^{210}Pb in the bulk of the NaI(Tl) crystals over the time. Since half-life of ^{210}Pb is 22.2 years, it is long enough that the decreasing abundance of ^{210}Pb will not play a role in the gain monitoring. The WIMP search data is divided into each 0.83 days' bunches and fit with gaussian plus quadratic that returns the best fit value. Figure 3.3 shows the fit for (Gaussian + quadratic) ^{210}Pb peak to track the PMT gain.

The gain behavior over time for each PMT can be seen in figure 3.4. The boundaries within the piecewise function occur at the beginning of run 1616 and the beginning of the run 1678. The boundaries were chosen at "kinks," points where the slope of peak position over time changes abruptly. The source of these kinks is currently unknown, though they do seem to appear at the same point in all PMTs and at times that the detector high voltage is powered down. To correct for the changing gain is modelled as a piecewise linear function over time, as seen in figure 3.4. We introduce two additional boundaries in the piecewise linear function, at the beginning of run 1652 and the beginning of run 1666. Once this function has been fit to each PMT, the observed linear behavior is divided out. This leaves the data at a constant, but arbitrary, ADC value over time. The gain after correction can be found in figure 3.4. We found that that the gain of the PMTs were stable with less than 0.5 % fluctuation over 1.7 years.

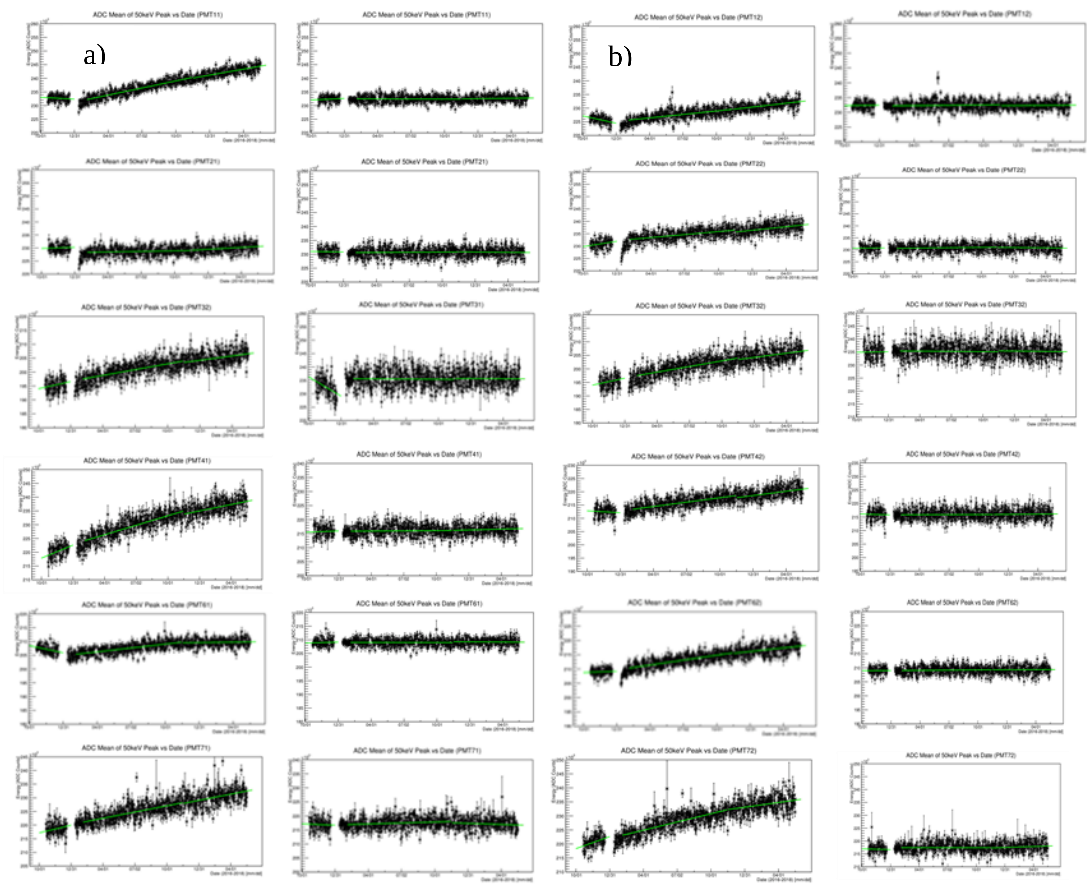

Figure 3.4 Variation of the PMTs gain over time a) left two panels are before correction b) right two panels are after correction

3.1.3 Detector calibration

The detector is calibrated by using external gamma calibration as well as internal gamma peak which is verified by the simulation. 49 keV gamma from internal ^{210}Pb and 3.2 keV x-ray from ^{40}K and available cosmogenic peaks are used to calibrate the low energy channel. The gaussian plus quadratic function was found to have the best goodness of fit with a higher rate of convergence to model the ^{210}Pb decay peak as shown in figure 3.5(a). The energy resolution is calculated by using the ADC values with the function,

$$\frac{\sigma}{E} = \frac{a}{\sqrt{E}} + b \qquad (3.1)$$

where a and b are the constant.

The ^{241}Am calibration data is used to estimate the light yield of the detector that is cross-checked with the 49 keV gamma peak and results are consistents. Out of total eight crystals, light yield from Crystal 5 and Crystal are is obtained to be (3.5 ± 0.33) PEs/keV and (7.33 ± 0.70) PEs/keV respectively, while other crystals are close to 15 PEs/keV. So, Crystal 5 and Crystal 8 are removed from further analysis because of the low light output. The used crystals having high light yield so we achieve the energy resolution (18 ± 1.2)% at 3.2 keV as shown in figure 3.5(c).

The known internal radio-isotopes and its corresponding energy reproduced from the simulation is used to calibrate the high energy of the detector with dynode readout. ^{210}Pb (49 keV), ^{212}Pb (238 keV), ^{214}Pb (295 keV), ^{214}Pb (352 keV), ^{214}Bi (609 keV), ^{60}Co (1173 keV), ^{40}K (1462 keV), ^{214}Bi (1764 keV), ^{214}Bi (2204 keV) and ^{208}Tl (2614 keV) are used as shown in figure 3.6. In general, the COSINE detector has ~10 % resolution at 49 keV and

~2% at 2614 keV via dynode readout. This dynode channel having lower resolution with compared with anode channel due to low PMT gain. Finally, the parameter from the linear function over the best fit values of each peak position is used to translate ADC values to energy scale.

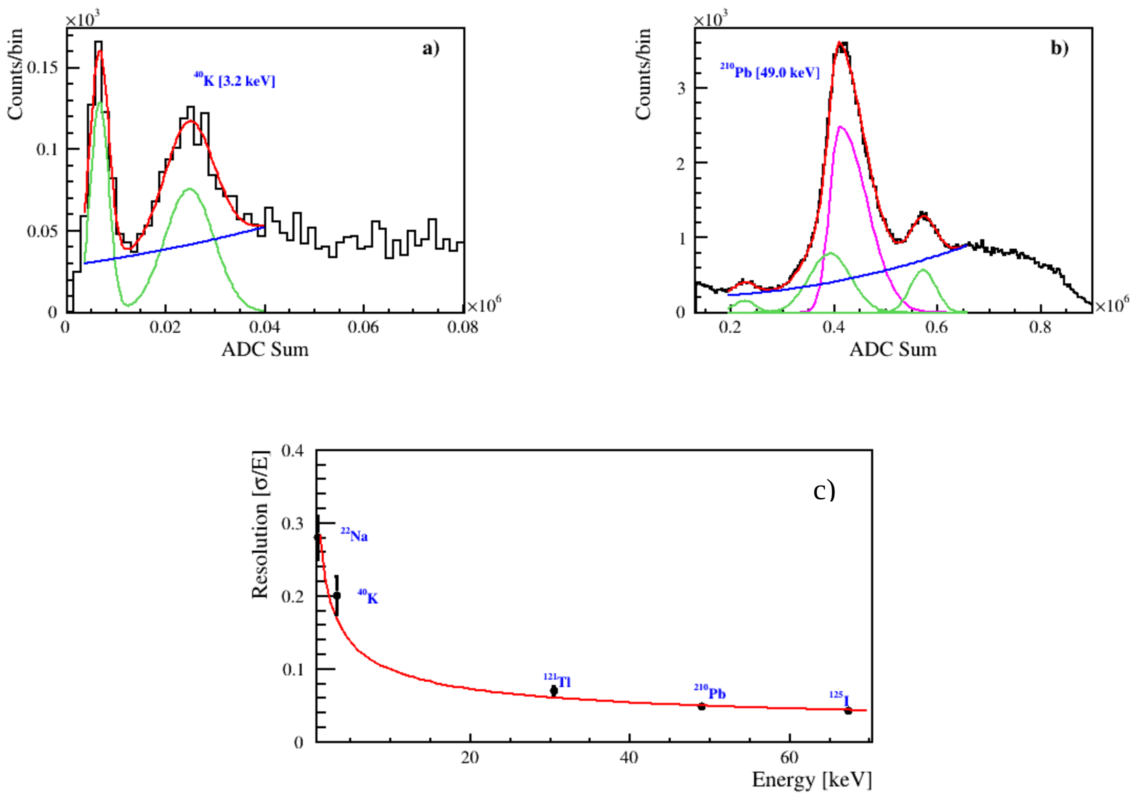

Figure 3.5 The peaks (a & b) induced by different internal radioisotopes in low energy are modelled to get the mean value and (c) measured resolution with high gain (anode)

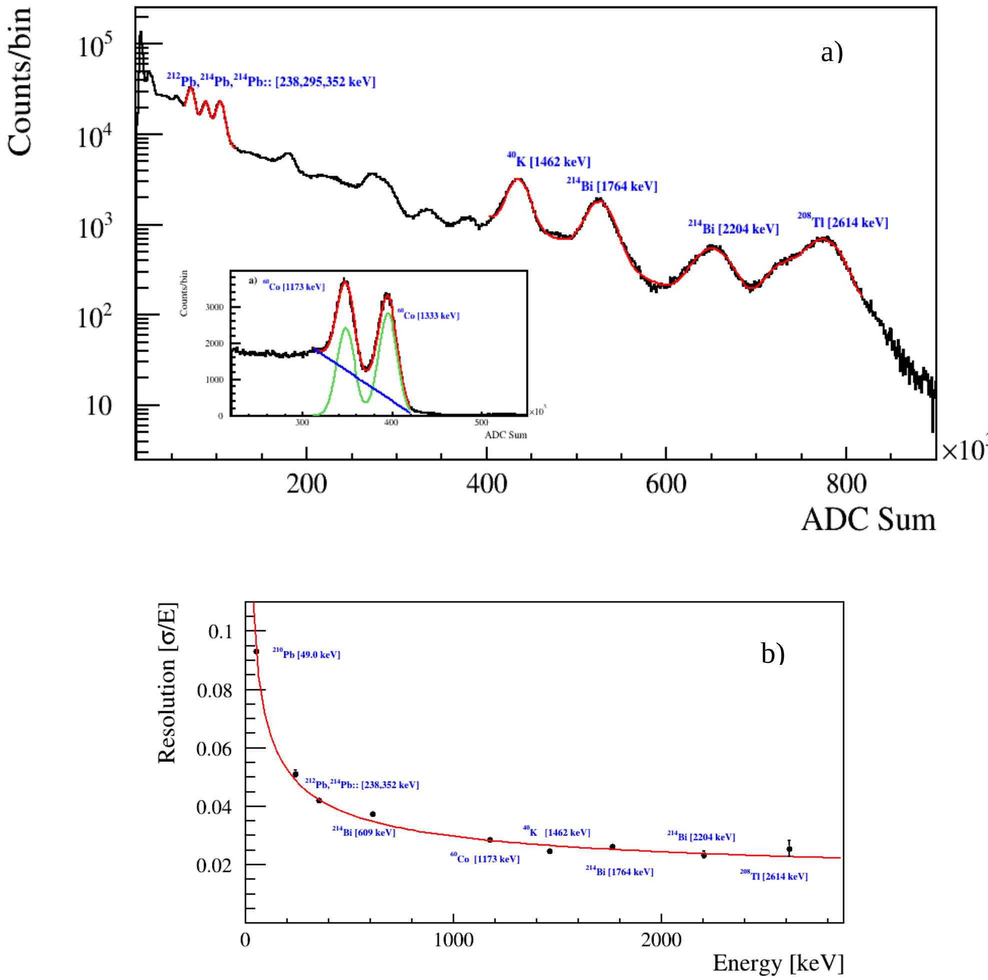

Figure 3.6 The peak (a) induced by different internal radioisotopes in high energy are modelled to get the mean value and estimate the resolution (b)measured resolution with low gain (dynode)

3.1.4 Validation of the gain correction

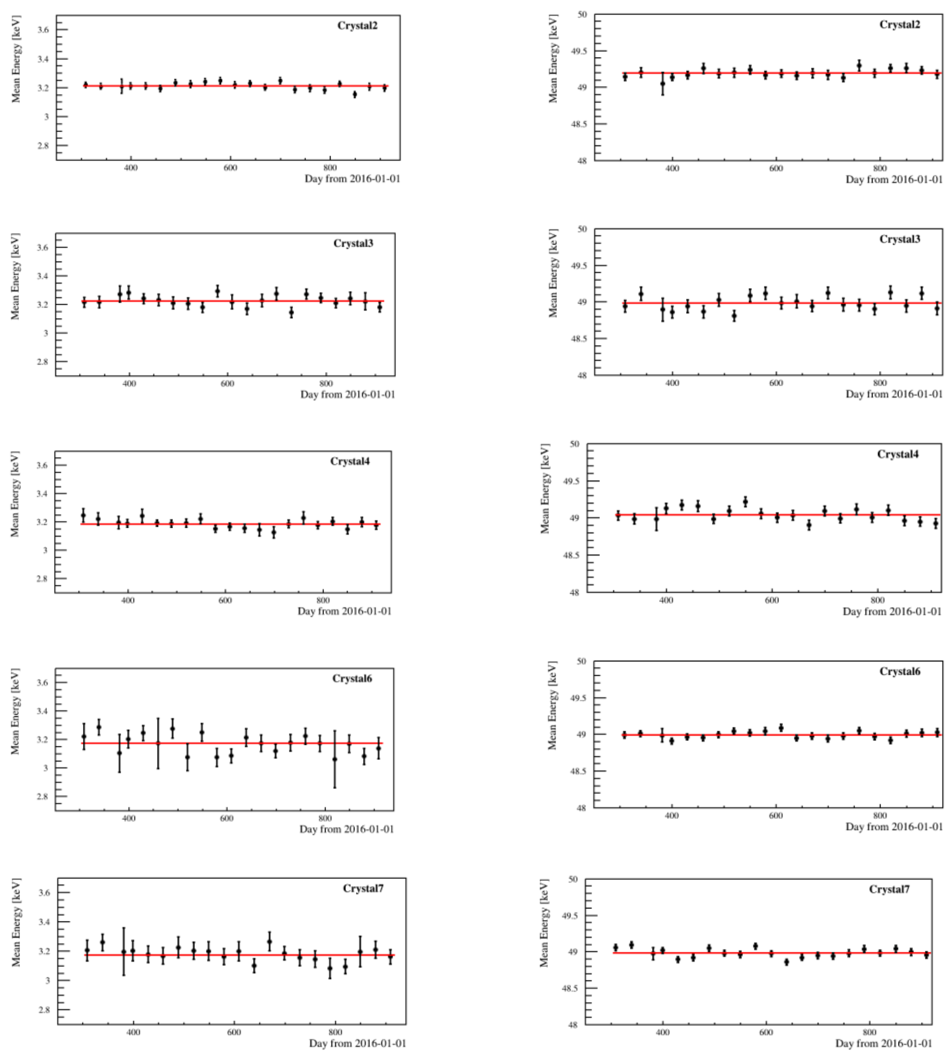

Figure 3.7 Stability of the gain correction and energy calibration in set2 data. Left(Right) panels track the ^{40}K(^{210}Pb) peak position.

To validate the gain correction, we measure the stability of the 3.2 keV x-ray emitted by ^{40}K. This decay is particularly useful, as it allows us to study the gain stability within our 2-6 keV region of interest. The behavior of the peak positions over time for each crystal with 30 days bins can be seen in figure 3.7. Based on this analysis, we find the gain in the 2 - 6 keV region to be acceptably stable with fluctuation of less than 1% level. The sideband region by using 49 keV from ^{210}Pb is also monitored as shown in figure 3.7 and found to be stable.

3.2 Liquid scintillator veto study

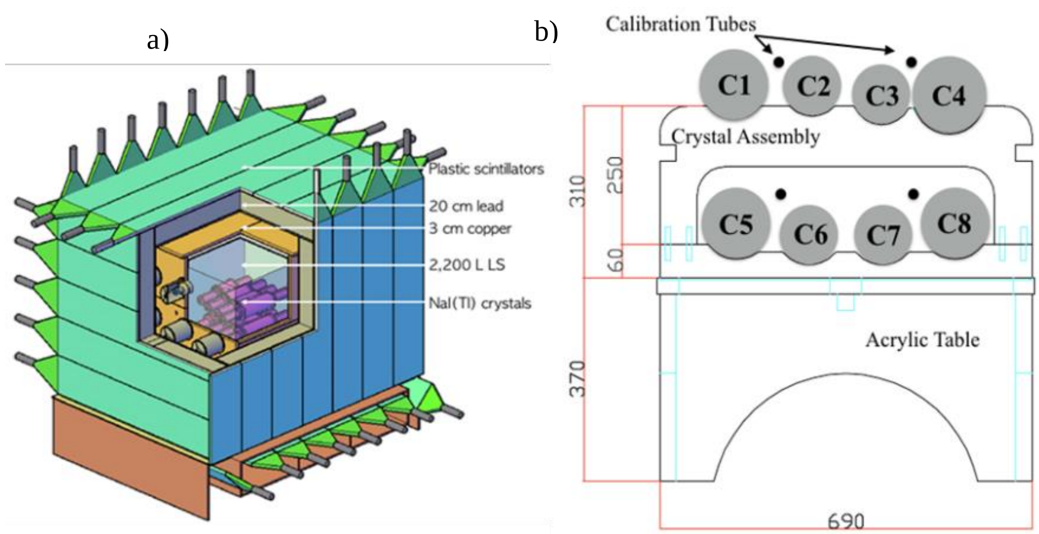

Figure 3.8 a) A schematic of the COSINE-100 detector system. b) A diagram of the crystal arrangement.

COSINE 100 used around 2 tons of LAB based LS which is filled into an acrylic box. The inner walls of the acrylic container and the outer surfaces of the crystal assemblies are wrapped with Vikuiti-ESR specular reflective films to increase the LS light collection efficiency. The photons produced from the LS are read out by 5-inch R877 PMTs from Hamamatsu, attached to the two sides of the box. The minimum distances between the PMTs attached to the crystals and the acrylic box inner wall is approximately 40 cm. A schematic representation of the COSINE-100 detector and shielding structure with the liquid scintillator are as shown in figure 3.8. N_2 gas is purging regularly with ~3 liters per minute to control the humidity and to prevent contact with oxygen. The humidity at this space is kept at <2.0% and high heat capacity of LS helps to keep the temperature within the liquid stable at temperature 24.20 $\pm$0.1 °C.

3.2.1 Gain correction for LS

The LS gain is monitored by tracking a Compton edge of ^{40}K over time. To evaluate the LS gain, we fit the Compton edge of ^{40}K found in the LS spectrum with the following function

$$f(q) = \frac{p_0}{\exp[p_1(q-p_2]+1} \qquad (3.2)$$

and extract the p_1 parameter which represents a location of the Compton edge. The value of p_1 over a time is shown in Figure 3.9(a).

It was observed that the gain slowly starts to decrease from the beginning of the physics run and it hits the minimum on around early April 2017 while the gain fluctuates in between. Then the gain increases back to ~85% of original gain on around late June 2017, and stable since. The cause of this behavior is still unknown, as there is only limited information on the LS system that can be gained from the current detector DAQ configuration. However, it is important to correct the LS gain based on p_1 of each sub-run as it will impact the signal event selection of COSINE-100. The LS spectrum shows stable trend over time after the correction as shown in Figure 3.9(b).

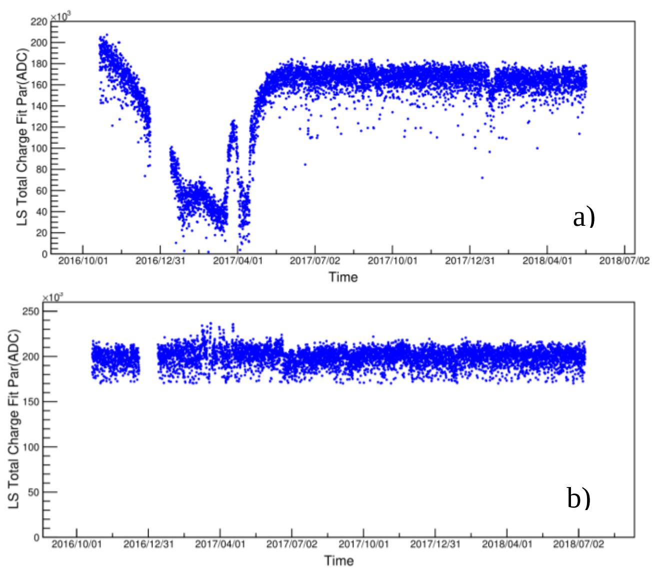

Figure 3.9 (a) LS gain fluctuation as a function of time before and (b) after the correction.

3.2.2 Calibration of liquid scintillator

The total charge sum from all 18 PMTs after the gain correction shows two shoulders that are expected to be coming from energy deposited by gamma rays from ^{40}K and ^{208}Tl is shown in figure 3.10. Since LS spectrum does not have mono-energetic features that could be used for energy calibration or estimation of the energy resolution, we compare data with simulation to get the LS veto calibration factor. The energy deposited by all the detector materials to the LS, the coincidence events tagged by both crystal and LS were derived from a simulation. The simulated ^{40}K events (which deposit 3.2 keV X-ray on the crystals and 1462 keV gamma events in liquid scintillator) are matched to data with the shoulder around 1462 keV as shown in Figure 3.10.

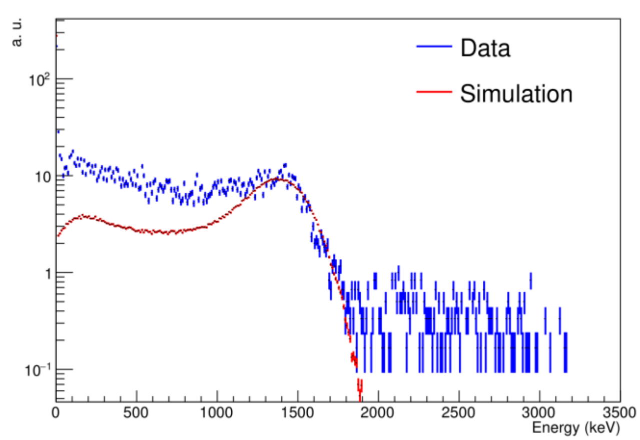

Figure 3.10 Liquid scintillator veto tagging spectra for crystal events with energies between 2-4 keV.

3.2.3 Threshold selection for LS

The LS detector is the passive detector so that LS data is triggered only when one or more NaI (Tl) crystal satisfy the trigger condition. The event taken time window for crystal DAQ and LS DAQ are 4 μs and 60 μs respectively. The crystal PMT are fired when they find a 200 ns coincidence window with other PMT. It indicates that within ~60us window of LS DAQ, ~200 ns time window per a triggered event acts as an intrinsic dead time.

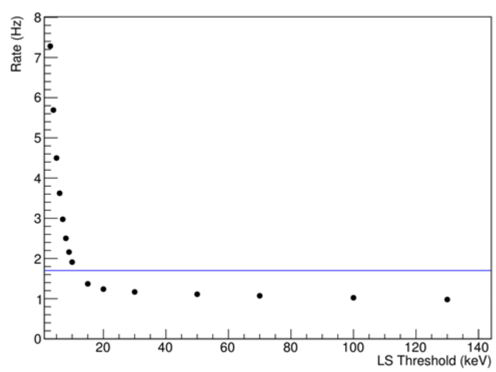

Figure 3.11 LS trigger rate as a function of LS threshold. The line is drawn at 1.7 Hz, which represents 0.5% dead time of LS DAQ .

LS analysis threshold is estimated to minimize the dead time at the level of 0.5%, which is a conservative dead time value for determining the threshold that removes noise events to an appropriate degree. Figure 3.11 shows how the LS trigger rate changes as a function of the threshold. With the higher analysis threshold, the LS trigger rate decreases as fewer number events pass the threshold. This suggests that by having a threshold of 80 keV, 0.5% deadtime is achieved for the LS data taking. Also, a study confirmed that the 80 keV threshold ensures the minimum change of the dead time between different run periods.

3.2.5 Background tagging efficiency

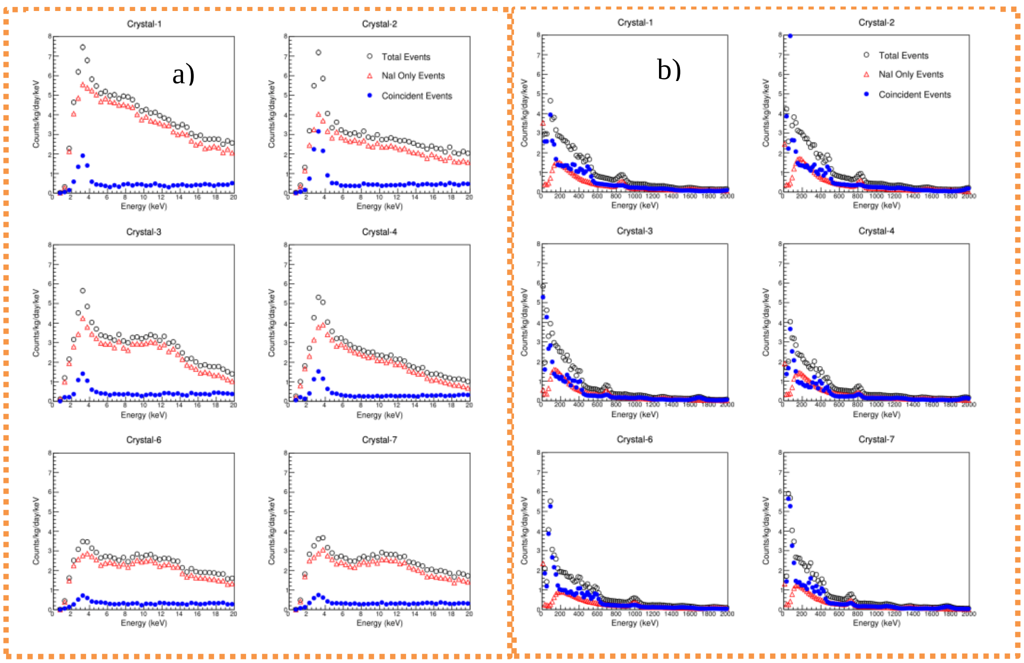

Figure 3.12 Background energy spectra of the six NaI(Tl) crystal in the COSINE-100 detector system, for a) low energy b) high energy. Blue events are vetoed events that have hits on the LS veto detector with energies greater than 80 keV, whereas red events are hits on crystal detector only. The total hits (black) represents all events.

The tagging efficiencies for ^{40}K using the coincidence analysis are calculated as shown in Table 3.2 by counting event rate in the NaI (Tl) detectors with and without LS veto requirement. The ^{40}K tagging efficiencies at different energy ranges are estimated after simulating internal ^{40}K events in to the detector. It shows that the tagging efficiency of the ^{40}K events ranges from 65% to 75%. The un-tagged events are due to nearly 1462 keV γ-rays escaping without any trace in the LS veto detector. The estimated efficiency is most significant in the energy range of 2-4 keV because the tagging efficiency of the LS veto system for ^{40}K is the most effective. The crystals 1 and 4 are located at the edges of the crystal array and hence surrounded by relatively large LS volume so that they have higher efficiency while crystals 6 and 7 are mostly surrounded by neighboring crystals such that they have lower efficiency among other crystals.

Table 3.2. Total tagging efficiencies for six crystals in COSINE-100 detector system

Total Tagging efficency (%)	Crystal-1	Crystal-2	Crystal-3	Crystal-4	Crystal-6	Crystal-7
6-20 keV	10.88	16.52	13.98	14.39	13.06	13.15
100-1500 keV	57.53	54.69	50.92	49.79	61.92	57.68

^{40}K tagging efficiency for six crystals, estimated using Geant4 simulation

^{40}K Tagging efficiency (%)	Crystal-1	Crystal-2	Crystal-3	Crystal-4	Crystal-6	Crystal-7
2-4 keV	75.12	72.72	69.08	75.94	66.52	65.80
2-6 keV	73.51	71.16	67.54	74.46	65.18	64.39
0-10 keV	71.35	69.02	65.56	71.58	63.08	62.42

3.3Event selection

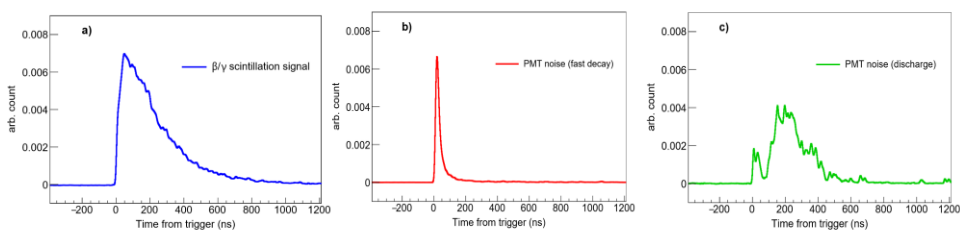

Figure 3.13 The accumulated event shape below 10 keV that passed the trigger condition a) signal like scintillating events in NaI(Tl) crystal b) fast decay PMT noise events c) discharge PMT noise events.

The COSINE DAQ triggers three classes of the events as shown in figure 3.13. So, we can reject PMT noise by using different variables related to charge and time [57]. However, there are several analogous types of events at very low energy because of the low number of SPE's and hard to discriminate by a single variable. So, a multivariable analysis called Boosted Decision Tree (BDT) [85] is used to select the physical events.

3.3.1 Pre-selection and Boosted Decision Tree (BDT)

Different types of the events are triggered due to the dark current on PMTs, muon and LS coincident events, oscillation type of events and pre-pulse events that can be removed by a simple noise selection cut called 'precut'. The coincidence events within the 30 ms (equivalent to the 0.1% deadtime) from the muon events are removed by using the muon cut as shown in figure 3.14(a). Because of the large tail from the muon induced events, accidental early pulse events are triggered as shown in figure 3.14 (b) which can be removed by using the second cluster trigger time cut greater than 2.0 μs. The dark current is typically generated due to the SPE radiated from the PMT photocathode and can be removed by using the number of cluster charges with values greater that of each PMT. Sometime detector suffers from the additional periodic noise as shown in figure 3.14(c) because of the external construction-related work near to the detector inside the tunnel that is removed by accounting the pulse height that shows a negative charge below its software threshold.

The isotopes such as ^{40}K, ^{214}Bi, and ^{22}Na make double or triple coincidence and can deposit energy to the neighbor crystals or LS veto detector. Since the cross-section of the WIMP-nucleon interaction is expected to be extremely small so that coincidence hit from WIMPs candidate signal events can't be imagine. Single hit (which make hit to the target crystal only) and multiple hit (which can hit two or more crystals) selection criteria is developed in this analysis where multiple hit events are vetoed events from WIMP search analysis. Any event that hits the target crystal and deposit energy more than 80 keV on the LS veto detector and the neighbor crystals having number of clusters more than four is the optimized selection criteria for multiple hit events. The events filtered from precut is used to select the scintillating events as discussed into below section.

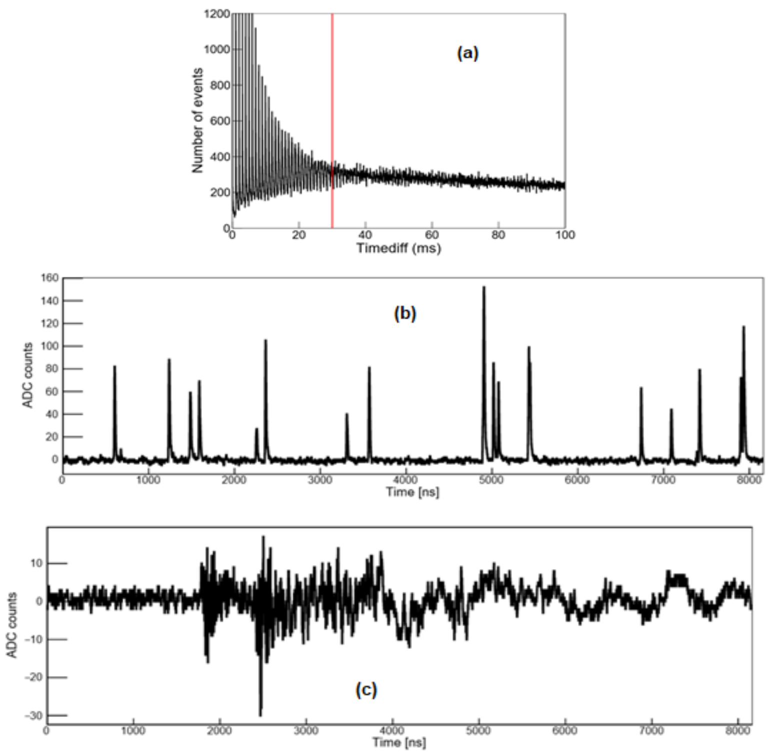

Figure 3.14 The set of pre-cuts used to remove accidental events a) time difference between muon and crystal hit events where red lines shows the selection to remove muon events b) phosphorescence events c) an oscillating type events caused by external activities inside the tunnel.

3.3.2 BDT input variables and training

DAMA/LIBRA collaboration uses a ratio of slow and fast charge cut to remove the PMT-noise-like events and called "DAMA Cut" in later literature. Other independent cuts like charge asymmetry cut and average cluster charge cut are developed to reject the PMT noise. The details of this cut definition are found with ref [57]. This set of cuts is called 'box cut' and the distribution of such cut parameter space is as shown in figure 3.15. The BDT method that includes each of the above dominant variables as an input and returns signal classifier as output is more efficient to separate PMT noise like events. The input variables used in BDT are listed as below.

1. Slow charge (X1): a fractional charge in [100 ns, 600 ns] window to total charge in [0 ns, 600 ns] window for each PMTs
2. Fast charge (X2): a fractional charge in [0 ns, 50 ns] window to total charge in [0 ns, 600 ns] window for each PMTs
3. Meantime (nmt500): Charge weighted meantime within 500 ns window after the trigger time for each PMT
4. Charge asymmetry: $\frac{q_1 - q_2}{q_1 + q_2}$ where q_1 and q_2 are integrated charge seen in each PMT
5. Average cluster charge (q_c/n_c): Average charge per cluster
6. Charge sum (qc5): Total charge sum within 5 μs window.

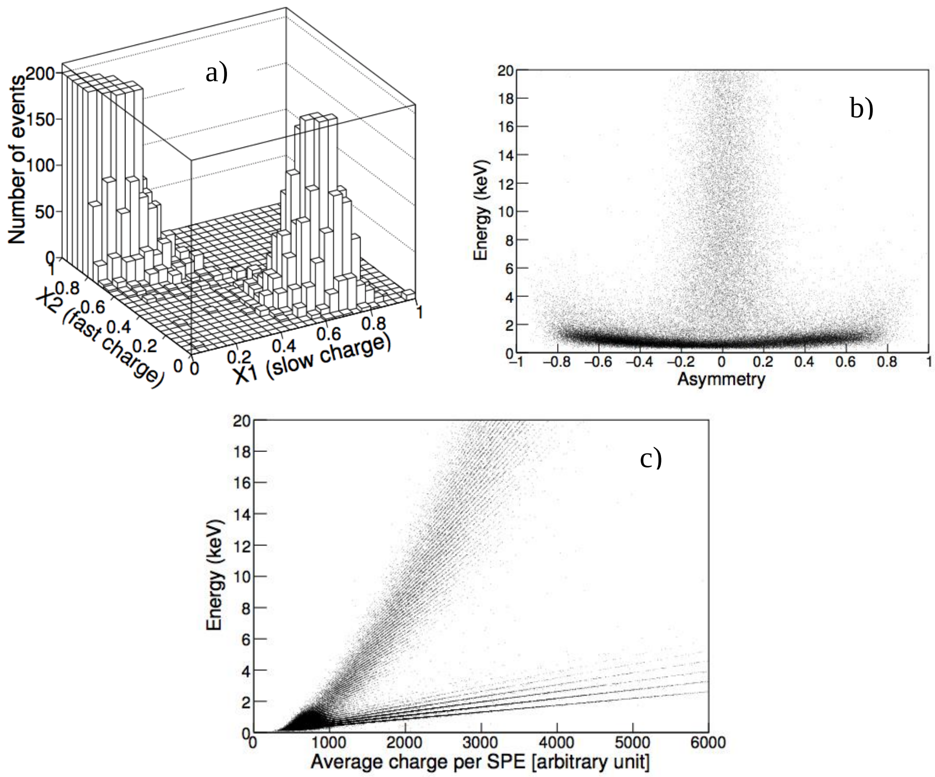

Figure 3.15 The distribution of the different parameters in background run used to select the scintillating events a) DAMA parameter space between slow and fast charge for the events below 10 keV. b) Charge asymmetry distribution between two PMTs in a single crystal c) The average cluster charge per SPE.

The BDT method accounts for the correlation between individual parameters. This method is useful to combine several discriminating variables to a single variable. So, BDT training is performed to reject the low energy PMT noises. The decision tree undergoes through multiple iterations based on the input features of the physical events and PMT noise samples. As the iteration goes on, preceding event sample weights are updated and the consecutive learner is trained on the weighted data set. Eventually, a single classifier is obtained by combining the weak hypothesis with the corresponding weights as a BDT.

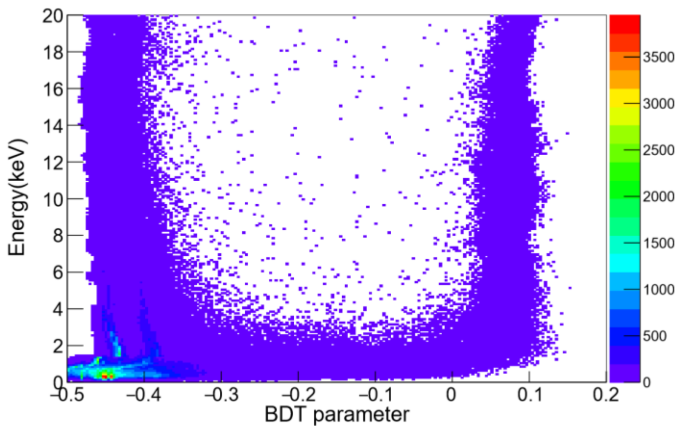

Figure 3.16 The scatter plot between energy vs BDT weight for Crystal 6. There is a clear separation of the noise band on left and the signal band on right, all the way down to 2 keV.

An external gamma calibration data having the lifetime of 13.9 days is taken by using the ^{60}Co disc source with a 74 Hz rate. The coincidence beta events from ^{60}Co calibration run in energy meantime parameter space are used to select the signal sample and the normal background run from the first 48.2 days is used to collect the noise sample for BDT training.

Both sample events are selected for the energy range below 30 keV. The BDT weighted parameters obtained after the training as a function of the energy is shown in figure 16. The noise band and scintillation signal band are selected up to 2 keV. So 2 keV analysis threshold is settled down for this round of the analysis. The cut values are optimized to select the scintillation events.

3.3.3 Second class of the BDT weighted variable (BDTA)

The BDT selection as discussed in Section 3.3.2 is a powerful tool to reject the regular PMT noise. However, few crystals suffer from a different class of infrequent noise like events. This noise event has a ‘bell-shaped’ waveform, that is wider and symmetric than regular PMT noise events as shown in figure 3.1(c). Due to its specific shape, it's hard to classify the difference between bell-shaped events and scintillating events at low energy below 10 keV because of a relatively smaller number of SPE in very low energy. Around 9% of the data is evenly distributed over time and is selected for blinded analysis. The temporal event rate as a function of the time for blind data is shown in figure 3.17. The bell-shaped PMT noise events are found to be in crystal 1, crystal 2 and crystal 7 in the specific time window. Crystal 1 is affected more severely and randomly distributed over time while Crystal 7 is localized between Jan 12 to the end of March 2017. Crystal 2 is having a very short burst of these noise events in the earlier run.

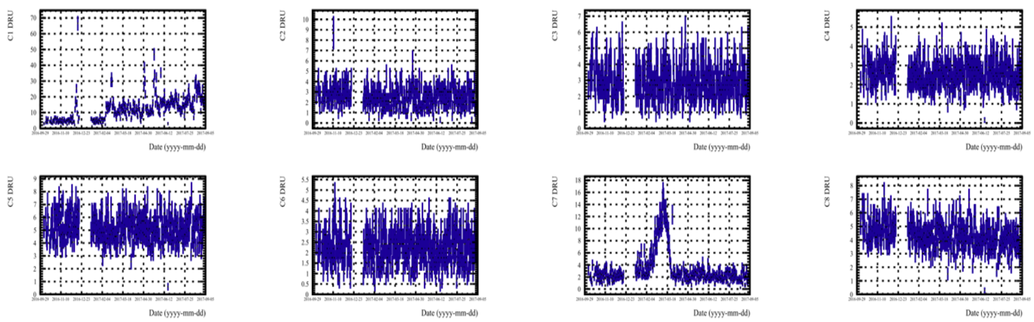

Figure 3.17 The time series event rate below 20 keV for all the crystals after regular event selection applied. The elevated rate in Crystal 1, Crystal 2, and Crystal 7 indicates the bell-shaped PMT noise events' existence.

These bell-shaped events are highly populated to Crystal 1 so this crystal is selected to develop the new BDT weight called "BDTA". Additional variables were developed so that it can take the shape difference between bell-shaped PMT noise and the usual scintillation events. Both crystals and PMT based meantime, the ratio of slow to fast charges (X1/X2) and energy is the input for BDTA. The variance of the mean time (nvt) in 1000 ns as described in equation 3.3 and charge accumulation time (CAT) at 95% charge fraction for each PMT are used as a new input variable for BDTA training.

$$\sigma^2 = \frac{\sum_i^{1000ns} q_i t^2}{\sum_i^{1000ns} q_i} - < t >^2, \tag{3.3}$$

where q is the charge and t is the corresponding meantime.

The scintillating events after using BDT cut from the background run 1544 (100 sub-runs, which is not suffering from bell-shaped noise) is used to select the signal sample and the background run 1546 (134 sub-runs which is suffering from bell-shaped noise) is used to select the noise sample for BDTA training. The new BDT weights, i.e. BDTA vs energy parameter using run 1546 for all crystals are shown in figure 3.18. The bell-shaped noise events populate to the left band and scintillating signals on the right band.

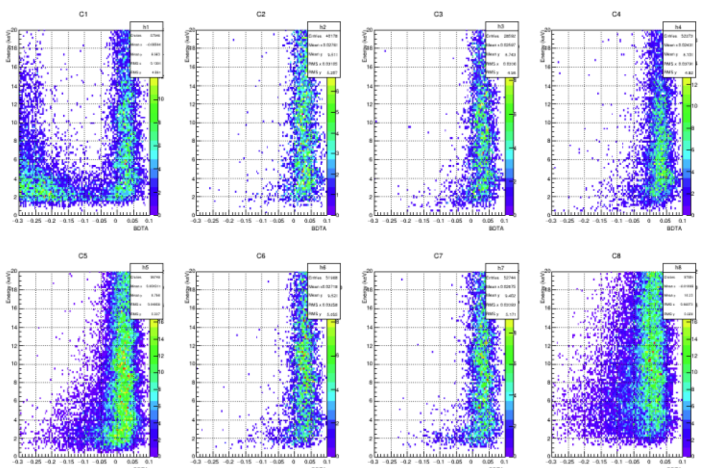

Figure 3.18 BDTA distribution for Run1546 which having high rate of bell-shaped PMT. Crystal 1 clearly shows the noise band on left.

The BDTA selection is optimized after modeling the BDTA distribution so that the noise rejection rate should be more than 99.5%. The comparison event rate of the blind data with

BDT selection and BDT plus BDTA selection is shown in figure 3.19. A significant amount of the bell-shaped noise is removed after adding a newly developed BDTA parameter in the event selection criteria. The crystal 7 bell-shape noise is removed quite effectively after adding BDTA selection. However, Crystal 1 shows a very unstable behavior over the entire run and excess large number of the events from Crystal 2 (from set1 data) and Crystal 7 (run 1616 and 1617). Such instabilities into the event rate from Crystal 1, Crystal 2, and Crystal 7 becomes very sensitive for time dependence analysis. So, we decided to remove the entire data for Crystal 1, Set1 data for Crystal 2 and run 1616 (total) and run 1617 (sub-run 0-200) for Crystal 7 in this round of the analysis.

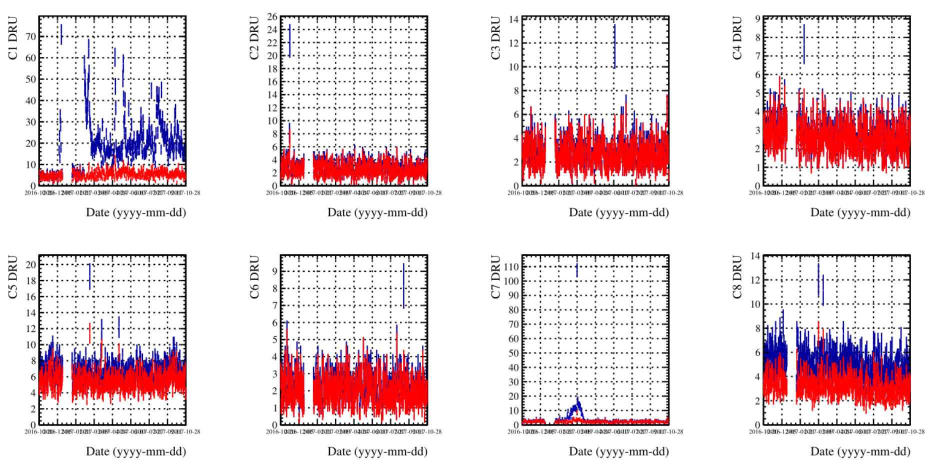

Figure 3.19 The time series event rate below 20 keV for all the crystals before (blue) and after (red) BDTA selection after regular event selection.

^{60}Co calibration run is used to estimate the event selection efficiency. The ratio of the survived events after the selection to the total signal events, the efficiency is calculated with binomial statistics. In figure 3.20, the bottom panel shows the selection efficiency of the current event selection as a function of energy, and energy spectra of five crystals for set2 data used in this analysis from 0 to 20 keV with the efficiency corrected. The selection efficiency at the threshold region is maintained by more than 60 % for each crystal. These spectra are well understood by comparing the data with GEANT4 simulation [86], where the overall background levels in Crystal-6 and Crystal-7 are lower than other crystals due to their lower ^{210}Pb and ^{40}K contamination levels.

3.4 Cosmogenic activation

The COSINE crystals having different times of the initial deployment at Y2L varies from few months to few years and the cosmogenic activation is inhomogeneous among the crystals. Such a time-dependent component can conflict or mimic with annual modulation search and it causes a false positive result over the physics search. So, identifying the background originated from the cosmogenic activation and constraining the level while modeling the time-dependent signal are performed in annual modulation analysis. The beta-decay spectrum of tritium has endpoint energy of 18 keV and the electron capture decay of

^{22}Na produces ~0.8 keV X-rays. The beta decay of ^{129}I to ^{129}Xe is followed by ^{129}Xe transitioning to the stable ^{129}Xe isotope via the emission of a 39.6 keV γ-ray [87].

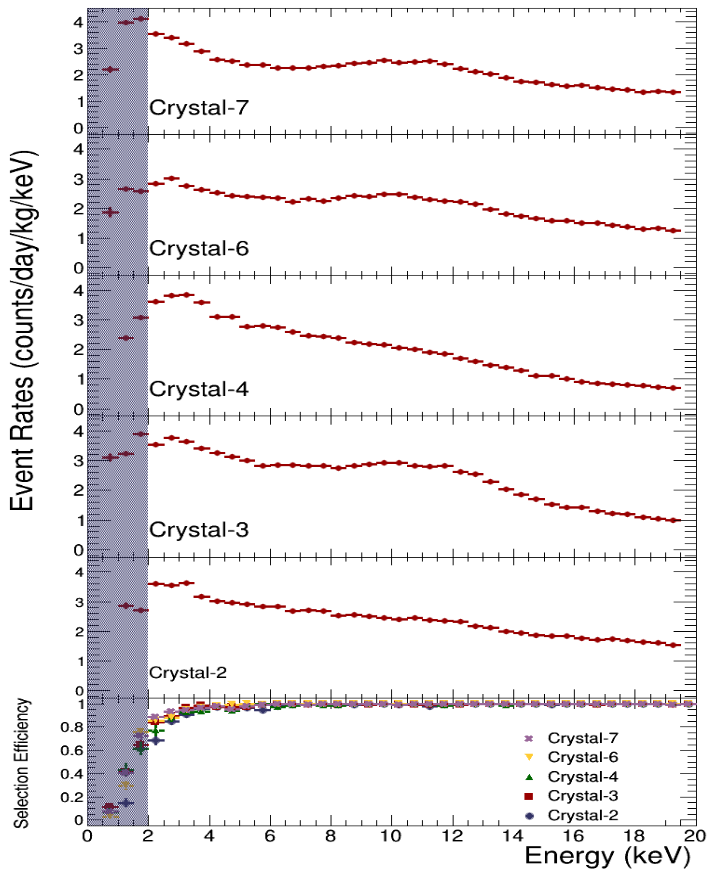

Figure 3.20 The background energy spectrum in our ROI after efficiency correction for the best five crystals used in this analysis (top panels) and signal selection efficiency estimated from the calibration run (bottom panel)..

These low energy contributing components are simulated to estimate their activities via the decay rate. That can be done by integrating the rates over the specific energy ranges, plot it over time, and fit to the decay rate of the particular cosmogenic. The decay rate can be modeled by an offset plus one or more exponential functions depends on the selected energy region like as in equation 3.4.

$$A + B \cdot e^{\frac{-\ln(2)(x-x_0)}{C}} \tag{3.4}$$

where x_0 is the initial time, A is the offset, B is the rate in DRU unit at x_0, and C is the half-life. Here, parameter B is extracted from the fit to get the initial amplitude (approximately around the beginning of the physics run) of the cosmogenic isotopes. The extrapolated rates at the beginning of the physics runs can be converted to the activity (Bq/kg) by using the equation 3.5.

$$Rate = \frac{\Delta E \times B}{86400 \times f_{\Delta E}} \tag{3.5}$$

where ΔE is the fraction of the events from that cosmogenic depositing energy in the specified integration region, and it can be calculated from the simulated spectra.

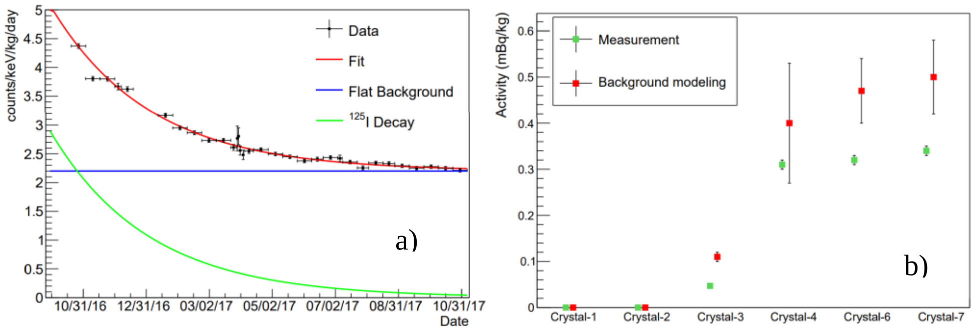

Figure 3.21 a) Decay rate between 60 – 70 keV single hit events modeled with an exponential component having half-life equivalent to ^{125}I. b) Comparison of the average activities from the first 60 days of the data extracted from this method (green) with an independent background modeling method (red)

All the crystals used in this analysis are activated by a common cosmogenic isotope of ^{125}I which has shorter half-life of 59.4 days and deposits at 30-40 keV and 60-70 keV energy range via electron capture. The contribution from the ^{121m}Te in the range of the 60-70 keV is almost negligible so 60 -70 keV energy range is integrated and modeled with half-life of the ^{125}I to estimate activity as shown in figure 3.21 (a). The estimated activity of all crystals are compared with the activity estimated from another independent method of background modeling [86]. Other components were studied with same technique and the average activities are summarized in table 3.3. Such quantitative estimation can be used to constrain the time dependent background contribution from the cosmogenic component in COSINE WIMP search data.

Table 3.3. Initial activity of ^{121m}Te, ^{127m}Te, and ^{113}Sn in each crystal as measured by the decay rate method (unit are in mBq/kg). Crystal 2 shows null result because of the long cooling time.

	Crystal-2	Crystal-3	Crystal-4	Crystal-6	Crystal-7
^{121m}Te	-	0.90±0.16	0.89±0.06	0.44±0.07	0.41±0.07
^{127m}Te	-	0.87±0.16	0.48±0.03	0.38±0.04	0.35±0.04
^{123}Sn	-	0.16±0.04	0.14±0.02	0.15±0.01	0.12±0.01

3.5 Annual modulation analysis

The scintillating event after applying all the developed cuts from set2 data having 97.7 kg year exposure is used for modulation analysis. The time dependence systematic which might be originated from environmental factors or detector's instability like gain or calibration or light yield is well controlled as discussed in Section 3.1 for this analysis. The sideband events are modeled with the combination of the linear plus single exponential plus sinusoidal function to validate the fit machinery. Then final fit is performed to the data over 2 to 6 keV energy region and the modulation amplitude and phase are extracted. The details of the modulation analysis techniques are discussed in the below section.

3.5.1 Modulation fit model

The set2 data from October 21, 2016 to July 18, 2018 that passed the event selection criteria as discussed in the section 3.3 is divided into each 15 days bin to study the time dependence of the event rate. The signal region for annual modulation search is 2-6 keV single hit events. The two more-sideband energy region single hit 6-10 keV and multiple hit 2-6 keV region and having similar amount of statistics are chosen to develop and validate the fitting machinery. The efficiency corrected total event rate in signal range as a function of the time is displayed as in figure 3.22. The x-axis is a conservative timestamp unit for display purpose where zero is equivalent to the 1st January, 2016 and first bin of each crystals is equivalent to 21st Oct, 2016. However, set1 data is removed from C2 so that first bin for C2 in this plot is equivalent to 12th Jan, 2017. There was calibration campaign from 19th Dec 2016 to 12th Jan, 2017 so that there are two empty bins after 4th bin for all crystals except C2. Additional bins are missing for C7 because of the bell-shaped noise data which is removed from this analysis.

The data doesn't show any unusual outliers indicating the stability of the event selection criteria. The total event rate is minimum for C6 and C7 because of the low level of its internal background from ^{210}Pb and ^{40}K. C3 and C4 are newly deployed crystals at Y2L that's why it has relatively higher rate because of the cosmogenic components. The total event rate is decreasing as a function of the time because of the decay of the cosmogenic components. Such decreasing rate is higher to newly deployed crystals like C3 and C4 because of the fast decay of the short-lived isotopes like ^{125}I.

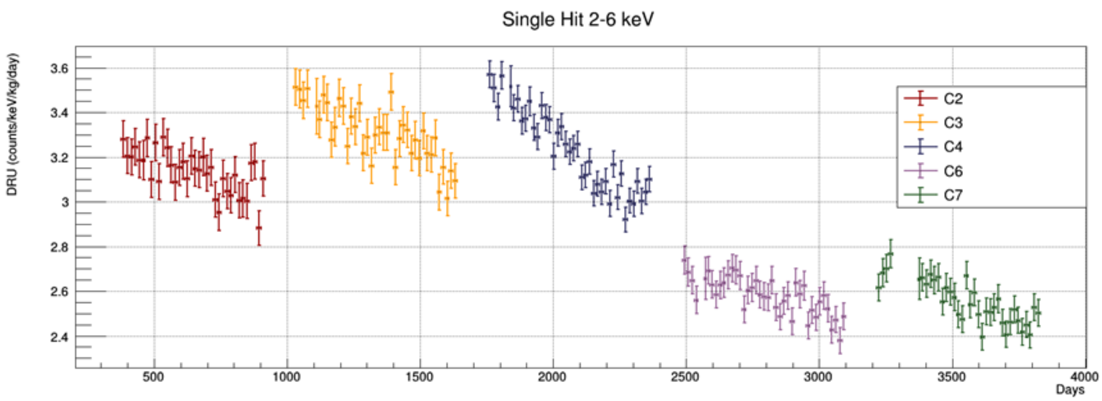

Figure 3.22 Event rate as a function of the time for all five crystals. The empty bin in C7 around 3300 to 3400 is because of the removed data which is affected by bell-shaped PMT noise

The model with an offset for its fixed background, exponential component for time varying cosmogenic isotopes and sinusoidal component to extract the modulating behavior is the proper candidate to model the background rate. The model function to fit the data is used as in equation 3.6.

$$Rate = C + p_0 \exp\left(-\frac{ln2t}{p_1}\right) + Acos\frac{2\pi(t-t_0)}{T}, \qquad (3.6)$$

where C is a constant, p_0 and p_1 are fitting parameters for the exponential background model, A is a modulation amplitude, t_0 is a phase, and T is the modulation period. The offset (C) is constrained from the detector background modeling [86], exponential parameters (p_0 and p_1) corresponds to the cosmogenic components whose half-life and initial activity can be constrained as discussed into the section 3.4. The phase is fixed with either standard halo model (expected phase 152.5 days) or DAMA/LIBRA best fit phase (144 days), and the period is fixed 365.25 days. As the background contributions to each crystal are different where the modulating component is supposed to be correlated across all the crystals, a simultaneous fit has been performed.

Figure 3.23 shows the COSINE-100 event rates for each energy bin before and after subtracting off cosmogenically activated isotopes' components. Fitted lines are with the simultaneous fit of exponential background and sinusoidal function for the un-subtracted rate, and with the sinusoidal function alone for the subtracted rate. Vertical blue arrows point to June 2, the peak date in the modulation reported by DAMA/LIBRA [75].

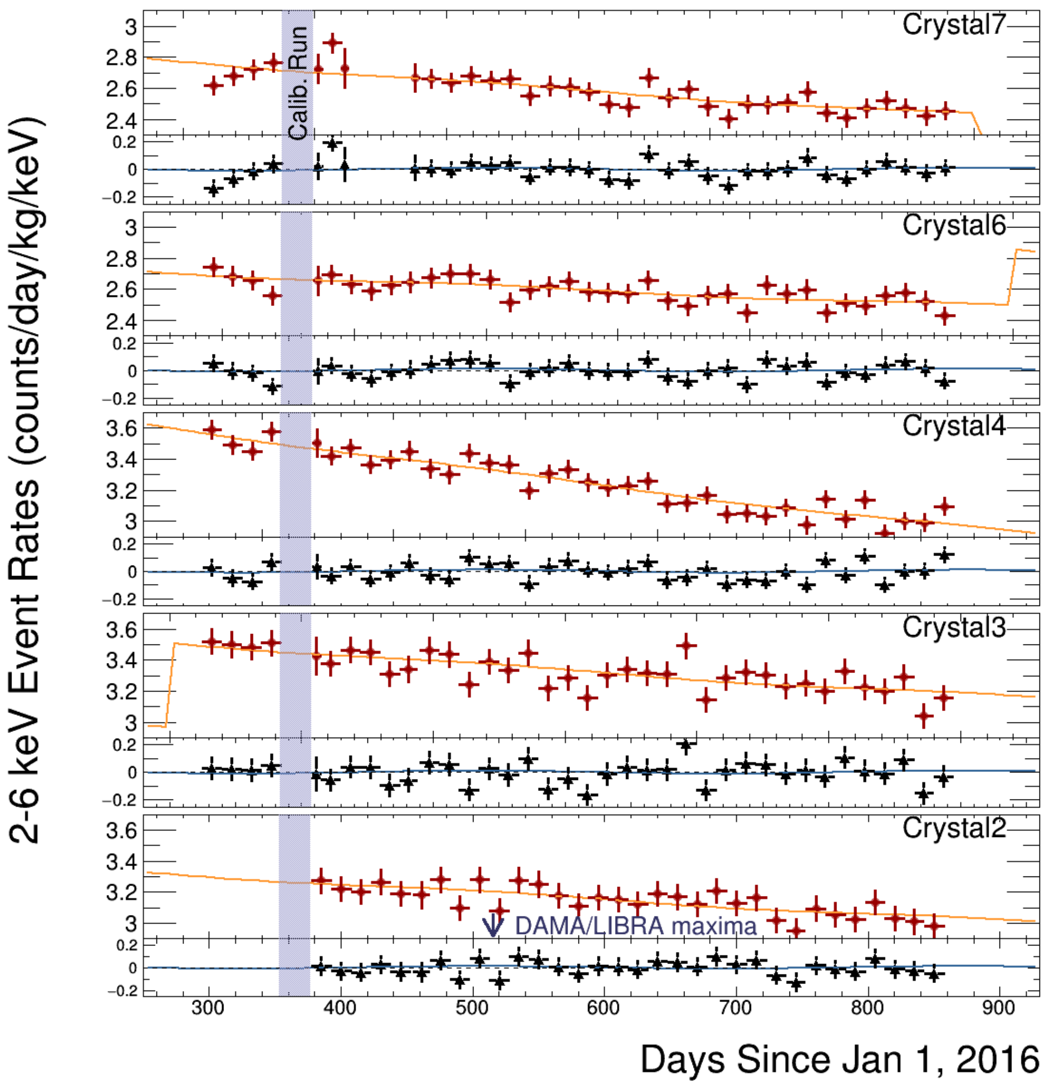

Figure 3.23 Event rate vs. time for each crystal, both the rate before background subtraction (red) and after the subtraction (black), in 2–6keV energy region for single hit.

To perform the modulation analysis, a chi-square minimization fits the event rate over time for each energy bin with a sinusoidal at top the exponential cosmogenic background. The amplitude of the possible annual modulation of dark matter with the modeled background in each energy bin, a χ2 test with equation 3.7 is carried out.

$$\chi^2 = \sum_i \frac{[M_i - E_i]^2}{M_i} + \sum_j^5 (\frac{p_j - P_j}{\delta P_j})^2 \,, \quad (3.7)$$

where M_i and E_i are the measured and expected values, p_j & P_j are the nuisance parameter (flat constant value constrained from background modeling) δP_j is the uncertainty of measured component and j is the constant term index for each crystal.

3.5.2 Sideband sample modeling

Independent samples are studied to test any possible fake positive results due to fitting tools or any systematic because of the specific modeling. Any control sample in which WIMP dark matter interaction can't be expected is the candidate for the sideband samples. So, multiple hit events and single hit events close to the ROI are the best candidates for the sideband sample. The sideband sample 6-20 keV single hit which has similar statistics with a signal allowed region of 2-6 keV single hit are modeled as shown in figure 3.24. Sideband data fits well with exponential models built with the known cosmogenic components. Other control sideband sample i.e. single hit [6-10 keV] and multiple hits [2-6 keV] are well modeled and return the null amplitude as summarized to Table 3.4.

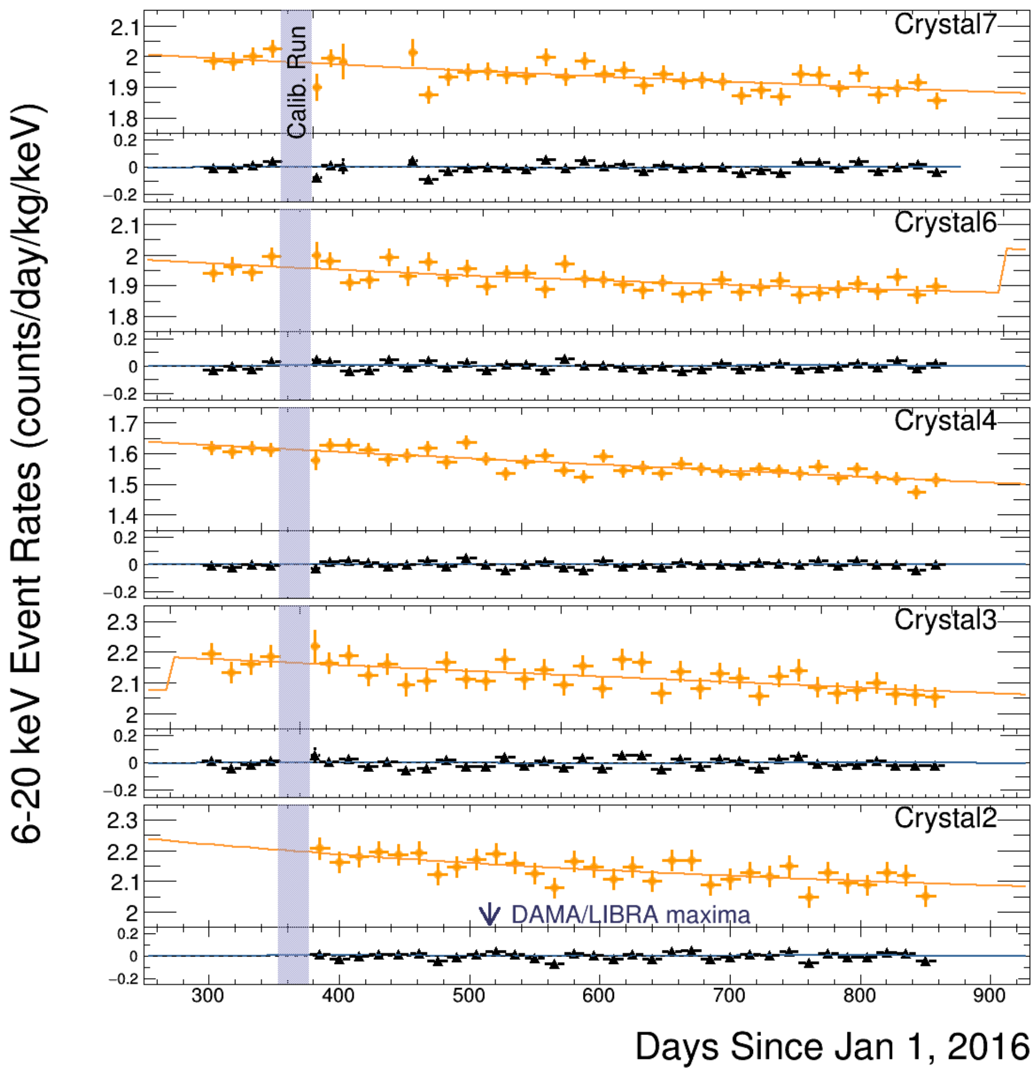

Figure 3.24 Event rate vs. time for each crystal, both the rate before background subtraction (red) and after the subtraction (black), in 6–20keV energy region for single hit.

Table 3.4. Summary of the result of the fit models for different sideband samples with fixed phase and period using the model as in equation 3.7.

Energy Interval (keV)	χ^2	d.o.f.	Amplitude (counts/day/kg/keV)	Phase (Days)	Period (Days)
2-6 [Multiple Hit]	204.0	175	-0.0016±0.0020	152.5(fixed)	365.25 (fixed)
6-10 [Single Hit]	164.0	163	0.0034±0.0030	152.5(fixed)	365.25 (fixed)
6-20 [Single Hit]	164.0	162	-0.0008±0.0030	152.5(fixed)	365.25 (fixed)

3.5.3 Modulation fit result

The total event rate in the ROI (single hit, 2-6 keV) having 2.7 counts/day/kg/keV on average is modeled with the function as discussed in Section 3.5.2 as shown in figure 3.24. The chi-square minimization fits to scan the modulation amplitude with the condition of a fixed period of one year and both free and floated phases are executed over the data. The amplitude is scanned with a fixed phase based on the standard halo model of 152.5 days and the DAMA modulation amplitude-phase of 145 days independently. Eventually, the amplitude is scan after floating the phase. The best fit for the 2–6 keV range has a modulation amplitude of 0.0092±0.0067 counts/keV/kg/day with a phase of 127.2±45.9 days. Log-Likelihood parameter estimation of the annual modulation with amplitude and phase as free parameters shows that the current data from COSINE-100 is consistent with both the DAMA/LIBRA annual modulation result and the null hypothesis at the 68.3 % C.L.

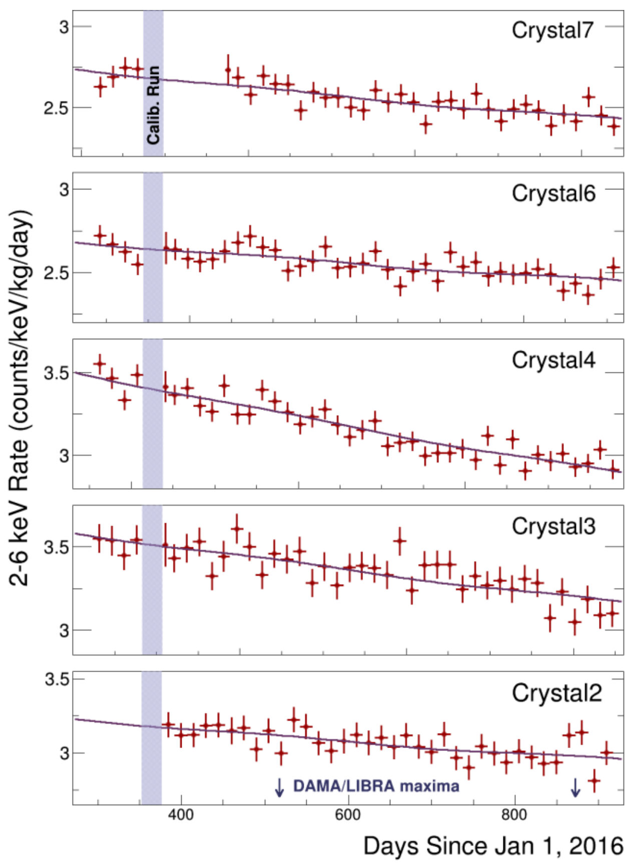

Figure 3.25 Rate vs. time for Crystals 2, 3, 4, 6, and 7 for the 2–6 keV energy region binned in 15-day intervals. Solid blue arrows indicate the peak date in the modulation as reported by DAMA/LIBRA [75].

A Feldman-Cousins method [88] was also used to cross-check the result, and returned a consistent C.L as shown in figure 3.26.

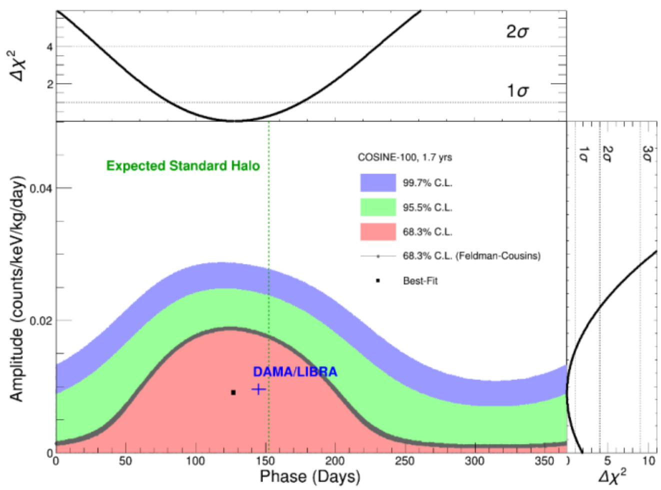

Figure 3.26 The COSINE-100 best fit and 68.3 %, 95.5 %, and 99.7 % C.L. contours as a function of modulation amplitude (counts/day/kg/keV) and phase relative to January 1, 2015, for period fixed at 365.25 days. Top and side panels show the dependence of $\Delta\chi^2$ as a function of phase and amplitude, respectively, along with two-sided significance levels.

As a cross-check, we show the fit results to the annual modulation with and without the LS veto. The LS veto removes backgrounds and improves the uncertainties on the annual modulation amplitudes by 7 %. Table 3.5 summarizes the result of the various fitting scenarios used for the 2–6 keV energy interval. The best-fit modulation amplitudes as a function of energy with 1 keV energy bins are shown in figure 3. 27. These fits were performed with a fixed period of one year and the phase fixed at 152.5 days. We expect approximately 3σ coverage of the DAMA region using the same target within five years of data exposure.

Table 3.5. Summary of fit result for the modulation and null hypotheses for the 2-6 keV energy region in COSINE-100. The result without using the LS veto is presented as a cross-check. DAMA/LIBRA result [51] and the ANAIS-112 2019 result [52] are also shown.

Configuration	χ^2	d.o.f.	p-value	Amplitude (counts/day/kg/keV)	Phase (Days)
COSINE-100	175.3	174	0.457	0.0092±0.0067	127.2±45.9
DAMA/LIBRA (Phase1+Phase2)	-	-	-	0.0096±0.0008	145±5
COSINE-100	175.6	175	0.473	0.0083±0.0068	152.5 (fixed)
COSINE-100 (Without LS)	194.7	175	0.143	0.0024±0.0071	152.5 (fixed)
ANAIS-112	48.0	53	0.67	-0.0044±0.0058	152.5 (fixed)
DAMA/LIBRA (Phase1+Phase2)	71.8	101	0.988	0.0095±0.0008	152.5 (fixed)

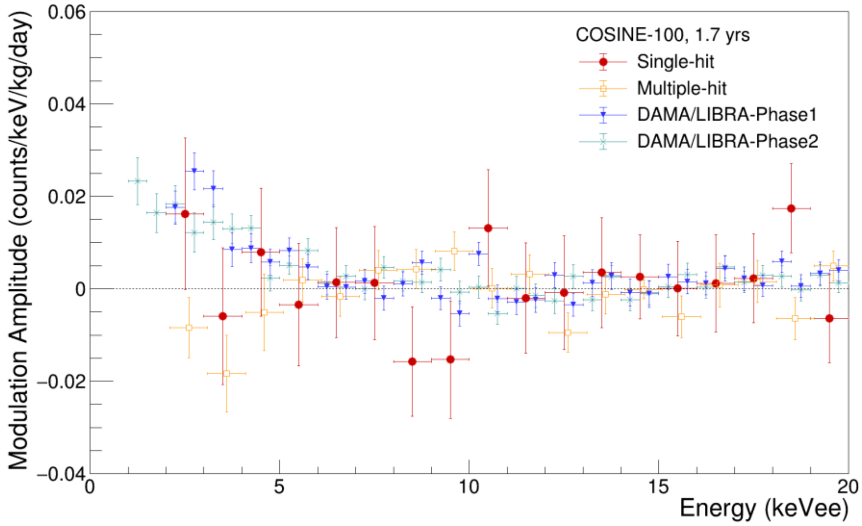

Figure 3.27 Modulation amplitude as a function of energy in 1 keV bins for the 1.7-year COSINE-100 single-hit (red closed circle) and multiple-hit (orange open circle). DAMA/LIBRA phase 1 (blue) and phase 2 (green) from Ref. [51] are also shown for reference. Period and phase are fixed at 365.25 days and 152.5 days. Horizontal error bars represent the width of the energy bins used for the analysis. Vertical error bars are $\pm1\sigma$ error.

Chapter 4

Lowering the analysis threshold

DAMA/LIBRA collaboration have upgraded their PMTs with higher quantum efficiency of 33% - 39% at NaI(Tl) emission wavelength of 420 nm. They are commissioning the phase2 of their experiment since 2011 and achieved the analysis threshold at 1 keV and persistent modulation with large exposure ranging from 1 keV to 6 keV. The COSINE-100 made a noble effort to lower down the analysis threshold from 2 keV to 1 keV for an ample to ample comparison of DAMA modulation signal. The lowered threshold can improve the sensitivity of the WIMP-nucleon interaction search because of the expected exponential dark matter particle spectra which is more effective to the lower mass region. This chapter describes about the method used to reach the 1 keV threshold and background understanding of set2 data with 1 keV threshold.

4.1 Parameter Development

COSINE 100 used BDT technique to distinguish between scintillation signal and noise signal over their WIMP search data. The purity of signal sample for BDT training is the key-factor to lower down the energy threshold. The charge weighted meantime is the available best parameter which can separate the scintillation sample and noise. However, this parameter can't discriminate noise and signal below 2 keV. So, development of new parameter having better discriminative power is necessary to achieve the threshold below 2 keV.

4.1.1 Detector calibration using non-linear calibration function

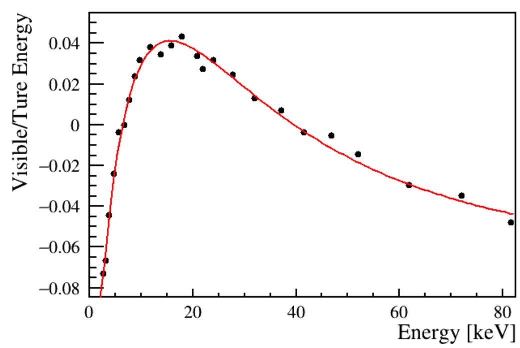

Figure 4.1 The non-linear calibration function measured by [89]. The data is modelled by using the empirical function defined as in equation 4.1.

Several experiments report that NaI(Tl) detector is suffering from non-linearity because of the fluorescence efficiency [89]. The energy scale nonlinearity is one of the systematics in 2 keV physics search and going to be improved for 1 keV search. Such nonlinearity is more severe at low energy region however COSINE-100 has only six possible calibration points below 100 keV. So, an empirical calibration function is modeled based on the nonlinearity response of NaI(Tl) detector data from ref [89] as shown in figure 4.1. This empirical function as shown in equation 4.1 is used to calibrate the COSINE detector as shown in figure 4.2.

$$CalFunc = P_3 \frac{Log(\frac{x-P_1}{P_2})}{(x-\frac{P_1}{P_2})^3} + P_0 \qquad (4.1)$$

Where P_0 is an offset, P_1 is the shift values, P_2 and P_3 are the size corresponds to energy and the normalization offset.

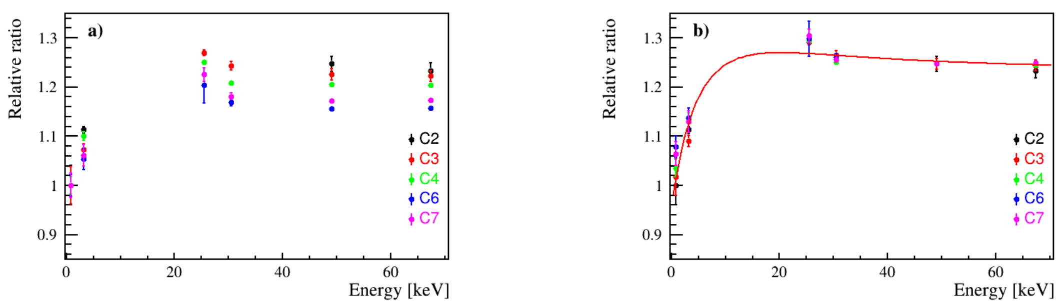

Figure 4.2 a)The non-linearity fraction measured with different COSINE crystals b) The non-linear global calibration function for COSINE crystal.

The function shows crystal dependence behavior because of the limited data for calibration. In principle, each crystal should have similar non-linearity so that we can use a single global function with different offset for each crystal. The calibration data for each crystal are overlaid to the figure 4.2 (a). The COSINE crystals show the nonlinearity of ~20 %. Each calibration point is normalized with ^{210}Pb mean value and empirical function is used to model the data point as shown in figure 4.2 (b). Such non-linear calibration shows the proper alignments of the known isotopes and their corresponding energy scale from 0.8 keV (^{22}Na) up to 67.8 keV (^{125}I) peak.

4.1.2 Decay time parameter

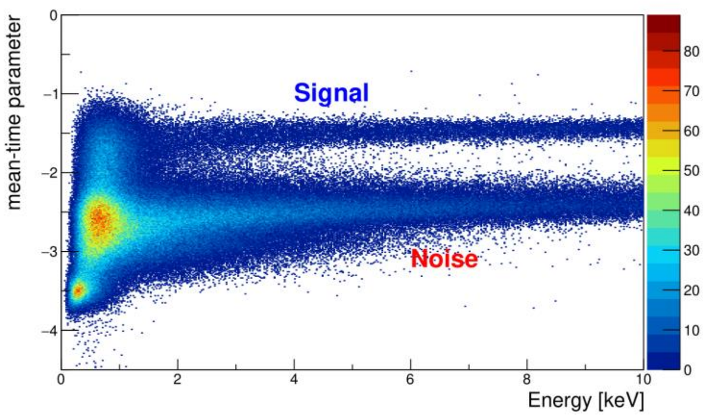

Figure 4.3 Mean-time parameter from normal background run as a function of the energy. The upper band denotes signal like (physical) events and the lower band shows the noise-like (PMT noise) events.

Particle-induced (scintillation) events generally show a longer decay time than that of a PMT noise pulse. The charge weighted mean time of the PMT pulse can separate most of the physical events and PMT noises based on different decay time of pulses. Each event has two values of mean time for each crystal, because two PMTs are attached to a crystal. Since we should merge those values, a parameter p_m, mean-time parameter, is defined as follows,

$$P_{m,i} = \ln (\sum_j^2 < t >_{i,j} \qquad (4.2)$$

where i and j denotes the crystal and the PMT numbering, respectively (i=1, 2, ⋯, 8, j =1, 2), and $<t>_{i,j}$ is charge weighted mean time of j^{th} PMT attached to i^{th} crystal.

The mean-time parameter can efficiently separate physical events and the background noise at threshold of 2 keV as shown in figure 4.3. However, below 2 keV, there are lots of PMT noises that cannot be separated. Those are presumed as another type of noise which has different waveform and a new parameter or method is needed to select physical events. The mean-time parameter does not inherit the characteristics of the decay time completely and the decay time of the physical event is still considered valid for event selection, so new parameter based on decay time of the PMT pulses is developed. Simplified decay time for each PMT can be written,

$$t_{d,j} = \frac{\ln (Q_{tail,j}/Q_{head,j})}{T_{tail,j} - T_{head,j}}, \qquad (4.3)$$

where $t_{d,j}$ is the simplified decay time of PMT j. The $Q_{head,j}$ ($Q_{tail,j}$) is charge sum in first(second) half of PMT pulse and the $T_{head,j}$ ($T_{tail,j}$) is charge weighted mean time of first (second) half. The structure of Eq. 4.2 implies the decay time between ($T_{head,j}$, $Q_{head,j}$) and ($T_{tail,j}$, $Q_{tail,j}$). A new parameter $p_{d,i}$ called the decay-time parameter for i^{th} crystal

$$P_{d,i} = \ln\left(\sum_j^2 t_{d,j}\right) \tag{4.4}$$

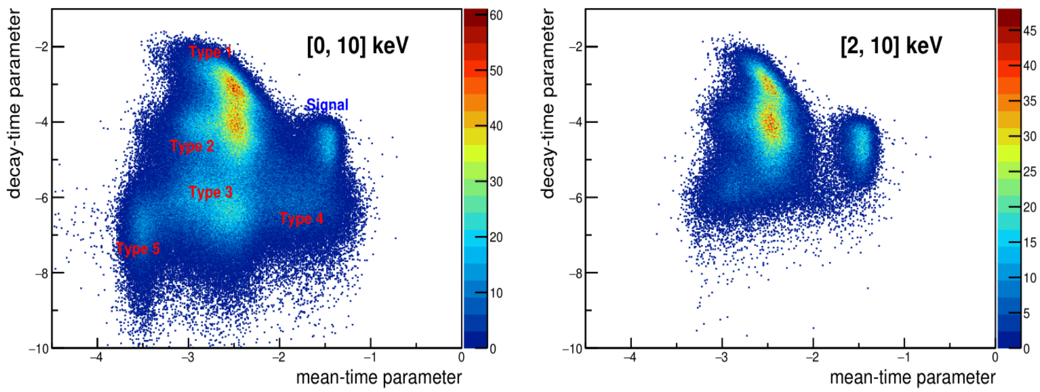

Figure 4.4 Meantime vs decay time parameter distribution. The left (right) panel shows the distribution with the range of 0(2) to 10 keV.

The 2-D plot of mean and decay time as shown in figure 4.4. There are 5 types of the event categories. Type 4 and 5 as well as majority of the type 3 cannot seen in figure 4.4 (b), so they are distributed from 0 to 2 keV.

Especially the type 4 noise is difficult to separate from signal below 2 keV. The accumulated pulse of physical events has broadest shape compared with pulse shape of PMT noises. Types which can be separated via decay-time parameter such as type 3, 4 and 5 has common characteristic that the pulse shape has higher tail than other type of PMT noises. On the contrary, the pulse shape of type 1 which has large values of decay-time parameter has lower tail. The PMT noises which has pulse shape with high tail can have larger values of mean-time parameter than that of low tail, and it is the reason why we cannot separate the physical events from PMT noises in low energies region via mean-time parameter only.

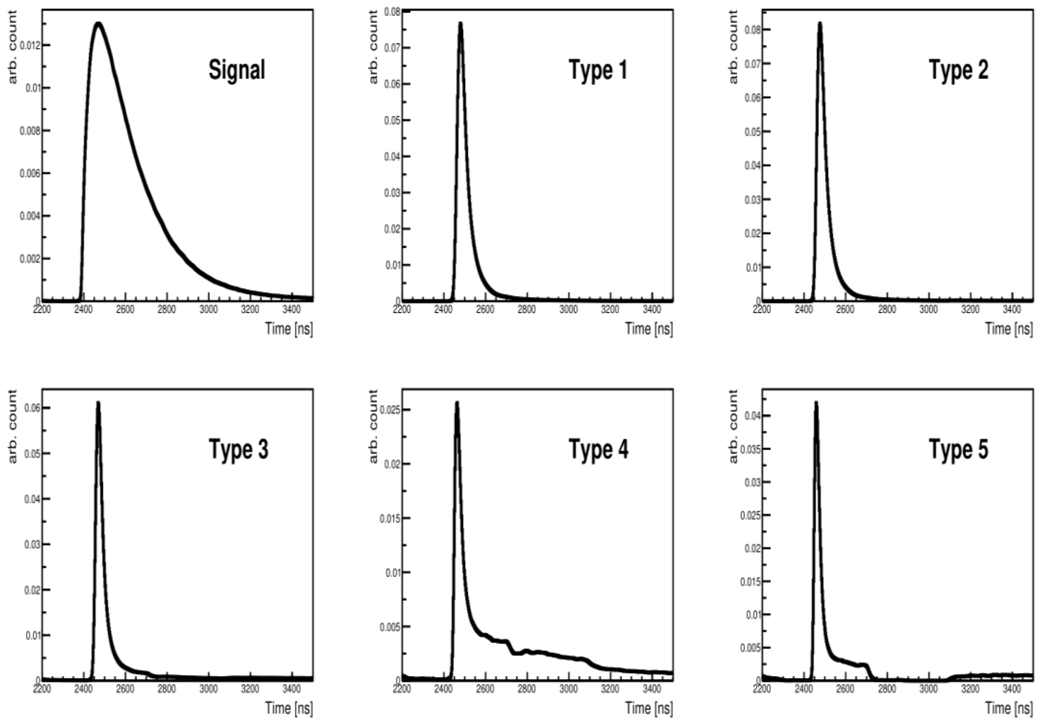

Figure 4.5 Accumulated waveforms categorized in figure 4.4. The waveforms of type 3, 4 and 5, which have small value of decay-time parameter, shows long tail. The events below 10 keV in the normal-background data is used for noise waveforms and the events with the range of 2 to 10 keV in the ^{60}Co calibration data is used for signal waveform.

4.1.3 likelihood parameter

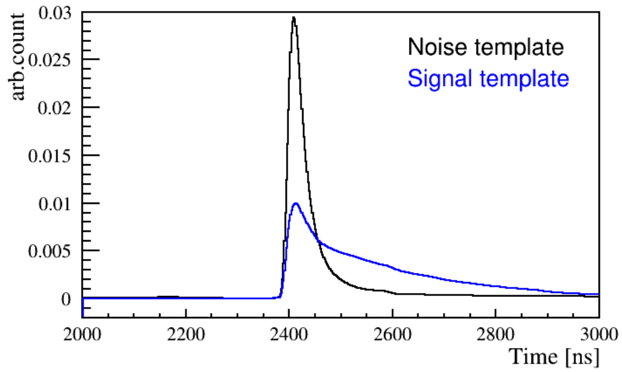

Figure 4.6 Accumulated waveforms using normal background run for noise template and coincidence events from ^{60}Co calibration run for signal template.

The development of the decay-time parameter gives a better separation power for event selection at low energies, but it still has several limits. The PMT pulse should be divided into the first half (head) and the second half (tail) for the calculation, so both of two PMT pulses for each crystal should have two or more peaks. It will be critical issue for low energy region. The second is the significance of correlation between mean and decay time parameters to estimate the selection efficiency. We should set one (or more) criteria for event selection in 2-D parameter space and it means that the different modeling for physical events and PMT noises is needed to estimate the efficiency. The correlation between two parameters can affect the efficiency and the modeling considered the correlation is not easy without bias. Thus, 1-D parametrization using mean and decay time parameters are developed.

The pure physical events is collected from events that are coincident for one of the crystals (multiple hit) in the calibration data of ^{60}Co which is taken about a month to collect the Compton scattered low energy events. The signal reference waveform is prepared by using the 60Co multiple hit events using meantime vs decay time parameter space. In order to construct noise template waveform, the PMT noise events are selected via criteria of both parameters, from all events in the normal background data. The two reference waveforms are distinctly different as shown in figure 4.6 and a logarithmic likelihood of waveform summed two PMT pulses for each event can be calculated with each reference waveform. There are two logarithmic likelihoods for a crystal due to two reference waveforms, the signal and the noise. In order to construct a parameter from 2 logarithmic likelihoods, the score is given as,

$$P_{l,i} = \frac{ln\mathcal{L}_n - ln\mathcal{L}_s}{ln\,\mathcal{L}_n + ln\mathcal{L}_s} \qquad (4.4)$$

where $p_{l,i}$ is the likelihood parameter of crystal i. The lnL_s and lnL_n denote logarithmic likelihoods obtained with signal and noise references, respectively. The likelihood parameter for ^{60}Co calibration run is as shown in figure 4.7. The upper and lower band denote the physical events and the PMT noises, respectively, and the likelihood parameter has better separation power in the energy range of 1 to 2 keV than mean-time parameter.

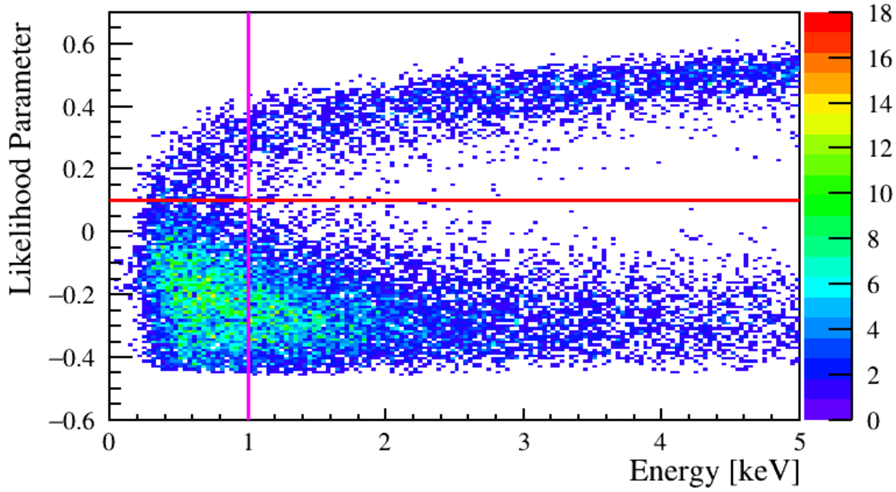

Figure 4.7 Likelihood parameter as a function of the energy for multiple-hit events in the ^{60}Co calibration data. The upper (lower) band corresponds to signal (noise) and red line are used to separate signal and noise events.

4.1.4 Signal sample for BDT training

The newly developed likelihood parameter has power to separate signal and noise up-to 1 keV. The signal like events is used to model the scintillating events over normal background data. The events above the red line in figure 4.7 are selected as pure signal samples and the events between 1.0 to ~1.5 keV is modelled to estimate the purity of signal sample and found to be more than 99 % level. These pure signal samples are used as a signal model and first 59.5 days of the normal-background data which contains large amount of the PMT noise like events which are used as a noise sample to train the BDT. The BDT weights as a function of energy of the normal background data is shown in figure 4.8 which shows good separation between scintillation signals and PMT noises above 1 keV. The events right to red line is selected as a signal-like events.

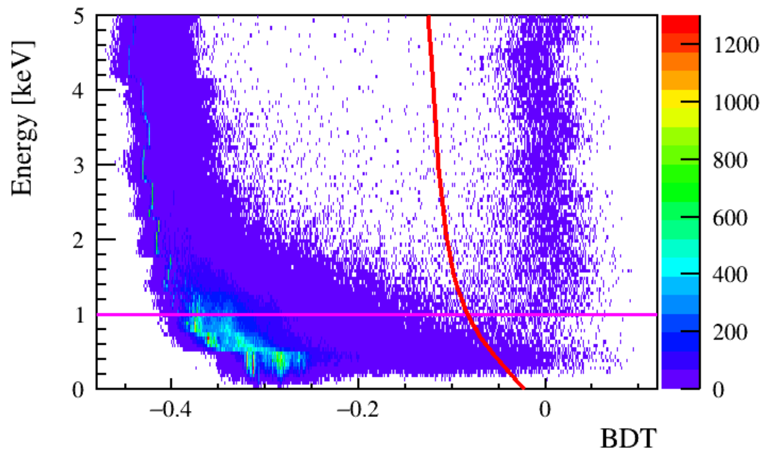

Figure 4.8 BDT weight as a function of the energy for normal background run using set 1 data and red line are used to select signal and noise events.

4.1.5 BDT output validation

Trained BDT weights have a good separation power in background data but the validation of BDT and quantifying the selection efficiency is mandatory before getting the final background spectrum. In order to validate the BDT weighting process, a comparative study between independent samples is performed. The signal samples from ^{60}Co calibration data and the signal-like events selected from the background data after the BDT selection are used as an independent sample. However, the spectrum of ^{60}Co calibration data is not the same as the background data, so ^{60}Co spectrum is reweighted to match the background spectrum for comparison, where weight is calculated based on the modelled background spectrum using total simulation of the background data as shown in figure 4.9.

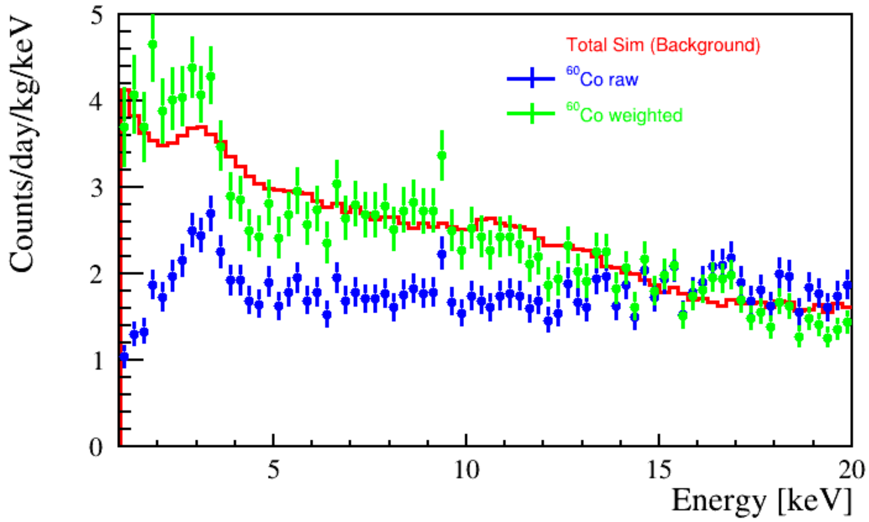

Figure 4.9 Energy spectrum of the ^{60}Co multiple hit events before (after) reweighting blue(green) in Crystal 4 based on the total modelled simulated spectrum (red) using background data.

Figure 4.9 show the weighted spectrum from the ^{60}Co calibration data and the weights are applied to all selection variables made from ^{60}Co samples to compare with the background data. After weighting, there is a good agreement for variables between two independent samples as shown in figure 4.10 which confirms the BDT weighting process. The degree of consistency between those two samples is used as a validation tool.

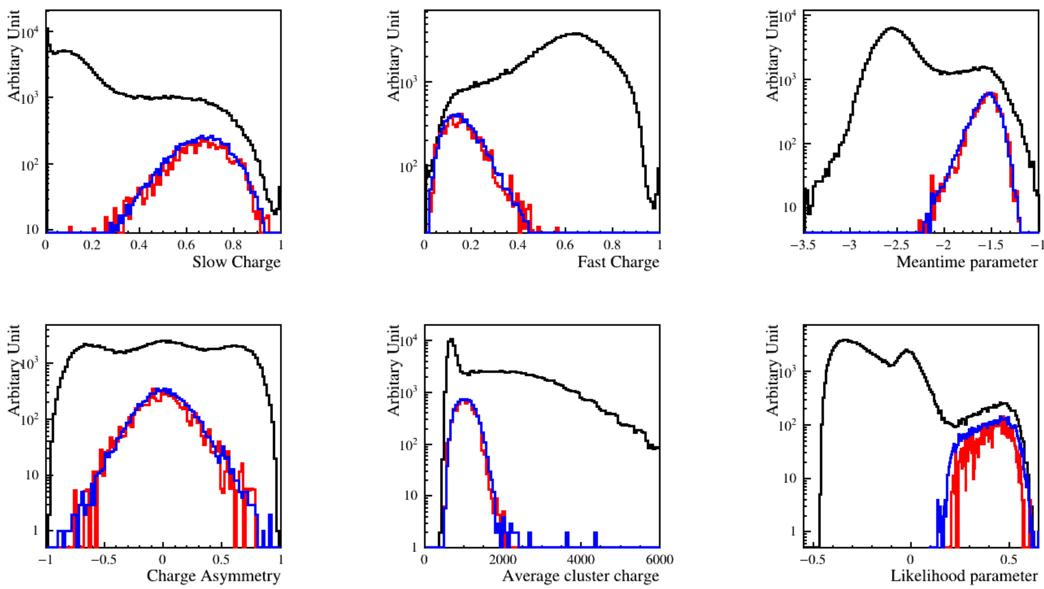

Figure 4.10 Some example variables studied to validate the BDT output response. The black, red and blue distributions are the total background, ^{60}Co coincident events and signal-like events from the background data, respectively. All variables are weighted as shown in figure 4.9.

4.2 Event selection

New set of event selection to reach 1 keV analysis threshold is developed for set 2 data. The precut as discussed in the section 3.3.1 is revised for this analysis because tight precut can remove the physical events near the threshold region. The trigger position of the triggered event is around 2.4 μs within the 8 μs time window and each event are reconstructed using clustering algorithm to extract the single photoelectron above the pedestal. Local maximum point between each successive ADC bins is found to form isolated cluster. In the case where two local maximums are found in a cluster, the separation between neighboring cluster is obtained by finding local minimum points between two single photoelectrons. The coincident events with muon detector (MuonTotalDeltaT0) within the 30 ms are removed as a flasher event. Generally, tails of such events give pre-pulse before the trigger time in coincidence window. There is a category of precut which can remove the PMTS dark current comes with a constraint that the number of clusters (nc) for each PMT should be greater or equal to one.

The second cluster time (t_1) of each PMTs should be greater than zero to remove any possible garbage type of events passed via the clustering algorithm. The negative charge cut (rqcn) of the crystal should be greater than -1 which is effective to remove oscillation noise typically coming from any electric related work near to the detector room.

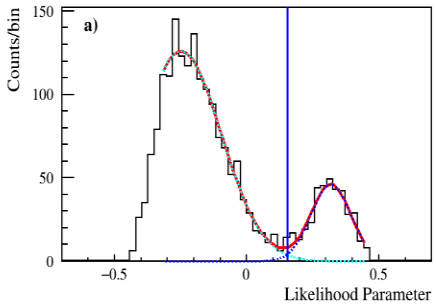

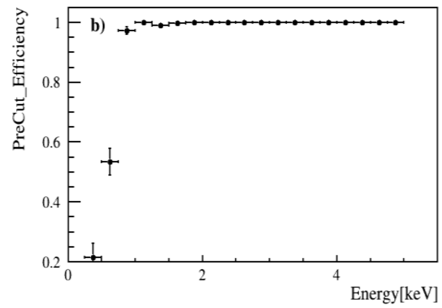

Figure 4.11 Signal sample selection efficiency estimation A) The likelihood parameter from ^{60}Co multiple hit events between 1 to 1.25 keV. The events right to the blue line is used for BDT training B) The signal sample selection efficiency for C6

This precut is applied to the calibration data to collect the pure scintillating signal sample for BDT training. To ensure the selection of the signal sample, its efficiency is estimated as shown in figure 4.11 (a). The likelihood parameter for each 0.25 keV events are modelled by using the Gaussian plus asymmetry Gaussian distribution and obtained the precut efficiency. Precut efficiency for all crystal is more than 98 % at 1 keV.

In 2 keV analysis threshold study, straight line cut for BDT is used as a final event selection. However, signal/noise separation is energy dependent and this is a quite risk while looking for nuclear recoil analysis. So, energy dependent function (which is the convolution of the linear and exponential function) is used to select the signal events as shown in figure 4.12.

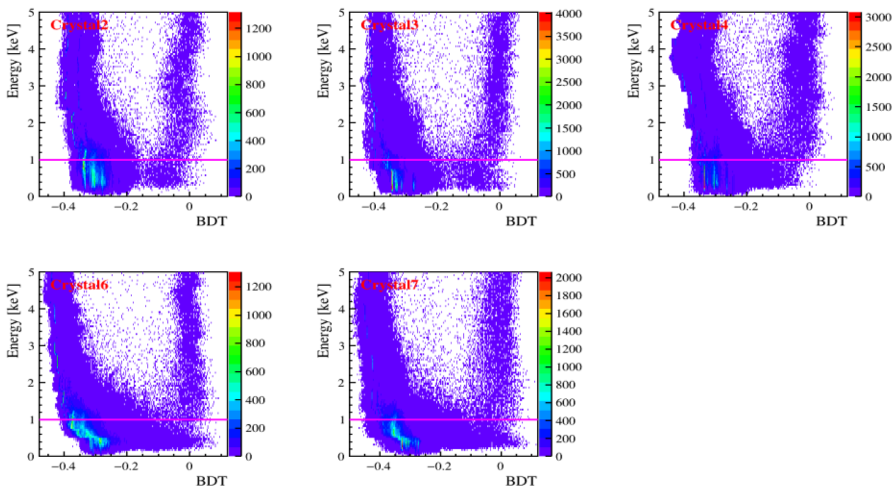

Figure 4.12 Energy versus BDT parameter for all crystals using set1 background run. Each panel corresponds to different crystals.

The BDT selection is optimized by using the 1 to 1.5 keV events from set1 background data. The BDT parameter is modeled with the convolution of asymmetry Gaussian (cyan color) for noise like events and single Gaussian (magenta color) for signal like events as shown in figure 4.13. The selection is optimized so that the purity of the signal (signal to noise ratio) should be more than 99 % level. The red color spectrum in figure 4.13 is after selecting the energy dependent BDT cut as shown by red line in figure 4.12.

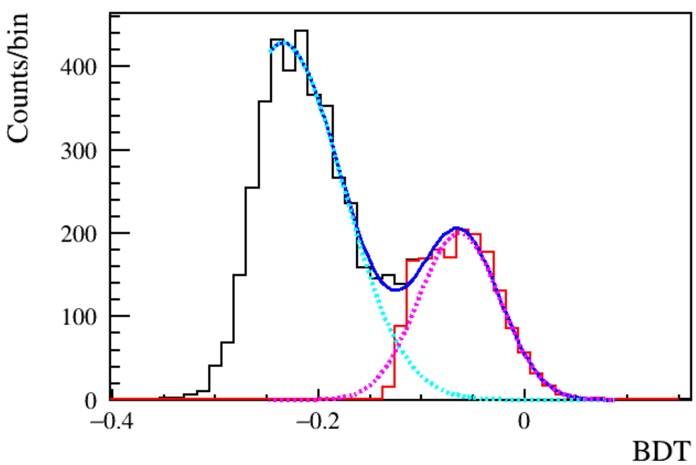

Figure 4.13 The BDT distribution of between 1 to 1.5 keV single hit events from set1 background data. The red histogram is signal events after bdt cut and dotted cyan and magenta model function is used to estimate the purity of the signal selection and found to be 99.38%.

Crystal by crystal event selection is optimized and their selection efficiency is estimated by using ^{60}Co multiple events. The ratio of the events which passed over signal selection to the total events is the signal efficiency. The signal selection efficiency for each crystal is estimated as shown in figure 4.14 and achieved to be more than 70 %.

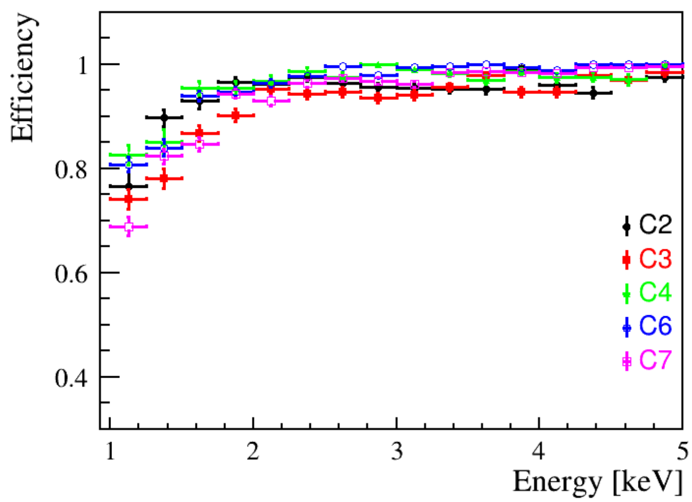

Figure 4.14 Event selection efficiency for all crystal estimated with ^{60}Co multiple hit events for each 0.25 keV bin.

An independent test bench which is feasible to study the nuclear recoil (NR) events is used to cross-check the stability of the selection criteria and efficiency estimation. A small ($2 \times 2 \times 1.5$ cm^3) NaI(Tl) crystal which is taken from the same ingot of Crystal 2 is installed at neutron generator facility in Korea Research Institute of Standards and Science (KRISS) [90]. Mono-energetic neutrons were produced by deuteron-deuteron nuclear fusion reaction using a DD109 neutron generator and measured to be 2.43 ± 0.03 MeV. Such high energy neutrons scatter from the crystal and produce nuclear recoils at low energy. BC501A liquid scintillation detectors are used to tag the neutron scattered events from NaI(Tl) crystal. The energy vs BDT of three independent samples are compared into the figure 4.15(a). Same event selection which was used for COSINE Crystal 2 is used to estimate electron and nuclear recoil efficiency. The efficiency among two independent electron recoil (ER) samples and one nuclear recoil sample are consistent within statistical fluctuation over same event selection as shown in figure 4.15(b). This illustrate the stability of event selection efficiency in the region of NR search.

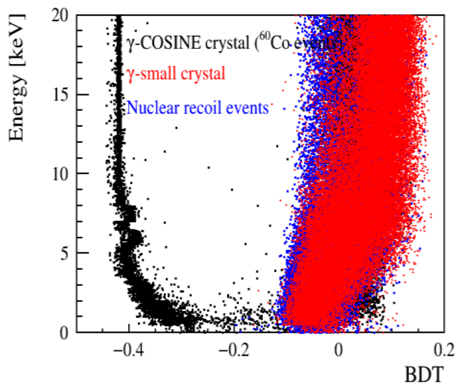

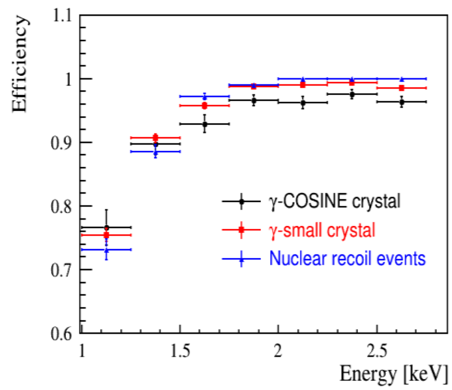

Figure 4.15 BDT performance of the independent sample a) The small size crystal's ER and NR are overlaid over COSINE ER data. b) Efficiency comparison between independent measurements.

The efficiency is modelled with an error function,

$$ErrFunction = ErF(p[0] + p[1]x) \qquad (4.5)$$

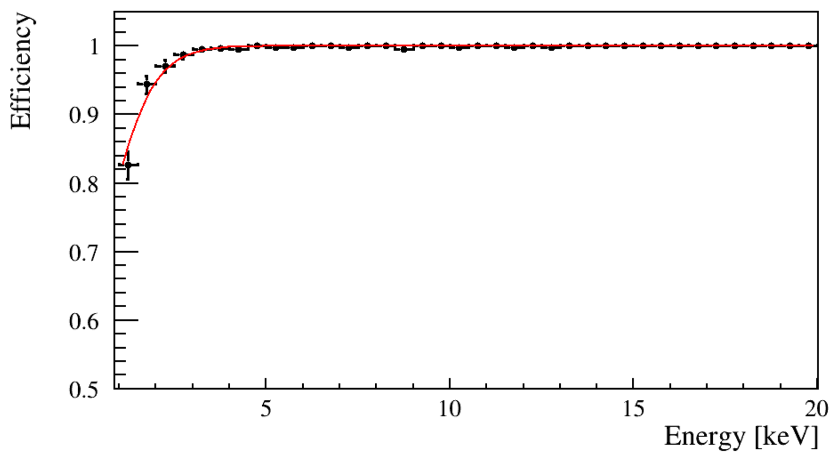

Figure 4.16 Efficiency modelling by using the error function. First order error function (red) is used to model the efficiency.

4.2.1 Background data

The set 2 data having 97.7 kg.year exposure is used for background understanding. The good run data list which was used for annual modulation analysis is used to make the final background spectrum. The event selection discussed in the section 4.2 is used to select the signal events and modelled efficiency function is used to get the final efficiency corrected spectrum.

The single hit low energy spectrum in our ROI from different crystals are shown in figure 4.17. The spectrum above 2 keV is well reproduced with new BDT weight and selection criteria while comparing the 2 keV analysis threshold study. This improved event selection doesn't require any additional second level of BDT (BDTA in 2 keV threshold study) for good run list. In general, most of the crystal's background is increasing between 1 to 2 keV. This will be discussed in next section of the background modelling.

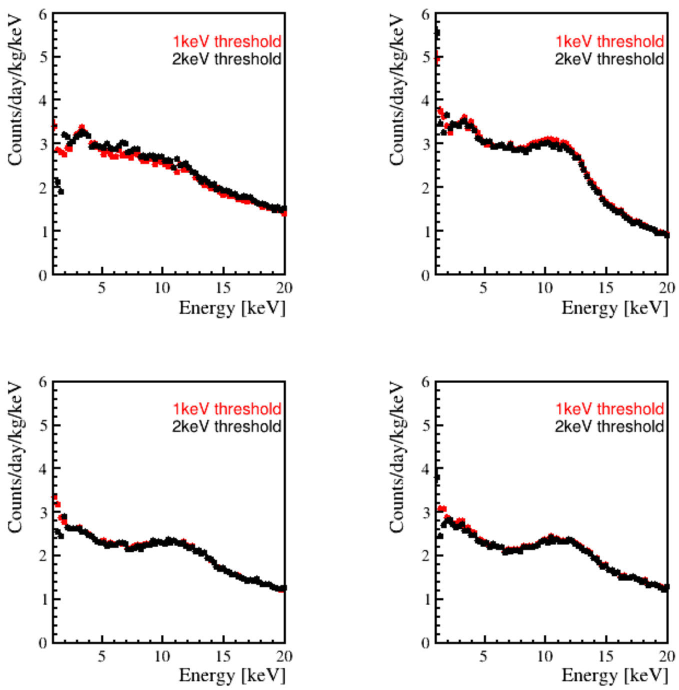

Figure 4.17 Efficiency corrected background spectrum using set 2 data between 1-20 keV. The black (red) energy spectrum after applying the event selection developed for 2(1) keV threshold analysis.

4.3 Background understanding for WIMP search data

Background understanding is crucial for rare event search. Geant4 based MC is used to model the background data. COSINE-100 used set1 data with 2 keV analysis threshold in previous round of background modeling [86]. An improved background modeling with set2 data is performed for this round of physics analysis with large exposure and lower threshold. The details of the background modeling procedure along with its quantitative estimation to ROI is discussed into this section.

4.3.1 Background modeling method

The COSINE-100 is using an array of 106 kg of low-background NaI(Tl) detectors submerged in a veto counter with 2 tons of liquid scintillator. The geometry of the experimental setup is well explained in the ref [86]. The Geant4 improved their toolkit and updated it to the Geant4 4.10.4.p2 [91]. This Geant4 version is one of the major systematics while modeling the set 1 data. So, careful study about the version difference is carried out for this study.

The full decay chains of the radioisotope's nuclei like ^{238}U, ^{232}Th and ^{235}U are break into 5, 3 and 2 groups of daughter isotopes respectively based on their half-life period as shown in table 4.1. The events are simulated with COSINE simulation framework and reconstructed after smearing the resolution which is calculated as discussed into section 3.1.3. Total MC is divided into four channels for each crystal (low energy single and multiple hit, high energy single and multiple hit) to make compatible with the data. If any events deposit energy to the target single crystal, then it is considered as single hit but if it deposits energy to more than one crystal or LS energy less than 80 keV, then it is considered as multiple hit. Figure 4.18 shows the deposited energy to one of the COSINE crystals using different Geant4 version and fitted with the proper function. Parameter p3 in figure 4.18 (a) give the mean energy corresponding to ^{40}K events and parameter p4 in figure 4.18 (b) give the mean energy corresponding to the ^{210}Pb.

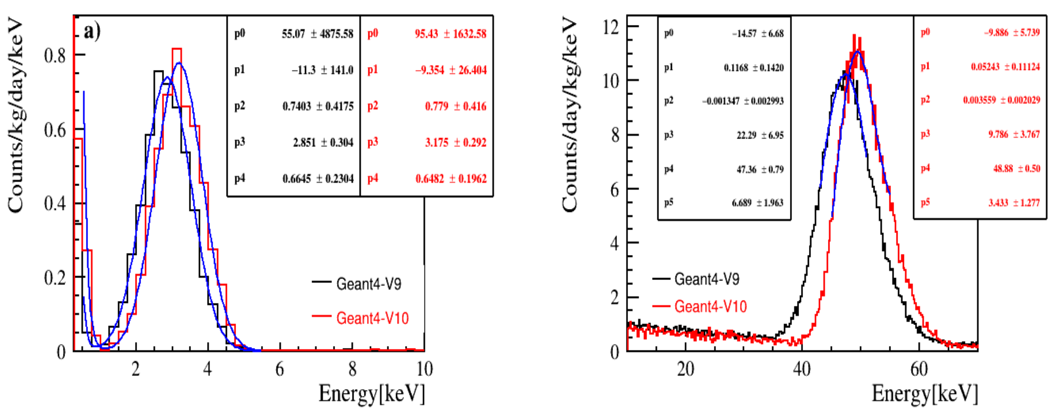

Figure 4.18 The resolution smeared simulated spectrum generated by two different Geant4 version 4.9.6.p02 (black) and 4.10.4.p2 (red). The peak position of each isotopes is reasonably simulated in Geant4 version 4.10.4.p2 package

Table 4.2: Chain-breaking groups for ^{238}U, ^{235}U and ^{232}Th

G:	DC	DM	HL	G:	DC	DM	HL	G:	DC	DM	HL
G-11	^{238}U-^{234}Th	α	4.8E9y	G-21	^{232}Th-^{228}Ra	α	1.40E10y	G-41	^{235}U-^{231}Th	α	7.04E8y
	^{234}U-234Pa	β-	24.1d	G-22	^{228}Ra-^{228}Ac	β-	5.75y		^{231}Th-^{231}Pa	β-	25.52h
	^{234}Pa-^{234}U-	β-	6.7hr		^{228}Ac-^{228}Th	β-	6.15y		^{231}Pa-^{227}Ac	α	3.3E4y
G-12	^{234}U-^{230}Th	α	2.5E5y	G-23	^{228}Th-^{224}Ra	α	1.91y	G-42	^{227}Ac-^{227}Th	β-	21.77y
G-13	^{230}Th-^{226}Ra	α	7.5E4		^{224}Ra-^{220}Rn	α	3.63d		^{227}Th-^{223}Ra	α	18.7d
G-14	^{226}Ra-^{222}Rn	α	1.6E3y		^{220}Rn-^{216}Po	α	55.6s		^{227}Fr-^{223}Ra	β-	21.8s
	^{222}Rn-^{218}Po	α	3.8d		^{216}Po-^{212}Pb	α	0.145s		^{223}Ra-^{219}Rn	α	11.4s
	^{218}Po-^{214}Pb	α	3.1m		^{212}Pb-^{212}Bi	β-	10.6h		^{219}At-^{215}Bi	α	56s
	^{214}Pb-^{214}Bi	β-	26.8m		^{212}Bi-^{212}Po	β-	66.6m		^{219}Rn-^{215}Po	α	3.96s
	^{214}Bi-^{214}Po	β-	19.9m		^{212}Po-^{208}Pb	α	2.99E-7s		^{215}Bi-^{215}Po	β-	7.6min
	^{214}Po-^{210}Pb	α	1.6E-6s		^{212}Bi-^{208}Tl	α	60.6m		^{215}Po-^{211}Pb	α	1.78ms
G-15	^{210}Pb-^{210}Bi	β-	22.2y		^{208}Tl-^{208}Pb	β-	3.05m		^{211}Pb-^{211}Bi	β-	36.1m
	^{210}Bi-^{210}Po	β-	5d	**G: Group, DC: Decay Chain, HL: Half Life**					^{211}Bi-^{207}Tl	α	2.14m
	^{210}Po-^{206}Pb	α	138d						^{211}Po-^{207}Pb	α	516ms
									^{207}Tl-^{207}Pb	β-	4.77min

The ^{40}K coincident events should deposit 3.2 keV on the target crystal following the electron capture decay from K-shell. The ^{210}Pb isotopes should deposit around 50 keV which is the composite peak contributed from conversion electrons, Auger electrons, and X-rays, followed by beta electrons from the decay to ^{210}Bi. All the isotopes which are used for set1 modeling is studied between two version and Geant version 4.10.4.p2 [91] is reasonably simulated in terms of energy scale and their shape. So, COSINE-100 switched its Geant4 MC toolkit from version 4.9.6.p02 to version of 4.10.4.p2.

The low energy range is fixed between 0 keV to 70 keV and high energy range is fixed between 70 keV to 3000 keV. This is the optimized range for WIMP search background data set. The four channels (low energy single and multiple hit with 0.25 keV binsize, high energy single and multiple hit with 2 keV binsize) simultaneous fitter is used for background modeling. Since signal region for WIMP search is below 6 keV, so lower bound for fitting the single hit is 6 keV while multiple hit is 1 keV and upper bound for both single and multiple is 3000 keV. The resolution for low and high energy is treated independently. The measured components typically internal are constrained within their uncertainties while any unknown component like external or cosmogonic or surface are freely floated in this fitting method. The four-channel likelihood fit as given by equation 4.6 is used to model the set2 data.

$$\mathcal{L} = \prod_{i}^{N_{ch}} \prod_{j}^{N_{bin}} \frac{\mu_{ij}^{n_{ij}} e^{-\mu_{ij}}}{n_{ij}!} \prod_{k}^{N_{bkg}} e^{-\frac{(x_k - a_k)^2}{2\sigma_k^2}} \tag{4.6}$$

where N_{ch} is the number of channels, N_{bin} is the number of bins in each histogram, N_{bkg} is the number of background components, n_{ij} is the number of observed counts, μ_{ij} is the total model expectation by summing all N_{bkg} background components in the product of Gaussians, x_k is the value of the k^{th} background component, α_k is the mean value and σ_k is its 68 % uncertainty.

4.3.2 Sources of the background

The different background isotopes originated from the crystal itself (internal), PMTs, acrylic supporter and copper housing used in encapsulation (external), and cosmogonic components which was used in set1 [86] modeling is also considered as a source of the background to model set2 data. Set2 modeling is improved after considering several additional components as well as surface profiling for ^{210}Pb component.

The radioactive contamination is estimated by using the set2 data as shown in table 4.2 where the activities of ^{40}K and ^{238}U are used from the ref [57]. ^{238}U background can't be estimated by using BiPo coincidence technique [74] because of the 1ms dead time and ^{40}K is assumed to be in similar level because of its longer half-life. This measurement is the constrains for log-likelihood fitter.

The Iodine isotopes are the one of the probable candidate to be present in the NaI(Tl) crystal. ^{129}I is a cosmogonic element produced by spontaneous fission of the uranium and cosmic rays. It is a β-decay going to the excited-level of ^{129}Xe at 39.57 keV and half-life of 16.1 ×

10^6 years. The simulated spectral shape of the ^{129}I in one of the COSINE-100 crystal is as shown in figure 4.19 (b). The distribution follows the sharp rise around 40 keV due to de-excitation of 39.6 keV gamma and a continuum beta line with an end point of 194 keV. The background modeling after adding the ^{129}I is as shown in figure 4.19 (b). This shows an improvement in the modeling between 40 to 70 keV.

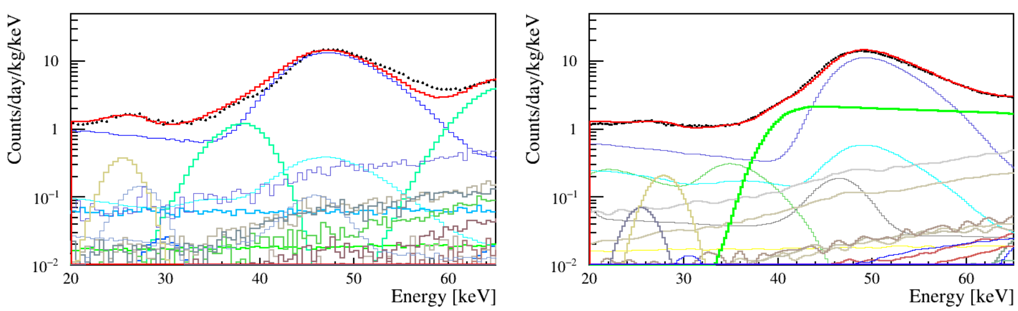

Figure 4.19 Background modeling for low energy single hit events for C6 a) Set1 background model w/o ^{129}I cosmogonic components b) background modeling w/ ^{129}I cosmogonic components. The thick green line corresponds to ^{129}I isotopes.

^{210}Pb is one of the dominant component in our ROI and we have been found that the spectral shape of the β-decay events at low energy varies with the depth of the NaI(Tl) crystal surface [92]. So, depth profile is scanned by using an independent measurement. This knowledge is used to scan the ^{210}Pb profiling for COSINE crystal's surface.

A small size crystal of 1.28 kg from the same ingot of C6 and C7 is used to measure the ^{210}Pb surface profiling. This crystal is cut in two pieces, and surface of one of the pieces of the crystal is exposed to the ^{222}Rn source for two weeks which contaminate the crystal. These pieces were attached facing each-other and a 4 μm thin mylar film is inserted between them to prevent cross-talk of the scintillation light as shown in figure 4.20. The detector is installed at R&D set-up (A6) and taken data for 70 days.

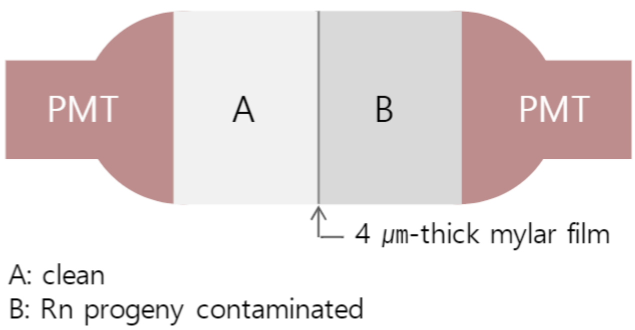

Figure 4.20 The schematic view of the detector used to measure the 210Pb depth profiling.

The surface alpha decay events from ^{210}Pb to ^{206}Pb is modeled by using Geant4 simulation assuming that the depth distribution would be exponential followed by the equation 4.7. The best fit result from alpha modeling is shown in figure 4.21. The best fit value for slope component is found to be 2.06 $\pm$ 0.12 μm using log-likelihood method.

$$Par0 \times Exp\left(\frac{Par1}{Depth(\mu m)}\right) \tag{4.7}$$

where Par0 is the offset and Par1 is the slope of the ^{210}Pb distribution.

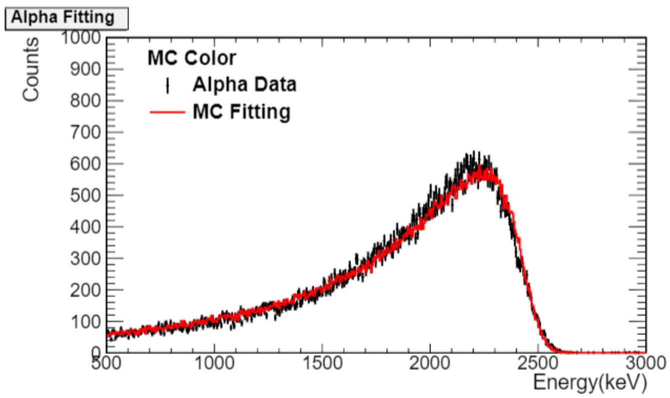

Figure 4.21 The surface alpha events from R&D setup (black) modelled with simulation (red). The best fit slope parameter is found to be 2.06 $\pm$ 0.12 μm.

^{210}Pb isotopes are generated uniformly within 10 μm thickness of the crystal surface and reweighted as shown in figure 4.22 (a) by using the best fit slope values obtained from the measurement. The energy spectrum from surface ^{210}Pb is reconstructed with an exponential distribution as a function of the depth within crystal surface to get the profiled energy spectrum as shown in figure 4.22 (b). This gives a better and more realistic constrain for ^{210}Pb surface contribution and its uncertainties are treated as one of systematics for the physics analyses. The inclusion of the ^{210}Pb surface profile is addressed to get better modeling at low energy.

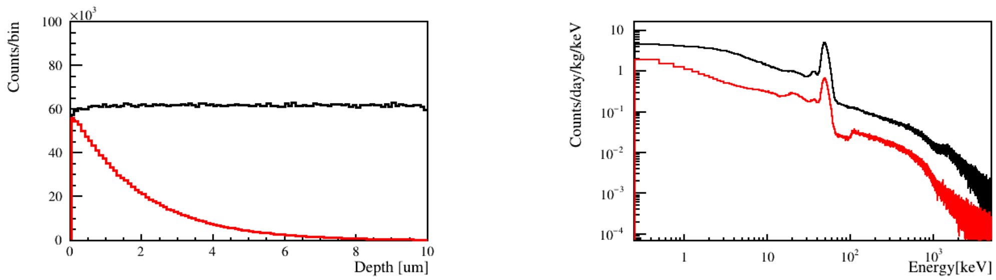

Figure 4.22 The ^{210}Pb surface optimization for C6 with the exponential model a) depth of the generated (black) and reconstructed (red) events b) energy distribution of the generated (black) and reconstructed (red) events.

The region from 150 to 250 keV and above ~2500 keV isn't reproduced by simulations. Additional ^{235}U from the PMTs after chain-breaking as shown in table 4.1 improved this mismatching around 200 keV. The energy above 2500 keV is modeling in multiple hit while mismodeling in single hit indicate that, there could be some unknown external components originated far away from the detector. The inclusion of the ^{208}Tl monoenergetic gamma from the copper shield improved the modeling. The considered assumptions are essential to improve the overall agreement with measured data.

4.3.3 Background modeling for set2 data

All the assumptions discussed into the section 4.3.1 is incorporated on the top of the known hypothesis which was used in set1 modeling. There are 55 different components including

Table 4.3: The major dominant component and their corresponding energy

Isotopes	Single Hit Energy(keV)	Remarks	Isotopes	Multiple Hit Energy(keV)	Remarks
^{210}Pb	~10	Teflon, X-ray	^{40}K	~3.2	Internal, X-rays
^{109}Cd	~25	Cosmogenic, Binding energy of Ag K-shell electrons	^{121m}Te	~30	Cosmogenic, Electron capture
^{210}Pb	~50	Internal, γ-ray, X-rays,, auger electron	^{22}Na	~511	Cosmogenic, γ-rays
^{125}I	~67	31.7 keV X-rays and Auger electrons to a 35.5 keV excited state	^{214}Bi	~609	External, γ-ray
^{212}Pb+^{214} Pb	~240	External, γ-ray	^{214}Bi	~1120	External, γ-ray
^{214}Pb	~295	Externa, γ-ray	^{232}Th	~2610	External, γ-ray
^{214}Pb	~350	External, γ-ray			
^{214}Bi	~609	External, γ-ray			
^{234}Pa	~920	External, γ-ray			
^{40}K	~1460	External, γ-ray			
^{214}Bi	~1760	External, γ-ray			
^{214}Bi	~2220	External, γ-ray			
^{208}Tl	~2615	External, γ-ray			

internal, external and surface components that are used in this background understanding as shown in table 4.3. Out of these 55 components, 33 components are contributed to reproduce the data by using the four channels simultaneous log-likelihood method as discussed in section 4.3. The next couple of the pages from figure 4.23 to 4.27 shows the comparison between set2 data and MC for five crystals which are considered for this analysis. In general, an improved background modeling based on Geant4 based simulation reproduces the background data and gives a better understanding of the detector's background.

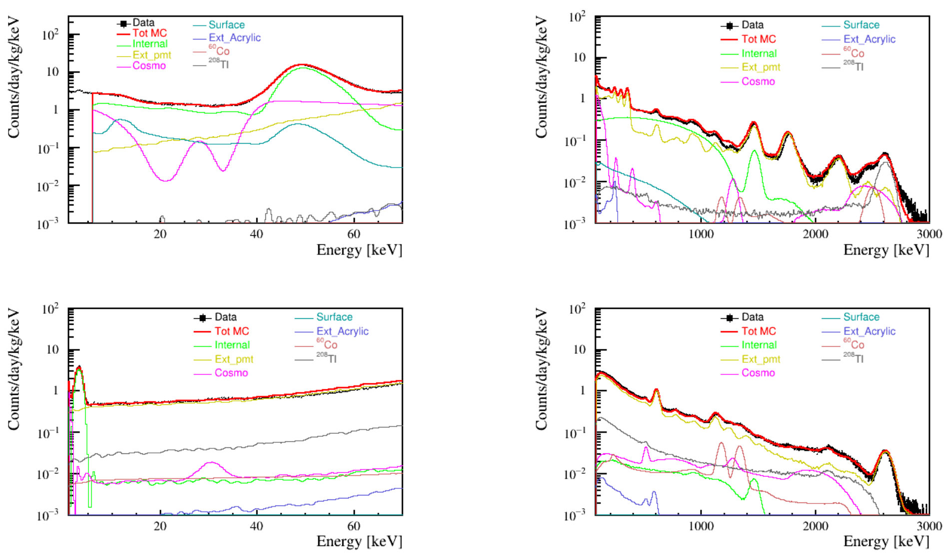

Figure 4.23 The single hit (top) and multiple hit (bottom) with high gain (left) and low gain (right) background energy spectrum fitted with MC simulation for Crystal-2.

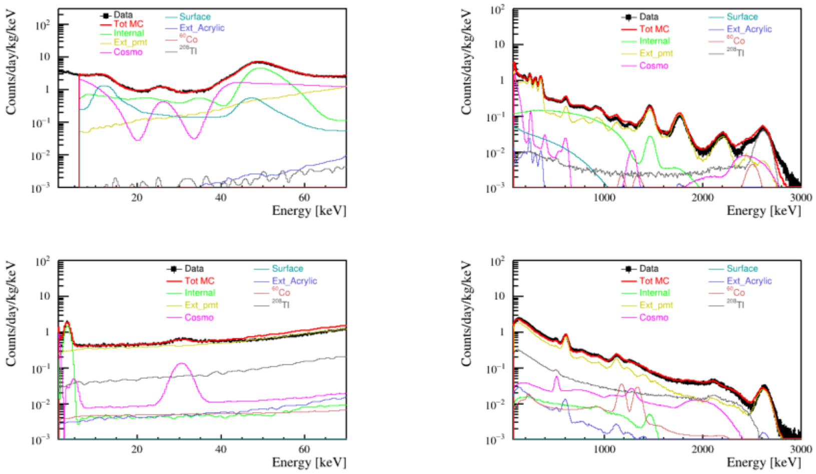

Figure 4.24 The single hit (top) and multiple hit (bottom) with high gain (left) and low gain (right) background energy spectrum fitted with MC simulation for Crystal-3.

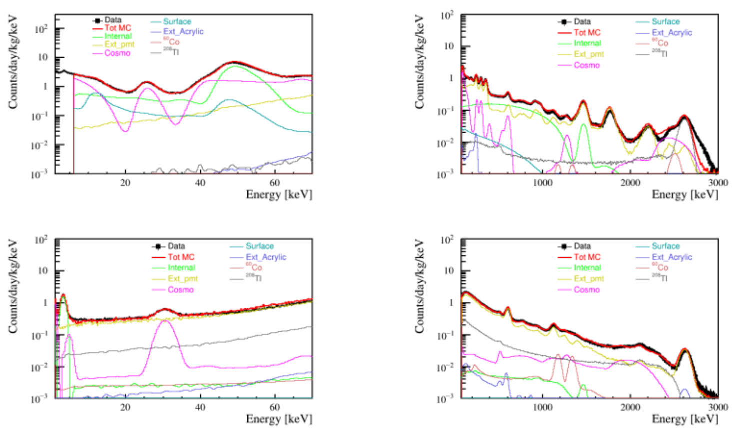

Figure 4.25 The single hit (top) and multiple hit (bottom) with high gain (left) and low gain (right) background energy spectrum fitted with MC simulation for Crystal-4.

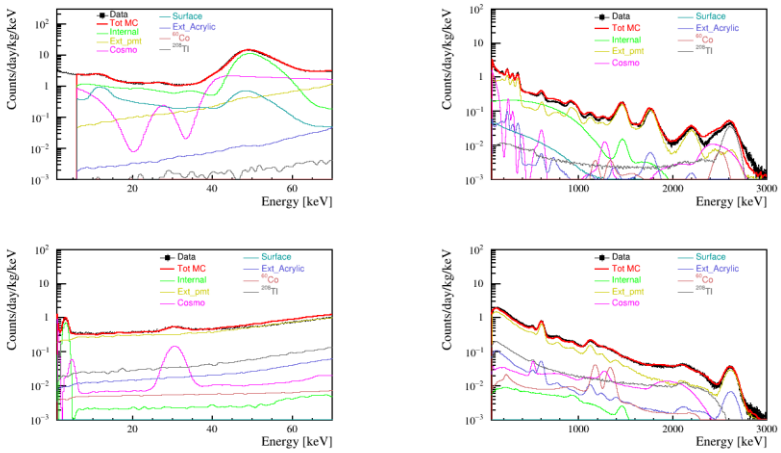

Figure 4.26 The single hit (top) and multiple hit (bottom) with high gain (left) and low gain (right) background energy spectrum fitted with MC simulation for Crystal-6.

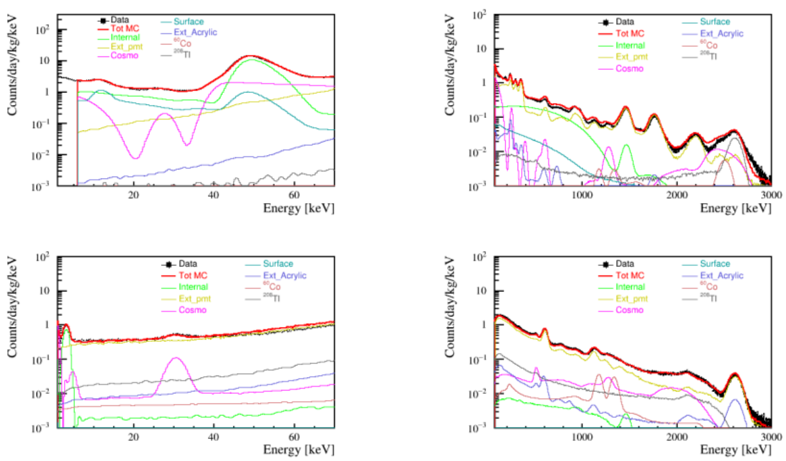

Figure 4.27 The single hit (top) and multiple hit (bottom) with high gain (left) and low gain (right) background energy spectrum fitted with MC simulation for Crystal-7.

The major components and their corresponding mean energy is summarized in table 4.3. The background activities of the dominant components calculated from this background modeling method are also summarized in this table 4.4. Among these five crystals, Crystal 2 have the longest cooling time that's why short-lived cosmogenic components were already decayed away. The Crystal 4, Crystal 6 and Crystal 7 have the least cooling time so that short-lived cosmogenic isotopes are pronounced in this crystals. So, the cosmogenic contributions are the crystal dependence based on the deployed history of the crystals. The radio purity of the crystals depends on the powder grade as well as growing condition. Powder-C is relatively poorer grade powder in comparison with the WIMP-Scint II and III. Crystal 2 was grown from powder C so it has larger internal background (typically ^{40}K and ^{210}Pb). Crystal 3 and 4 are grown from WIMP-Scint II which has the least ^{210}Pb but higher ^{40}K. The least ^{40}K background is found from WIMP-Scint III, unfortunately higher ^{210}Pb from WIMP-Scint III crystal like in Crystal 6 and Crystal 7. The overall background components for Crystal 6 and Crystal 7 are similar because they are same ingot crystal. The dominant peaks are summarized in the following table 4.3.

Background assessment is compared with set 1 fitted result as shown in figure 4.28. Since set1 used initial ~2 months data while set2 used initial 1.7 years data. So, significant background reduction is observed for short-lived components like ^{125}I, ^{109}Cd and ^{22}Na while long-lived isotopes like ^{40}K, ^{3}H are consistent between two modelled values. The comparison between these independent methods validate the fitted result.

Table:4.4 Background assessment of dominant component for COSINE 100

Isotopes	Source position	Fitted Activities				
		Crystal-2	Crystal-3	Crystal-4	Crystal-6	Crystal-7
^{238}U-1	Crystal's Bulk	0.0025±0.000001	0.0025±0.000001	0.0003±0.000004	0.00025±0.000007	0.00025±0.000002
^{232}Th-2		0.0022±0.0009	0.00221±0.003	0.002±0.0008	0.003±0.001	0.003±0.001
^{232}Th-3		0.0025±0.0004	0.00025±0.0009	0.0003±0.0001	0.00025±0.0001	0.0003±0.00005
^{40}K		1.92±0.0058	0.94±0.0047	1.071±0.003	0.43±0.0032	0.51±0.0031
^{210}Pb		1.80±0.0036	0.61±0.0018	0.66±0.0017	1.5±0.0016	1.45±0.0017
^{210}Pb	Crystal Surface	0.55±0.0083	0.4±0.0068	0.37±0.0052	0.88±0.0081	1.32±0.0092
	Bulk PTFE	0.45±0.0072	0.38±0.0023	0.56±0.005	0.75±0.0074	0.86±0.0069
^{60}Co	Copper case	0.56±0.009	0.33±0.0086	0.22±0.0046	0.36±0.0083	0.38±0.0087
^{238}U-1	External	22.6±6.66	22.4±7.8	22.36±3.2	11.4±1.1	22.2±3.4
^{238}U-4	(Crystal attached PMTs)	137.5±0.275	124±0.114	124.6±0.38	120±1.3	132.5±0.2
^{232}Th-2		43.3±0.779	23.6±0.33	47.6±0.333	47.8±0.4	45.4±0.5
^{232}Th-3		23.9±2.414	23.9±0.406	40.8±0.408	40.8±0.53	40.79±0.416
^{40}K		34.1±2.7	57.8±4.4	227.9±6.4	231.7±12.5	275.5±1.3
^{238}U-4	External	150±0.24	149.9±1.199	150±0.35	162.5±0.52	175±0.245

	Other Crystal's PMTs					
^{232}Th-3		48±0.672	48±1.056	47.9±1.006	35.9±1.3	47.9±0.8
^{40}K		294±4.86	296±4.176	286.3±1.718	231.7±1.7	286.7±1.7202
^{125}I	Cosmogenics	0	0	0.046±0009	0.003 ±0.0007	0.002±0.0006
^{121}Te		0.003±0.002	0.034±0.0006	0.013±0	0.012 ±0.0037	0.026±0.0041
^{121m}Te		0	0	0.087±0.0005	0.031 ±0.001	0.010±0.0006
^{123m}Te		0.011±0.0003	0.028±0.0011	0.07±0.0013	0.074 ±0.002	0.060±0.0016
^{125m}Te		0.011±0.0009	0.004±0.0014	0.008±0.0013	0.008 ±0.0009	0.005±0.0009
^{127m}Te		0.036±0.0018	0.086±0.0016	0.086±0.0016	0.00001±0.0009	0.00001±0.0009
^{3}H		0.138±0.0012	0.295±0.0012	0.269±0.0008	0.117±0.004	0.101±0.0011
^{109}Cd		0	0.021±0.0004	0.05±0.0003	0.004±0.0004	0.003±0.0005
^{129}Na		0.36±0.0058	0.38±0.0049	0.43±0.003	0.43±0.0069	0.421±0.0046
^{113}Sn		0.009±0.0003	0.011±0.0003	0.015±0.0002	0.013±0.004	0.012±0.0003
^{129}I		1.207±0.0048	1.16±0.0034	1.145±0.0145	1.5±0.002	1.43±0.0034
^{238}U-4	Acrylic table	0.72±0.0007	299±2.09	0.001±0	216±1.19	15.4±1.047
^{232}Th-3		62.3±0.062	299±0.299	152±0	100.1±1.56	153.7±0.061
^{40}K		0	299±8.97	0.029±0.0046	0.005±0.0003	0.014±0.0001
^{235}U-1	External PMT	0.65±0.0169	0.48±0.0192	2.42±0.043	1.018±0.0068	0.21±0.0082
^{208}Tl	Cu shield	2.3±0.025	3.12±0.025	1.2±0.0072	1.29±0.024	1.14±0.0137

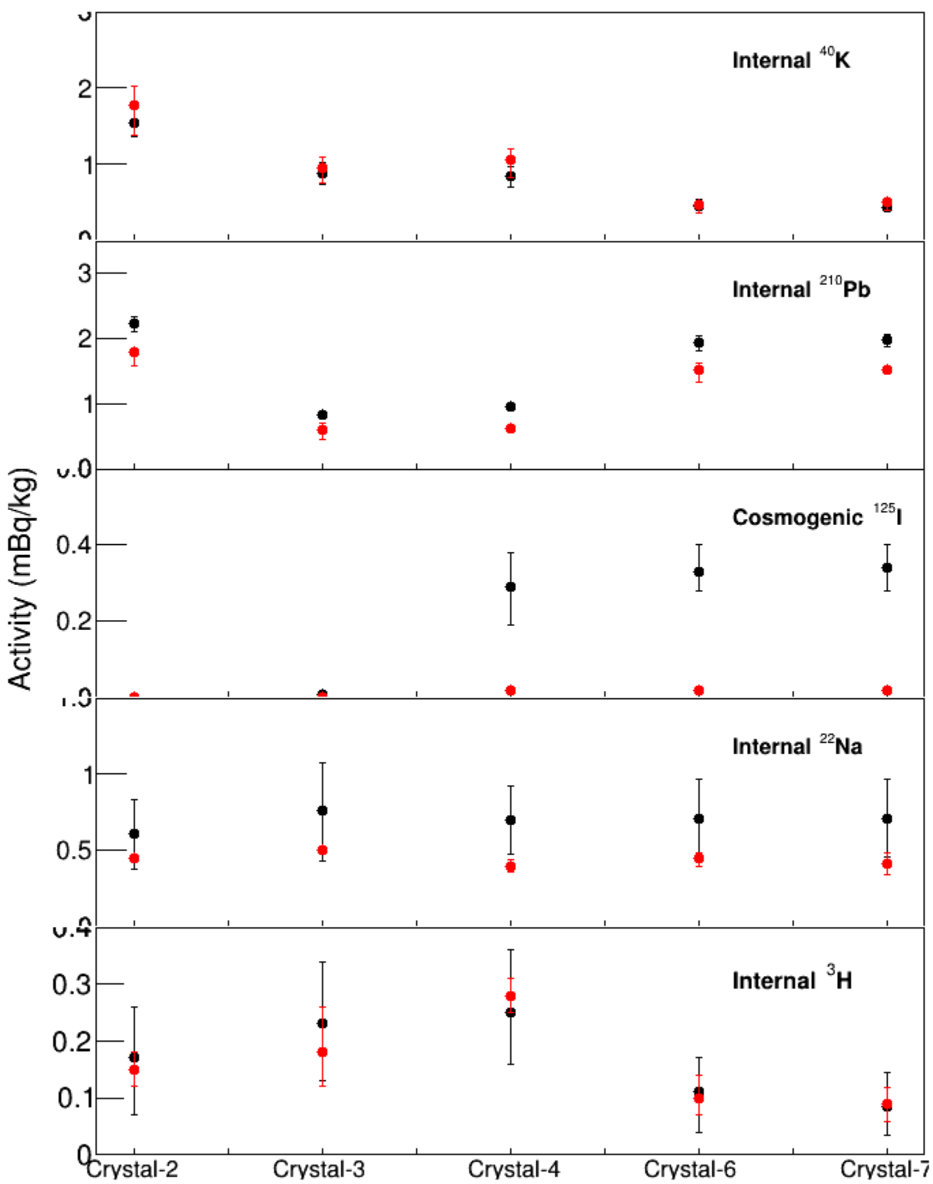

Figure 4.28 Comparison for the fitted activities between set1 (black) and set2 (red).

4.3.4 Dominant components in signal region

The signal region for COSINE experiment is below 6 keV. This is the reason why single hit spectrum is fitted above 6 keV. The obtained best fit MC hypothesis is extrapolated up to 1 keV which is shown in figure 4.29. There is a good agreement between data and MC so that we can control background very well for any rare event physics search. The dominant background in our ROI are; internal (^{210}Pb, ^{40}K), cosmogenic (^{3}H, ^{113}Sn, ^{109}Cd), surface (^{210}Pb from Teflon reflector, crystal surface). The COSINE-100 crystals were grown in collaboration with Alpha spectra company, Colorado USA so that it suffers from cosmogenic activation due to higher altitude. The ^{210}Pb background is due to the ^{222}Rn exposure either during the crystal grown or machining period. The ^{40}K is basically due to purity of the powder. The background contribution in our ROI for each crystals are summarized into the table 4.5.

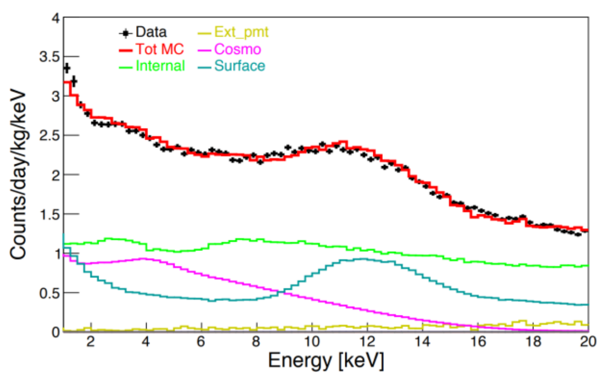

Figure 4.29 Data MC comparison after extrapolating the best fit hypothesis to the signal (1 to 6 keV) region for C6.

Table 4.5: Background estimated to the signal region [1-6 keV]

Background	Crystal-2	Crystal-3	Crystal-4	Crystal-6	Crystal-7
Internal					
^{40}K	0.22±0.004	0.10±0.003	0.12±0.003	0.05±0.007	0.06±0.005
^{210}Pb	1.28±0.04	0.43±0.02	0.47±0.02	1.08±0.03	1.04±0.03
Other ($\times10^{-4}$)	196±18	200 ± 14	75 ± 11	134±16	100±6
Cosmogenic					
^{3}H	1.21 ±0.04	2.57 ±0.05	2.35 ±0.04	1.02 ±0.02	0.88±0.02
^{109}Cd	-	0.06±0.01	0.13±0.01	0.01±0.01	0.008±0.01
Other	-	0.02±0.003	0.06±0.004	0.04±0.003	0.03±0.001
Surface					
^{210}Pb	0.35±0.04	0.32 ±0.05	0.26±0.01	0.56±0.03	0.82±0.04
External	0.06±0.01	0.04±0.01	0.03±0.01	0.04±0.01	0.04±0.01
Total simulation	3.12±0.07	3.61±0.08	3.43±0.06	2.82±0.06	2.89±0.06
Data	3.11±0.03	3.53±0.07	3.34±0.05	2.80±0.05	2.84±0.05

Chapter 5

WIMP searches with 1keV analysis threshold

Lowering the experimental analysis threshold is a key factor to improve the experiment's sensitivity in order to search the WIMP induced low energy nuclear recoil rate. Signal to background ratio is boosted with lower threshold, assuming a constant background, that scale down the dependence of the WIMP signal on astrophysical uncertainties. As a result, lowering threshold is more effective to improve the sensitivity at lower WIMP mass. This section describes about the spin-independent WIMP interpretation of the DAMA signal above the COSINE-100's background model with 1 keV energy threshold and 97.7 kg. Year exposure.

5.1 Systematics study

The parameters like selection efficiency, resolution measured from the background data and the modeled background method have its own uncertainties which can affect the shape of the background and signal hypothesis. The detail study of the identified systematics is quantified in the following studies.

5.1.1 Signal selection efficiency systematics

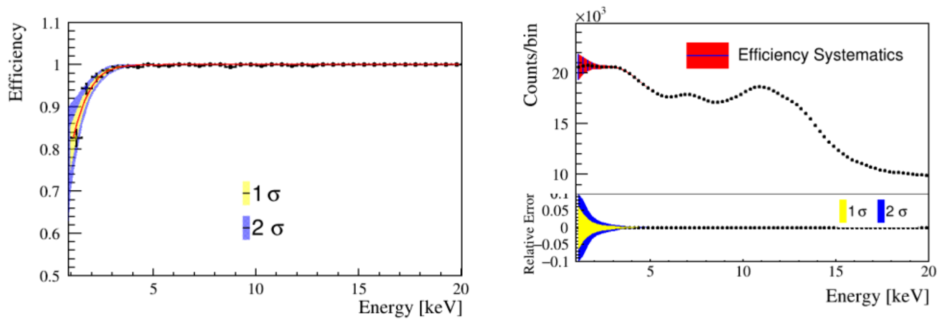

Figure 5.1 The event selection efficiency systematic for Crystal 6 a) displayed with 1(2)σ uncertainty band b) systematic size compared with low energy single hit spectrum (black).

The ^{60}Co calibration run is used to select the scintillating event with an uncertainty followed by the binomial statistics. The efforts are made to model the efficiency in this study as shown in the figure 5.1. First order error function as shown in equation 5.1 is used to model the efficiency. The uncertainties for the parameters are estimated by using the covariance matrix between the parameters assuming the correlation between them. Figure 5.1 (a) shows that the efficiency is well modelled with the error function within the systematics of $\pm$ 1 σ. Figure 5.1 (b) display the measured background (black) with the $\pm$ 1 σ systematic size (green) that corresponds to the event selection efficiency for C6 at low energy. It is found that signal selection efficiency is the most dominant systematics (5 to 6 % at 1 keV) in our ROI. The efficiency selection is crosschecked with independent samples as discussed into section 4.2 and found consistent within statistical fluctuation.

5.1.2 Measured resolution systematics

The energy resolution is parameterized as given by equation 3.1 and figure 5.2 (a) shows the energy dependence resolution (red) for low energy anode data with it's one sigma uncertainty band. The energy resolution is used to smear the simulated events. The $\pm$ 1 σ resolution is applied independently to the MC events and studied the effects of resolution variation in background modeling. Figure 5.2 (b) display the measured background (black) with the ± 1 σ systematic size (green) that corresponds to the energy resolution for C6 at low energy. It is found that resolution systematics is one of the important systematics near to the threshold region because of the ^{22}Na component.

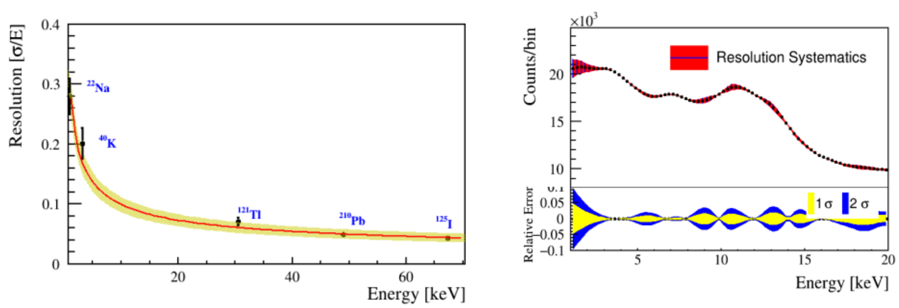

Figure 5.2 The measured energy resolution systematic for Crystal 6 a) displayed with 1σ uncertainty band b) systematic size compared with low energy single hit spectrum (black).

5.1.3 ^{210}Pb surface profiling systematics

The background understanding from ^{210}Pb surface is optimized with its depth profile as discussed into the section 4.3.1 and figure 5.3 (a) shows the surface ^{210}Pb depth profile (red) for low energy anode data with its $\pm$ 1 σ (magenta and blue) line. The surface ^{210}Pb is one of the dominant components in ROI, so $\pm$ 1 σ systematics is applied to the slope parameter to get the re-weighted ^{210}Pb surface energy spectrum from MC. This variation of the slope parameter in background modeling is considered as ^{210}Pb surface profiling systematics. Figure 5.3 (b) display the measured background (black) with the $\pm$ 1 σ systematic size (green) that corresponds to the ^{210}Pb surface profile for C6 at low energy. This systematic size is the crystal dependence as expected due to different level of the ^{210}Pb surface component for each crystal. It is found that this systematics is the one important systematics (1 to 3 % at 1 keV) in our ROI.

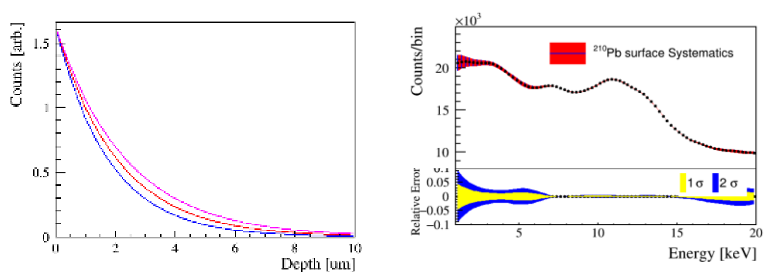

Figure 5.3 The measured surface profile systematic for Crystal 6 a) displayed with 1σ uncertainty band b) systematic size compared with the low energy single hit spectrum (black).

5.1.4 Energy scale non-linearity systematics

The energy scale non-linearity behavior from the NaI(Tl) is addressed in some level as discussed into the section 4.1.1. But the data points to calibrate the COSINE crystals are limited and that causes the different non-linear distribution than the reference measurement (measured for Compton electros) [89] as shown in figure 4.1 and 4.2. The model calibration function for COSINE detector (red) as shown in figure 5.4 (a) that follows ±1σ variation is chosen such that a nuisance parameter can change the relative light yield but cannot modify it beyond the limits set by known peaks in each low-energy single-hit spectrum.

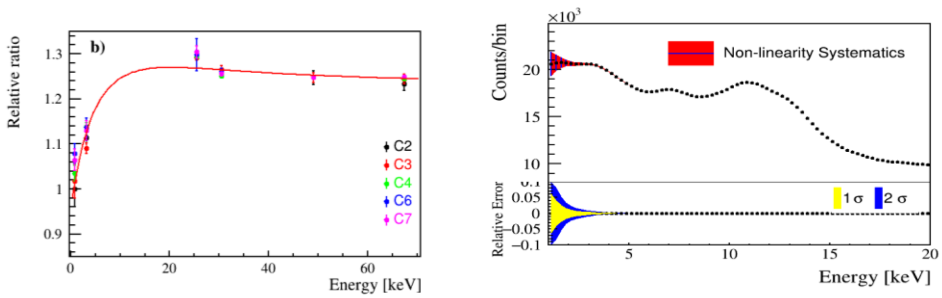

Figure 5.4 The measured energy scale non-linearity systematic a) Non-linear calibration for COSINE Crystals b) systematic size compared with the low energy single hit spectrum (black) for Crystal 6.

5.1.5 PMT's position and background measurement systematics

The background from PMTs are simulated and constrained in background modeling based on the measurements using HPGe detector. It is found that the spectral shape is different between PMT window and barrel part. Such spectral changes in MC due to different vertex position in background modeling is used as a PMT's position systematics as shown in figure 5.5 (a). The simulation isn't well reproduced in some region like multiple anode (above 50 to 70 keV) and single hit dynode above 2.7 MeV in few crystals. The PMT background is dominant in both regions. It is found that the spectral shape from the PMT are location dependent and it is hard to measure the PMT background from several location like its base, barrel, circuitry or windows and so on. Such mismodeling is covered by possible variation in PMT background measurement as shown in figure 5.5 (b). It is found that PMT background variation affect less than 0.5 % for single hit low energy region in background modeling. This variation is used as a PMT's background measurement systematics and it shows good coverage for PMT background dominated channels like high energy spectrum and low energy multiple spectrum as shown in 5.5 (b)

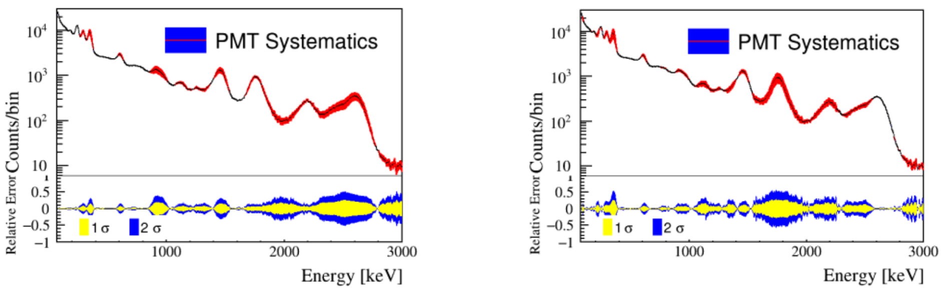

Figure 5.5 The systematic size from PMTs compared with high energy single hit spectrum (black) for Crystal 6 a) corresponds to the PMT location b) correspond to the measured background from PMT.

5.1.6 Total systematics

The six possible systematics as discussed above were estimated and its quadrature is used as a total systematics. Figure 5.6 display the measured background spectrum (black) compared with the modelled background with ±1 (±2) σ systematic size with green (yellow) color for background model. The dominant systematics in ROI is the efficiency, resolution and surface profiling and other three sideband channels (low energy multiple, high energy single and multiple) are the PMT location and its measurements. In general, an improved background modeling based on Geant4 based simulation reproduces the background data for all four channels and gives a better understanding of the detector's background within its systematics. The best fit models are extrapolated to the signal region of 1 to 6 keV. This background understanding constrains the WIMP search analysis.

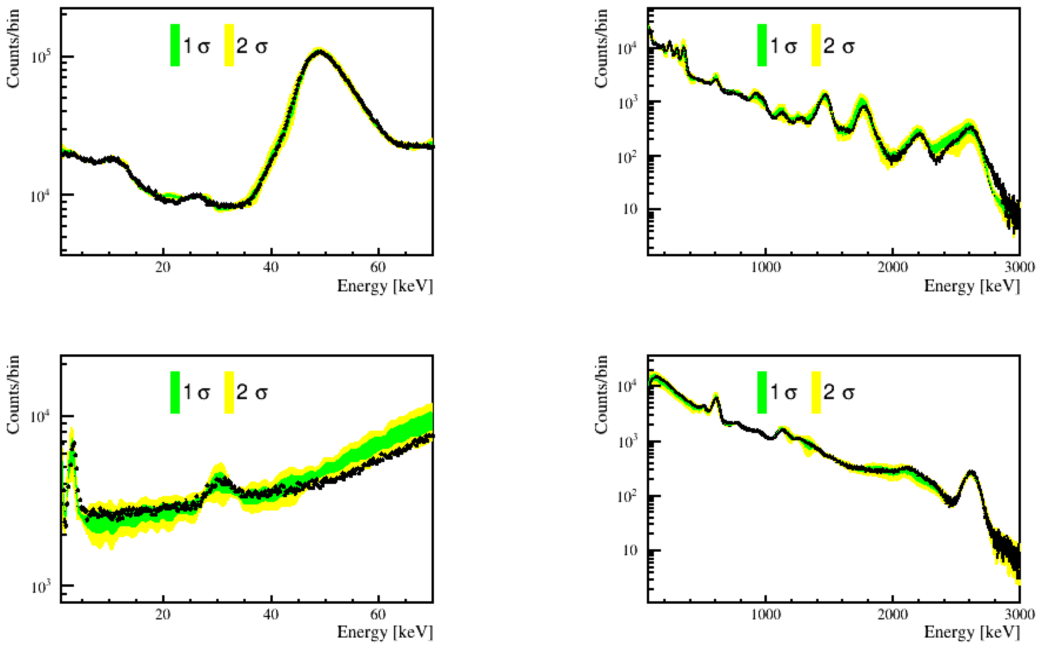

Figure 5.6 The comparison between measured data (black with an error of the 68 % CL) and background modeling with ±1σ (±2σ) green (yellow) band for Crystal 6 a) low energy [single hit] b) high energy [single hit] c) low energy [multiple hit] d) high energy [multiple hit].

5.2 WIMP signal extraction

A likelihood fit based on the Bayesian approach is performed to extract the WIMP signal with known background components as discussed in section 4.3 and expected WIMP hypothesis based on standard halo model. The details of WIMP extraction analysis will be discussed into the following sub-section.

5.2.1 Pseudo data generation

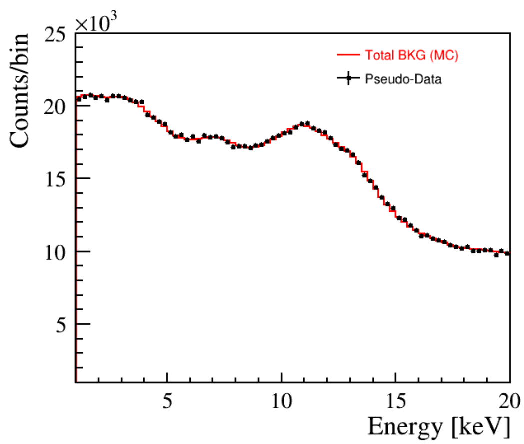

Figure 5.7 The pseudo-data (black) generated from the COSINE background model (red) for Crystal 6.

The WIMP search data is blinded to test the tools used for this analysis. So, 1000 pseudo-data are generated from the background modeled total MC to test the fitter. The example of the one pseudo data is as shown in figure 5.7. A toy Monte Carlo based on the background model is used to generate the pseudo data. Each bin of the single hit background modelled spectrum from 1 to 20 keV with 0.25 keV binsize is randomized (Poisson) to account the fluctuation. This pseudo experiment set is used to set the expected 90% C.L with different WIMP mass in order to avoid the biasing for WIMP search.

5.2.2 Computing the expected WIMP signal

The expected recoil spectrum is computed based on the framework purposed by Lewin and Smith [93]. The differential nuclear recoil rate per unit target mass for elastic scattering between WIMPs of mass m_χ and target nuclei of mass M is;

$$\frac{dR}{dE_{nr}} = \frac{2\rho_\chi}{m_\chi}\int d^3\vartheta \cdot \vartheta \cdot f(v,t)\frac{d\sigma}{dq^2}(q^2,\vartheta), \qquad (5.1)$$

where ρ_χ is the local mass density of WIMPs, f (v, t) is the time-dependent WIMP velocity distribution, and $d\sigma/dq^2$ (q^2, v) is the differential cross section depending on the velocity with the momentum exchange $q^2 = 2ME_{nr}$.

A Maxwellian distribution as shown in equation 5.2 as described by Lewis and Smith is assumed to get the WIMP velocity distribution,

$$f(v,t) = \frac{1}{N_{esc}} e^{-(v-v_E)^2 / 2\sigma_\vartheta^2} \qquad (5.2)$$

where N_{esc} is a normalization constant, v_E is the Earth velocity relative to the WIMP dark matter and σ_v is the velocity dispersion. The standard halo parameterization is used with local dark matter density ρ_χ = 0.3 GeV/cm 3 , v_E = 232 km/s, $\sqrt{}$ 2σv = 220 km/s and galactic escape velocity v_{esc} = 544 km/s.

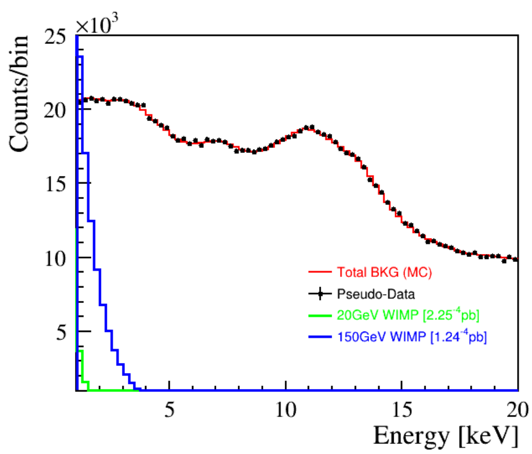

Figure 5.8 Expected WIMP signal display together with pseudo-data (black) generated from COSINE background model (red). WIMP signal green (blue) corresponds to 20 (150) GeV/c^2 from DAMA Na(I) contour.

The quenching factor and a nuclear form factors are used to model the nuclear response in differential cross section as described in ref [94], [95]. The estimated resolution discussed at the section 3.1.3 are considered, to obtain the differential nuclear recoil rate. The 21 different WIMP mass varying from 4 GeV/c^2 to 10,000 Gev/c^2 are simulated for this study. It is found that DAMA Na-contour and I-contour cross section corresponds to 18.6 GeV/c^2 and 159 GeV/c^2 respectively with COSINE measured quenching factor assuming the canonical spin-independent model. The 20 GeV/c^2 and 150 GeV/c^2 WIMP signal compared with the pseudo-data as discussed into the section 5.2.1 as shown in figure 5.8. It shows that there should be large excess of the events over background model if WIMP signal will be existing in COSINE data.

5.2.3 Bayesian approach to fit the signal

A fitter based on Bayesian approach is developed to extract the WIMP signal strength. Markov Chain Monte Carlo (MCMC) that follow the Metropolis-Hastings algorithm [96], [97] is used for multi-dimensional integrals of marginalization of posterior probability. The posterior probability density function (PDF) in terms of WIMP nucleon cross section is obtained via marginalization of the likelihood function including the prior,

$$P(\sigma|M) = N\pi(\sigma) \int L(M|q)\pi(q)dq \qquad (5.3)$$

where P(σ|M) is the posterior PDF, L(M|q) is the likelihood function, π(q) and π(σ) are priors, and N is a normalization factor, σ is the cross section (signal strength), M is the measurement and q denotes the parameters associated with systematic uncertainties.

5.2.4 WIMP signal extraction

Bayesian based binned, maximum likelihood fitting tool is used to fit the WIMP search data over known background, different WIMP mass hypothesis and systematics. Mean values and 68% uncertainties of the best fit parameters of the background components are propagated to this fitter as a starting position and a constraint, respectively. The constraints are applied as a 1 σ Gaussian priors for those background models. Similarly, systematic parameters that change the shape of the background distributions are added as nuisance parameters. In any stage, the event selections have not been modified.

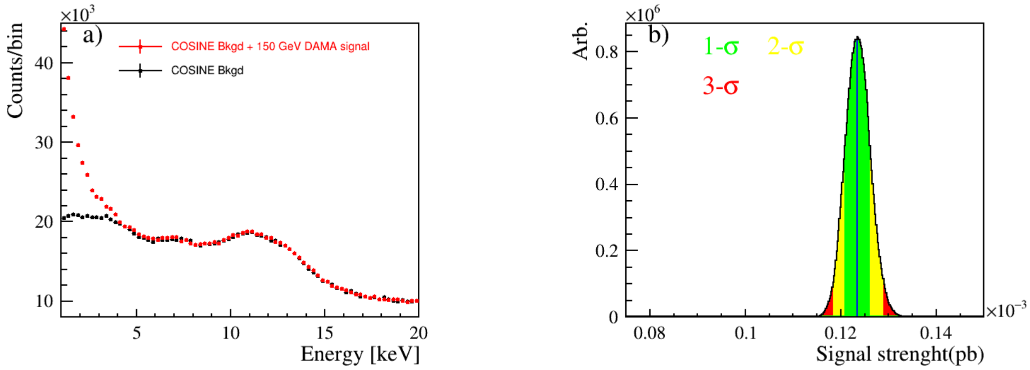

Figure 5.9 Analysis verification method to avoid any possible biasness on the WIMP search result a) one set of pseudo experiment generated from total MC (red) and total MC plus 150 GeV/c^2 mass (blue) WIMP signal b) the signal strength 1 σ(green), 2 σ(yellow), 3 σ(red) extracted after performing the likelihood fit.

The fitting machinery is validated by injecting/extracting the known signal strength. 1000 sets of pseudo-data together with 150 Gev/c^2 WIMP signal that corresponds to the DAMA Iodine contour assuming the canonical spin independent interaction are generated. The 150 GeV/c^2 WIMP mass that have an equivalent cross-section of 1.24×10^{-4} pb as ref [95]. Then log-likelihood fit is performed with this pseudo data to extract the WIMP signal strength. Figure 5.9 shows the fitted signal with COSINE background model after injecting 1.24×10^{-4} pb WIMP signal which returns $(1.239 \pm 0.026) \times 10^{-4}$ pb signal with 48 sigma significance. This verification avoids the possibilities of any biasness that is coming from the analysis technique.

The data is blinded for this analysis and expected sensitivity at 90 % confidence level is projected from 1000 pseudo-data set with expected backgrounds hypothesis without any dark matter induced signal. The WIMP mass from 4 GeV/c^2 to 10,000 GeV/c^2, 21 in total are simulated as discussed into the section 5.2.2. The median of the expected signal strength at 90 % confidence level upper limit on the WIMP-nucleon spin-independent cross-section assuming the background only hypothesis (red dotted line), are compared with WIMP-induced DAMA/LIBRA allowed region (solid contour) and COSINE-100 set1 result (black solid line) are shown in figure 5.10. The sensitivity is expected to be improved by one order of magnitude than set1 result. The lowered 1 keV analysis threshold is very helpful to improve the sensitivity of the experiment specially for low mass WIMP search.

The data unblinding is under the reviewing process while preparing this thesis. Since, the data is well reproduced from the known background as discussed into section 4.3 so data fit would be expected to favor the null hypothesis.

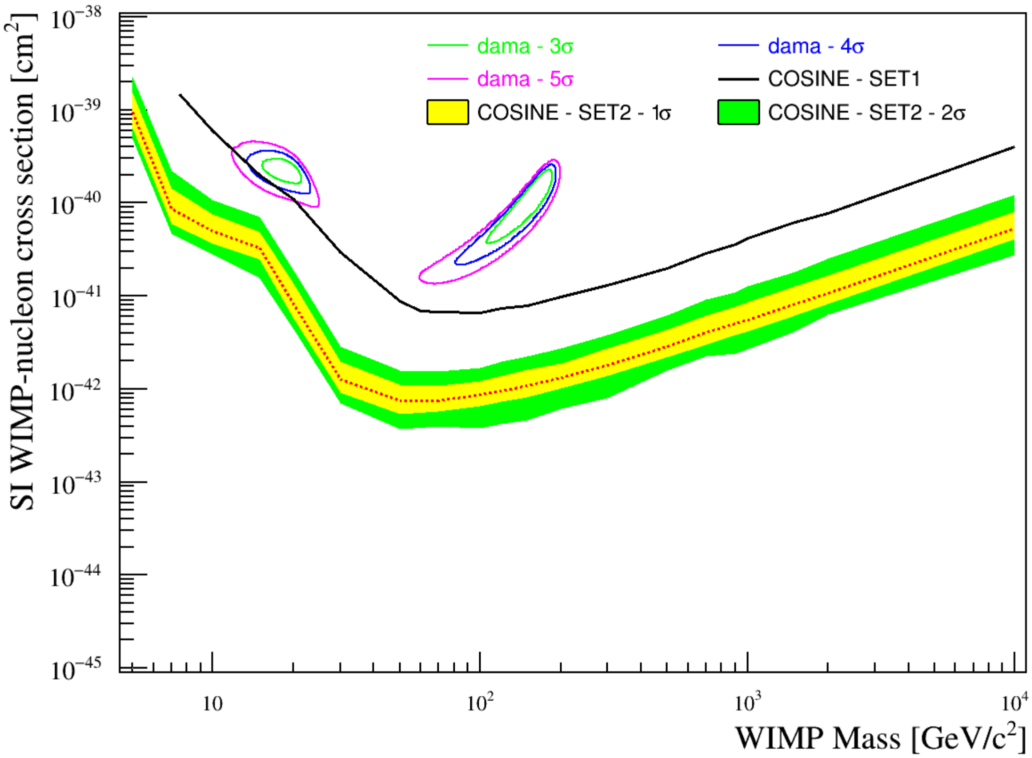

Figure 5.10 The expected sensitivity assuming background only hypothesis using set2 data with 1 keV energy threshold. The sensitivity is improved by order of magnitude while comparing between the 2 keV and 1 keV analysis threshold

Chapter 6

Conclusion

COSINE-100 has been successfully running from September 2016 and accumulating around 3 years of the dark matter search data. During this period it has demonstrated the very stable run with more than 94% of live time and proved the feasibility of running low background NaI(Tl) experiment with remotely operating facility in stable environmental condition.

Three data sets are used for physics analysis. The set1 data having 59.54 days is used to understand the detector response, its background understanding and WIMP search analysis. A spin-independent WIMP search analysis with 2 keV analysis threshold have been performed to confirm the DAMA-LIBRA result using first 59.5 days of data. There is no room for the WIMP signals that could be attributed to WIMP interactions after the data fit, so a 90% CL limit from the data was set. COSINE-100 excludes DAMA/LIBRA phase 1's interpretation with the spin-independent WIMP interaction with standard halo model in NaI(Tl) crystal. For a complete test of DAMA, the model independent annual modulation search is required.

The set2 data which is 1.7 years, is used for first annual modulation analysis. The modulation amplitude is scanned with a fixed phase based on the standard halo model of 152.5 days and the DAMA modulation amplitude-phase of 145 days independently using the chi-square minimization fits. Eventually, the amplitude is scan after floating the phase. The best fit for the 2–6 keV range has a modulation amplitude of 0.0092±0.0067 counts/keV/kg/day with a phase of 127.2±45.9 days. Log-Likelihood parameter estimation of the annual modulation with amplitude and phase as free parameters shows that the current data from COSINE-100 is consistent with both the DAMA/LIBRA annual modulation result and the null hypothesis at the 68.3 %.

The 2 keV analysis threshold result for annual modulation analysis is statistically limited. As like other several experiments, we need to improve the sensitivity with large exposure and lower threshold. COSINE-100 made a noble effort to lower down the analysis threshold from 2 keV to 1 keV as discussed in this analysis. The background understanding is improved for set2 data with 1 keV threshold that gives better constrain for physics searchs. The WIMP search sensitivity is found to be improved by order of the magnitude with 1 keV threshold. The method developed to achieve 1 keV threshold potentially lead to go below 1 keV with more efforts.

The COSINE-100 collaboration is actively working with several physics channels and preparing for phase2 with low background detector. In this way, COSINE family is very close to resolve the anomaly in the field of the dark matter search.

References

[1] J. Beringer *et al.*, “Review of particle physics,” *Phys. Rev. D - Part. Fields, Gravit. Cosmol.*, vol. 86, no. 1, 2012.

[2] V. M. Slipher, “The radial velocity of the Andromeda Nebula,” *Lowell Obs. Bull.*, vol. 2, pp. 56–57, 1913.

[3] G. Lemaître, “Un Univers homogène de masse constante et de rayon croissant rendant compte de la Vitesse radiale des nébuleuses extra-galactiques,” *Ann. la Soc. Scietifique Bruxelles*, vol. 47, pp. 49–57, 1927.

[4] EDWIN HUBBLB, “A RELATION BETWEEN DISTANCE AND RADIAL VELOCITY AMONG EXTRA-GALACTIC NEBULAE,” *Proc. Natl. Acad. Sci.*, vol. 15(3), pp. 168–173, 1929.

[5] P. A. R. Ade *et al.*, “Planck 2013 results. XXII. Constraints on inflation,” *Astron. Astrophys.*, vol. 571, 2014.

[6] P. A. R. Ade *et al.*, “Detection of B -mode polarization at degree angular scales by BICEP2,” *Phys. Rev. Lett.*, vol. 112, no. 24, pp. 1–25, 2014.

[7] G. R. Farrar and M. E. Shaposhnikov, “Baryon Asymmetry Jv,” *Phys. Rev. Lett.*, vol. 70, no. 19, pp. 2833–2836, 1993.

[8] B. S. Ryden, *Introduction to cosmology, Addison-Wesley*. 2003.

[9] A. A. Penzias and R. W. Wilson, “A measurement of excess antenna temperature at 4080 Mc/s,” *Astropart. J.*, vol. 142, p. 419, 1965.

[10] D. J. FIXSEN et al., “THE COSMIC MICROWAVE BACKGROUND SPECTRUM FROM THE FULL COBE1 FIRAS DATA SET,” *Astrophys. J.*, vol. 1, pp. 400–426, 1996.

[11] S. Weinberg, *Cosmology, Oxford University Press, Oxford*. 2008.

[12] D. Perkins, *Particle Astrophysics, Oxford University Press, Oxford*. 2003.

[13] D. Larson *et al.*, “Seven-year wilkinson microwave anisotropy probe (WMAP*) observations: Power spectra and WMAP-derived parameters,” *Astrophys. Journal, Suppl. Ser.*, vol. 192, no. 2, 2011.

[14] “http://lambda.gsfc.nasa.gov/.” .

[15] N. Jarosik *et al.*, “Seven-year wilkinson microwave anisotropy probe (WMAP*) observations: Sky maps, systematic errors, and basic results,” *Astrophys. Journal, Suppl. Ser.*, vol. 192, no. 2, 2011.

[16] G. Borner, *The early universe, Fourth Edition, Spinger Verlag Berlin Heidelberg*. 2003.

[17] K. Z. H. V. Klapdor-Kleingrothaus, *Teilchenastrophysil, B. G. Teubner Stuttgart*. 1997.

[18] G. Bertone, D. Hooper, and J. Silk, “Particle dark matter: Evidence, candidates and constraints,” *Phys. Rep.*, vol. 405, no. 5–6, pp. 279–390, 2005.

[19] K. A. Olive, “TASI Lectures on Dark Matter,” no. January, pp. 1–54, 2003.

[20] K Nakamura et al, “Review of Particle Physics,” *J. Phys. G Nucl. Part. Phys.*, vol. 37, no. 7A, pp. 184–192, 2010.

[21] M. Davis et al, “A survey of galaxy redshifts. III – the density field and the induced gravity field,” *Astropart. J.*, vol. 254, pp. 437–450, 1982.

[22] J. R. Gott *et al.*, “The tenth data release of the Sloan digital sky survey: First spectroscopic data from the SDSS-iii apache point observatory galactic evolution experiment,” *Astrophys. Journal, Suppl. Ser.*, vol. 211, no. 2, pp. 1–16, 2014.

[23] “Th e l a r g e s c a l e s t r u c t u r e o f t h e U n i v e r s e,” *Nature*, vol. 440, pp. 1137–1144, 2006.

[24] R. H. Sanders, “The universal Faber-Jackson relation,” *Mon. Not. R. Astron. Soc.*, vol. 407, no. 2, pp. 1128–1134, 2010.

[25] V. C. Rubin, J. W. Kent Ford, and N. Thonnard, “Rotational properties of 21 Sc galaxies with a large range of luminosities and radii, from NGC 4605 (R=4kpc) to

UGC 2885 (R=122kpc)," *Astropart. J.*, vol. 238, p. 471, 1980.

[26] E. Corbelli and P. Salucci, "The extended rotation curve and the dark matter halo of M33," *Mon. Not. R. Astron. Soc.*, vol. 311, no. 2, pp. 441–447, 2000.

[27] D. Clowe *et al.*, "A Direct Empirical Proof of the Existence of Dark Matter," *Astrophys. J.*, vol. 648, no. 2, pp. L109–L113, 2006.

[28] M. Bradač *et al.*, "Revealing the Properties of Dark Matter in the Merging Cluster MACS J0025.4−1222," *Astrophys. J.*, vol. 687, no. 2, pp. 959–967, 2008.

[29] S. W. Allen, R. W. Schmidt, and A. C. Fabian, "Cosmological constraints from the X-ray gas mass fraction in relaxed lensing clusters observed with Chandra," *Mon. Not. R. Astron. Soc.*, vol. 334, no. 2, pp. L11–L15, 2002.

[30] S. D. M. White, J. F. Navarro, A. E. Evrard, and C. S. Frenk, "The baryon content of galaxy clusters: A challenge to cosmological orthodoxy," *Nature*, vol. 366, no. 6454, pp. 429–433, 1993.

[31] "http://chandra.harvard.edu/photo/2006/1e0657/image." .

[32] Orest Chwolson, "Uber eine mogliche Form fiktiver Doppelsterne," *Astro. Nachrichten*, vol. 221, p. 506, 1924.

[33] Albert Einstein, "Lens-Like Action of a Star by the Deviation of Light in the Gravitational Field Albert," *J. Chem. Inf. Model.*, vol. 84, p. 381.

[34] D. Walsh, R. F. Carswell, and R. J. Weymann, “0957+561 A, B: Twin quasistellar objects or gravitational lens?,” *Nature*, vol. 279, no. 5712, pp. 381–384, 1979.

[35] C. Alcock *et al.*, “THE MACHO PROJECT: MICROLENSING RESULTS FROM 5.7 YEARS OF LARGE MAGELLANIC CLOUD OBSERVATIONS,” *Astrophys. J.*, vol. 542, pp. 281–307, 2000.

[36] P. Tisserand *et al.*, “Limits on the Macho content of the Galactic Halo from the EROS-2 survey of the magellanic clouds,” *Astron. Astrophys.*, vol. 469, no. 2, pp. 387–404, 2007.

[37] T. American and A. Society, “ANALYSIS OF A HUBBLE SPACE TELESCOPE SEARCH FOR RED DWARFS: LIMITS ON BARYONIC MATTER IN THE GALACTIC HALO,” *Astrophys. J.*, vol. 456, pp. 49–54, 1996.

[38] “http://hubblesite.org/newscenter/archieve/releases/1995/14/ Image.” .

[39] M. Persic and P. Salucci, “The baryon content of the universe,” *Mon. Not. R. Astr. Soc.*, vol. 258, p. 14P, 1992.

[40] et al I. Abt, “GERDA: The Germanium detector array for the search of neutrinoless double beta decays of 76Ge at LNGS,” *Propos. to LNGS P38/04*, 2004.

[41] J. A. et Al, “KATRIN design report 2004,” 2004.

[42] S. P. Martin, “A Supersymmetry Primer,” pp. 1–153, 2010.

[43] F. D. Steffen, “Dark-matter candidates : AAxions, neutralinos, gravitinos, and axinos,” *Eur. Phys. J. C*, vol. 59, no. 2, pp. 557–588, 2009.

[44] L. Bergstrom and A. Goobar*, Cosmology and particle astrophysics, Springer Praxis Books / Astronomy and Planetary Sciences, Praxis Publ*. 2006.

[45] G. G. Raffelt, *Astrophysical Axion Bounds*, vol. 741. 2008.

[46] K. Freese, M. Lisanti, and C. Savage, “Colloquium: Annual modulation of dark matter,” *Rev. Mod. Phys.*, vol. 85, no. 4, pp. 1561–1581, 2013.

[47] L. Baudis, “Direct Detection of Cold Dark Matter,” 2007.

[48] R. Agnese *et al.*, “Silicon detector dark matter results from the final exposure of CDMS II,” *Phys. Rev. Lett.*, vol. 111, no. 25, pp. 1–6, 2013.

[49] N. Weiner, “Inelastic dark matter,” *Phys. Rev. D - Part. Fields, Gravit. Cosmol.*, vol. 64, no. 4, p. 11, 2001.

[50] R. Bernabei et al., “Dark matter search,” *Riv. N. Cim. 26,* vol. 26, no. 1, pp. 1–73, 2003.

[51] R. B. et Al., “FIRST MODEL INDEPENDENT RESULTS FROM DAMA/LIBRA-PHASE2 The,” *NUCL. PHYS. AT. ENERGY*, vol. 19, pp. 307–

325, 2018.

[52] J. Amaré *et al.*, “First Results on Dark Matter Annual Modulation from the ANAIS-112 Experiment,” *Phys. Rev. Lett.*, vol. 123, no. 3, pp. 1–6, 2019.

[53] E. Barbosa De Souza *et al.*, “First search for a dark matter annual modulation signal with NaI(Tl) in the Southern Hemisphere by DM-Ice17,” *Phys. Rev. D*, vol. 95, no. 3, pp. 1–6, 2017.

[54] K. Fushimi *et al.*, “KamLAND-PICO PROJECT TO SEARCH FOR COSMIC DARK MATTER,” pp. 333–335, 2014.

[55] P. Montini, “Dark matter search with the SABRE experiment,” pp. 5–8, 2018.

[56] K. W. Kim *et al.*, “Tests on NaI(Tl) crystals for WIMP search at the Yangyang Underground Laboratory,” *Astropart. Phys.*, vol. 62, pp. 249–257, 2015.

[57] G. Adhikari *et al.*, “Initial performance of the COSINE-100 experiment,” *Eur. Phys. J. C*, vol. 78, no. 2, 2018.

[58] H. et al. Prihtiadi, “Muon detector for the COSINE-100 experiment,” *JINST*, vol. 13, p. T02, 2018.

[59] G. Adhikari *et al.*, “Search for a Dark Matter-Induced Annual Modulation Signal in NaI(Tl) with the COSINE-100 Experiment,” *Phys. Rev. Lett.*, vol. 123, no. 3, p. 31302, 2019.

[60] G. Adhikari *et al.*, “An experiment to search for dark-matter interactions using sodium iodide detectors,” *Nature*, vol. 564, no. 7734, pp. 83–86, 2018.

[61] J. Billard, E. Figueroa-Feliciano, and L. Strigari, “Implication of neutrino backgrounds on the reach of next generation dark matter direct detection experiments,” *Phys. Rev. D*, vol. 89, no. 2, pp. 1–15, 2014.

[62] R. Bernabei *et al.*, “First results from DAMA/LIBRA and the combined results with DAMA/NaI,” *Eur. Phys. J. C*, vol. 56, no. 3, pp. 333–355, 2008.

[63] R. Bernabei *et al.*, “New results from DAMA / LIBRA,” pp. 39–49, 2010.

[64] R. Bernabei *et al.*, “Performances of the new high quantum efficiency PMTs in DAMA/LIBRA,” *J. Instrum.*, vol. 7, no. 3, 2012.

[65] E. Aprile *et al.*, “Dark matter results from 225 live days of XENON100 data,” *Phys. Rev. Lett.*, vol. 109, no. 18, pp. 1–6, 2012.

[66] D. S. Akerib *et al.*, “First results from the LUX dark matter experiment at the sanford underground research facility,” *Phys. Rev. Lett.*, vol. 112, no. 9, pp. 1–7, 2014.

[67] R. Agnese *et al.*, “Search for low-mass weakly interacting massive particles using voltage-assisted calorimetric ionization detection in the SuperCDMS experiment,” *Phys. Rev. Lett.*, vol. 112, no. 4, pp. 1–6, 2014.

[68] J. Amaré *et al.*, "Preliminary results of ANAIS-25," *Nucl. Instruments Methods Phys. Res. Sect. A Accel. Spectrometers, Detect. Assoc. Equip.*, vol. 742, pp. 187–190, 2014.

[69] J. Amaré *et al.*, "Cosmogenic production of tritium in dark matter detectors," *Astropart. Phys.*, vol. 97, pp. 96–105, 2018.

[70] J. Cherwinka *et al.*, "First data from DM-Ice17," *Phys. Rev. D - Part. Fields, Gravit. Cosmol.*, vol. 90, no. 9, pp. 1–13, 2014.

[71] P. Adhikari *et al.*, "Understanding internal backgrounds in NaI(Tl) crystals toward a 200 kg array for the KIMS-NaI experiment," *Eur. Phys. J. C*, vol. 76, no. 4, 2016.

[72] H. S. Lee, "Dark matter search with CsI (Tl) crystal," 2007.

[73] J. S. Park *et al.*, "Performance of a prototype active veto system using liquid scintillator for a dark matter search experiment," *Nucl. Instruments Methods Phys. Res. Sect. A Accel. Spectrometers, Detect. Assoc. Equip.*, vol. 851, no. September 2016, pp. 103–107, 2017.

[74] G. Adhikari *et al.*, "Study of fast neutron detector for COSINE-100 experiment," *J. Instrum.*, vol. 13, no. 6, 2018.

[75] R. Bernabei *et al.*, "Final model independent result of DAMA/LIBRA-phase1,"

Eur. Phys. J. C, vol. 73, no. 12, pp. 1–11, 2013.

[76] G. Adhikari *et al.*, “The COSINE-100 data acquisition system,” *J. Instrum.*, vol. 13, no. 9, 2018.

[77] K. Blum, “DAMA vs. the annually modulated muon background,” *Arxiv Prepr. arXiv1110.0857*, p. 12, 2011.

[78] S. H. Song, K. K. Joo, S. H. So, and I. S. Yeo, “Feasibility study of a gadolinium-loaded DIN-based liquid scintillator,” *J. Korean Phys. Soc.*, vol. 63, no. 6, pp. 970–974, 2013.

[79] Y. Ding, Z. Zhang, J. Liu, Z. Wang, P. Zhou, and Y. Zhao, “A new gadolinium-loaded liquid scintillator for reactor neutrino detection,” *Nucl. Instruments Methods Phys. Res. Sect. A Accel. Spectrometers, Detect. Assoc. Equip.*, vol. 584, no. 1, pp. 238–243, 2008.

[80] P. Lombardi, G. Ranucci, F. Ortica, and A. Romani, “Decay time and pulse shape discrimination of liquid scintillators based on novel solvents,” *Nucl. Instruments Methods Phys. Res. Sect. A Accel. Spectrometers, Detect. Assoc. Equip.*, vol. 701, pp. 133–144, 2013.

[81] T. Y. Kim *et al.*, “Study of the internal background of CsI(Tℓ) crystal detectors for dark matter search,” *Nucl. Instruments Methods Phys. Res. Sect. A Accel.*

Spectrometers, Detect. Assoc. Equip., vol. 500, no. 1–3, pp. 337–344, 2003.

[82] S. E. Quirk, "Purification of Liquid Scintillator and Monte Carlo Simulations of Relevant Internal Backgrounds in SNO +," *A thesis Submitt. to Dep. Physics, Eng. Phys. Astrronomy, Queen's Univ. Kingston, Ontario, Canada*, no. January, 2008.

[83] "https://github.com/influxdata/ 1252 influxdb." .

[84] "http://grafana.org." .

[85] J. H. Friedman, "Greedy function approximation: A gradient boosting machine," *Ann. Stat.*, vol. 29, no. 5, pp. 1189–1232, 2001.

[86] P. Adhikari *et al.*, "Background model for the NaI(Tl) crystals in COSINE-100," *Eur. Phys. J. C*, vol. 78, no. 6, 2018.

[87] E. Barbosa de Souza *et al.*, "Study of cosmogenic radionuclides in the COSINE-100 NaI(Tl) detectors," *Astropart. Phys.*, vol. 115, p. 102390, 2020.

[88] G. J. Feldman, "Unified approach to the classical statistical analysis of small signals," *Phys. Rev. D - Part. Fields, Gravit. Cosmol.*, vol. 57, no. 7, pp. 3873–3889, 1998.

[89] L. Swiderski *et al.*, "Response of doped alkali iodides measured with gamma-ray absorption and Compton electrons," *Nucl. Instruments Methods Phys. Res. Sect. A Accel. Spectrometers, Detect. Assoc. Equip.*, vol. 705, pp. 42–46, 2013.

[90] H. W. Joo *et al.*, “Quenching factor measurement for NaI(Tl) scintillation crystal,” *Astropart. Phys.*, vol. 108, pp. 50–56, 2019.

[91] J. Allison *et al.*, “Recent developments in GEANT4,” *Nucl. Instruments Methods Phys. Res. Sect. A Accel. Spectrometers, Detect. Assoc. Equip.*, vol. 835, pp. 186–225, 2016.

[92] G. Adhikari *et al.*, “Understanding NaI(Tl) crystal background for dark matter searches,” *Eur. Phys. J. C*, vol. 77, no. 7, 2017.

[93] J. D. Lewin and R. F. Smith, “Review of mathematics, numerical factors, and corrections for dark matter experiments based on elastic nuclear recoil,” *Astropart. Phys.*, vol. 6, no. 96, pp. 87–112, 1996.

[94] V. Gluscevic, M. I. Gresham, S. D. McDermott, A. H. G. Peter, and K. M. Zurek, “Identifying the theory of dark matter with direct detection,” *J. Cosmol. Astropart. Phys.*, vol. 2015, no. 12, 2015.

[95] Y. Ko *et al.*, “Comparison between DAMA/LIBRA and COSINE-100 in the light of quenching factors,” *arXiv*, 2019.

[96] L. Tierney, “Markov Chains for Exploring Posterior Distributions,” *Ann. Stat.*, vol. 22, no. 4, pp. 1701–1762, 1994.

[97] C. Siddhartha and E. Greenberg, “Understanding the Metropolis-Hastings

Algorithm," *Am. Stat.*, vol. 49, p. 327, 1995.